

AIR FORCE  
TECHNICAL DATA CENTER

TECHNICAL LIBRARY

Document No. 61-84-698

Copy No. 13

AD 605978

UNIVERSITY OF MINNESOTA  
INSTITUTE OF TECHNOLOGY

DEPARTMENT OF AERONAUTICAL ENGINEERING

Progress Report No 16 ✓

THEORETICAL PARACHUTE INVESTIGATIONS *Bee*

Wright Air Development Center Contract No AF 33(616)-6372 ✓

Department of Aeronautical Engineering No 9093

1 December 1960 to 28 February 1961



MINNEAPOLIS 14, MINNESOTA

Progress Report No 16 ✓

THEORETICAL PARACHUTE INVESTIGATIONS

Wright Air Development Center Contract No AF 33(616)-6372 ✓

Department of Aeronautical Engineering No 9093

1 December 1960 to 28 February 1961

COPY	1	OF	1	mgr
HARD COPY	\$ .400			
MICROFICHE	\$ .100			

DDC  
RECEIVED  
SEP 26 1964  
DDC-IRA E

Dr. h. G. Heinrich, Professor, Department of Aeronautical Engineering  
 Dr. T. Riabokin, Research Associate, Department of Aeronautical Engineering  
 Prof. S. K. Ibrahim, Research Fellow, Department of Aeronautical Engineering  
 Mr. E. L. Haak, Engineer, Department of Aeronautical Engineering  
 Mr. R. J. Niccum, Engineer, Department of Aeronautical Engineering  
 Mr. G. Stumbris, Assistant Scientist, Rosemount Aeronautical Laboratories  
 and graduate and undergraduate students (part time workers) of the  
 Department of Aeronautical Engineering, University of Minnesota  
 (See Appendix)

## TABLE OF CONTENTS

<u>Project No</u>		<u>Page</u>
1	Investigations of Wake Effects on the Behavior of Parachutes and Other Retardation Devices Behind Large Bodies at Subsonic and Supersonic Speeds; . . . . .	4
	Subsonic and Supersonic Wind Tunnel Studies Theoretical Wake Studies with Experimental Verification	
4	Investigation of Basic Stability Parameters of Conventional Parachutes; . . . . .	20
	Wind Tunnel Investigation of Aerodynamic Coefficients Theoretical Investigation of Dynamic Stability Effective Porosity Studies	
6	Determination of the Minimum Sized Parachute for Stabilization of Aerial Delivery Cargo; . . . . .	38
7	Theoretical Study of Supersonic Parachute Phenomena; . . . .	39
	Pressure Distribution on Conventional Canopy in Supersonic Wind Tunnel Water Analogy Studies Stability and Drag Tests of Spiked Parachute	
8	Theoretical Analysis of the Dynamics of the Opening Parachute; . . . . .	67
	Analytical Method for Parachute Opening Time Analytical Method for Parachute Opening Force Size-Force History of Inflating Parachute Pressure Distribution on Canopy of Inflating Parachute	
9	Statistical Analysis of Extraction Time, Deployment Time, Opening Time, and Drag Coefficient for Aerial Delivery Parachutes and Systems . . . . .	98
10	Study of Basic Principles of New Parachutes and Retardation Devices . . . . .	99

# THEORETICAL PARACHUTE INVESTIGATIONS

## Progress Report No 16

### INTRODUCTION

1.0 This is the sixteenth quarterly report covering the time from 1 December 1960 to 28 February 1961 on the study program on basic information of aerodynamic Retardation, which was initiated on 15 February 1957.

1.1 The objectives in the first year of this program were specified in Wright Air Development Contract No AF 33(616)-3955 as follows:

Project No 1, "Investigation of wake effects on the behavior of parachutes and other retardation devices behind large bodies at subsonic and supersonic speeds."

Project No 2, "Reduction of test results from drop and wind tunnel tests with extended skirt parachutes of various sizes, and establishment of design data for this type of parachute to obtain the best performance characteristics."

Project No 3, "Establishment of reliable test methods for measuring the pressure distribution on the inner and outer surface of porous textile parachute canopies."

Project No 4, "Investigation of basic stability parameters of conventional parachutes."

Project No 5, "Study of possible methods to decrease the opening time of parachutes without increase of opening shock."

1.2 Work on the five specific objectives listed above continued through the second year of the program under an extension of the contract named above. In addition, two new objectives were introduced as follows:

Project No 6, "Determination of the minimum sized parachute for stabilization of general aerial delivery cargo."

Project No 7, "Theoretical study of supersonic parachute phenomena."

The approach to the solutions of the various problems concerning these seven objectives was outlined in the Proposed Technical Program submitted on 26 November 1957.

1.3 Work on four of the above seven objectives (Projects No 2, No 3, No 5, and No 6) has been completed, and final technical reports either have been or are being prepared. Work on the remaining three objectives (Projects No 1, No 4, and No 7) is continuing under Wright Air Development Center Contract No AF 33(616)-6372. In addition, this contract presents three new objectives as follows:

Project No 8, "Theoretical analysis of the dynamics of the opening parachute."

Project No 9, "Statistical analysis of extraction time, deployment time, opening time, and drag

coefficient for aerial delivery parachutes and systems."

Project No 10, "Study of basic principles of new parachutes and retardation devices."

The approach to the solutions of the various problems concerned with these three new objectives and that to the solutions of new problems concerned with the three old objectives which are being continued (Projects No 1, No 4, and No 7) are outlined in the Proposed Technical Program submitted on 16 February 1959. Additional proposals, which further outline the course of investigation, were submitted on 22 April 1959, 21 May 1959, 26 February 1960, and 22 April 1960.

1.4 As in preceding reporting periods, work during this reporting period has been pursued in accordance with the technical program and is described in the following sections of this report. The continuation of efforts on each project during the next reporting period is outlined within the report for that specific project.

## Project No 1

### 2.0      Investigations of Wake Effects on the Behavior of Parachutes and Other Retardation Devices Behind Large Bodies at Subsonic and Supersonic Speeds

#### 2.1      Subsonic Wind Tunnel Studies

2.1.1      The velocity and pressure distribution in the wake behind a body of revolution has been reported in Ref 1, in which an experimental parameter  $\lambda$  was introduced. This parameter  $\lambda$  was extracted from wind tunnel measurements of the pressure distribution in the wake of an ogive cylinder at distances downstream of  $X/D$  ranging from 2 to 12. This body had a drag coefficient,  $C_D = 0.35$ . These experiments indicated a strong dependence of  $\lambda$  upon the location measured from the rear end of the wake producing body. It was assumed at that time that  $\lambda$  will also vary with the drag coefficient of the primary body. Satisfactory agreement between theoretical prediction and experimental results for this body was obtained for  $X/D \geq 6$  by using an average value of  $\lambda$ .

2.1.2      Reference 2 presented values for  $\lambda$  which were extracted from similar measurements in the wake of a flat disk with  $C_D = 1.11$  at distances downstream from  $X/D = 2$  to  $X/D = 20$ . It was found that  $\lambda$  for this body differed considerably from the one described in Ref 1, which confirmed the above assumption.

2.1.3      In order to determine a relationship between  $\lambda$  and  $C_D$ , a new series of wind tunnel experiments was made using several bodies of revolution with

a wide range of drag coefficients, from  $C_D = 0.194$  to  $C_D = 1.405$ . Figure 1-1 presents these models, and gives their respective drag coefficients. During this reporting period, the data from these wind tunnel tests was reduced to graphical form.

## 2.1.4 Results

2.1.4.1 Figures 1-2 through 1-11 present the pressure distributions in the wakes behind the above described bodies of revolution. This pressure distribution is presented as a pressure coefficient,  $C_p$ , defined as:

$$C_p = \frac{P_o - P}{q}, \quad (1.1)$$

where  $P_o$  = wake total pressure  
 $P$  = wake static pressure  
 $q$  = free stream dynamic pressure.

The dimensionless parameter,  $2r/D$ , is the distance normal to the body centerline divided by the body radius.

2.1.4.2 Certain qualitative conclusions about the behavior of wakes behind bodies of revolution can readily be drawn from observation of Figs 1-2 through 1-11. At any given control section downstream from the rear of the bodies, the dimensionless width of the wake of bodies of low  $C_D$  is much less than the corresponding width for bodies of high  $C_D$ . It is also observed that at a given control section located some distance downstream, the pressure coefficient,  $C_p$ , on the centerline is noticeably reduced for the bodies of low  $C_D$  over the corresponding  $C_p$  for bodies of high  $C_D$ . These two wake effects apparently are the result of the much greater turbulent mixing behind bodies of high  $C_D$ .



than behind bodies of low  $C_D$ , which causes greater spreading of the wake and a much faster approach to free stream dynamic pressure on the centerline behind the bodies of high  $C_D$ .

#### 2.1.5 Proposed Work

Work during the next reporting period will be devoted to completion of predicting the dependence of  $X$  (Ref 1) on distance downstream from a body and on the drag coefficient. An attempt will then be made to determine generalized relationships for velocity and pressure distribution in the turbulent wake in subsonic flow, with the drag coefficient and the shape of the primary body as parameters. This will include correlating the experimental wakes presented in this report with the theoretical wakes predicted in Ref 1, and drawing conclusions as to the validity of the theory and its limits of application.

#### 2.2 Transonic and Supersonic Wind Tunnel Studies

2.2.1 As stated in Progress Report No 15, all testing concerning the transonic and supersonic phases of this project has been completed and present efforts are being devoted toward the completion of final technical reports. The completed studies have been divided under four headings, as follows:

- 1) Pressure and velocity distribution in the wake
- 2) Single body drag
- 3) Drag of secondary body in wake of primary body
- 4) System drag of combination of secondary and primary bodies.

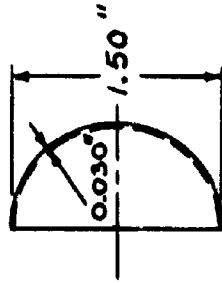
A technical report is being written under each of these headings.

2.2.2 During this reporting period, a draft of the report for the first objective, pressure and velocity distribution in the wake, was completed. The final draft of this report will be submitted to the Procuring Agency shortly. Also, initial drafts of the reports for the second and third objectives, single body drag, and drag of second body in wake of primary body, have been nearly completed and final drafts of these two reports will probably be ready for submittal during the following reporting periods.

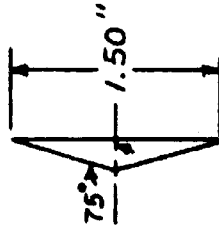
2.2.3 Work during the next reporting period will be devoted toward the completion of the drafts of these reports and the preparation of a draft of the report under the fourth objective, system drag of combination of secondary and primary bodies.

#### REFERENCES

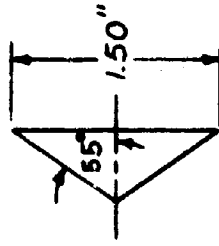
- 1) Heinrich, H. G., and Riabokin, T.: Analytical and Experimental Considerations of the Velocity Distributions in the Wake of a Body of Revolution, WADC Technical Report, Contract No AF 33(616)-6372, December, 1959.
- 2) Rubbert, P.E.: Investigation of the Velocity Distribution in the Wake of an Axially Symmetric Body, Master's Thesis submitted to the Graduate School of the University of Minnesota, July, 1960.



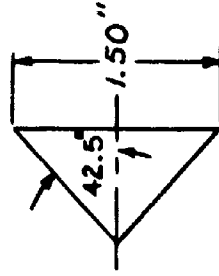
MODEL A  
HOLLOW HEMISPHERE  
(OPEN TO FLOW)  
 $C_D = 1.40$



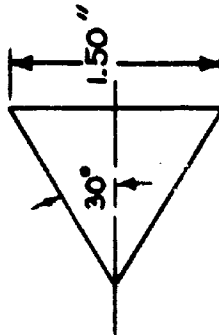
MODEL B  
CONE  
 $C_D = 1.03$



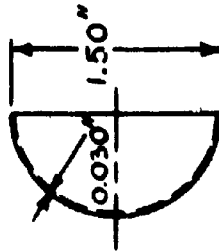
MODEL C  
CONE  
 $C_D = 0.836$



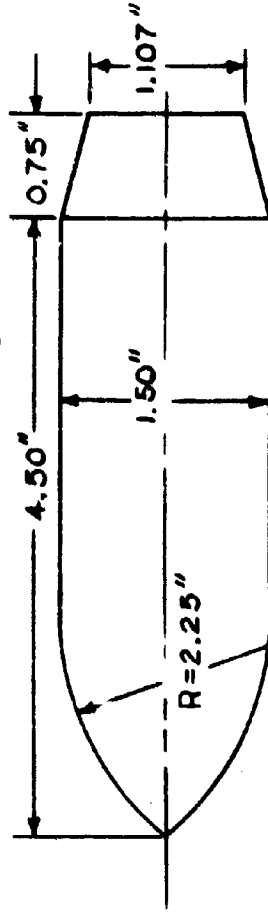
MODEL D  
CONE  
 $C_D = 0.743$



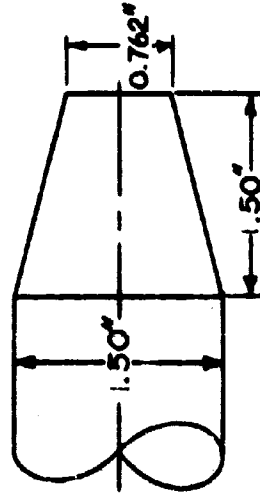
MODEL E  
CONE  
 $C_D = 0.577$



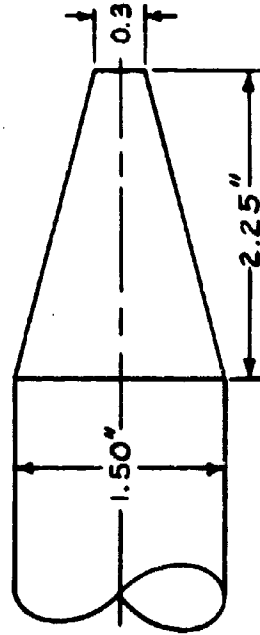
MODEL F  
HOLLOW HEMISPHERE  
(CLOSED TO FLOW)  
 $C_D = 0.425$



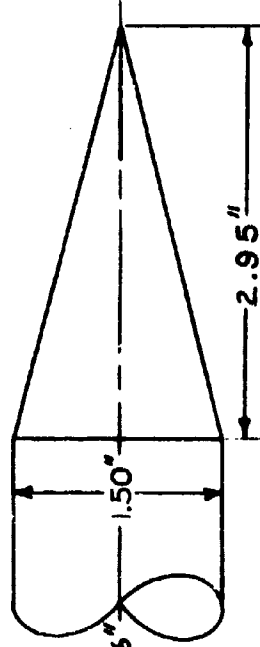
MODEL G  
OGIVE CYLINDER WITH  
AFTERBODY NO. 1.  
 $C_D = 0.230$



MODEL H  
OGIVE CYLINDER WITH  
AFTERBODY NO. 2.  
 $C_D = 0.206$



MODEL I  
OGIVE CYLINDER WITH  
AFTERBODY NO. 3.  
 $C_D = 0.197$



MODEL J  
OGIVE CYLINDER WITH  
AFTERBODY NO. 4.  
 $C_D = 0.194$

FIG 1-1. BODIES OF REVOLUTION

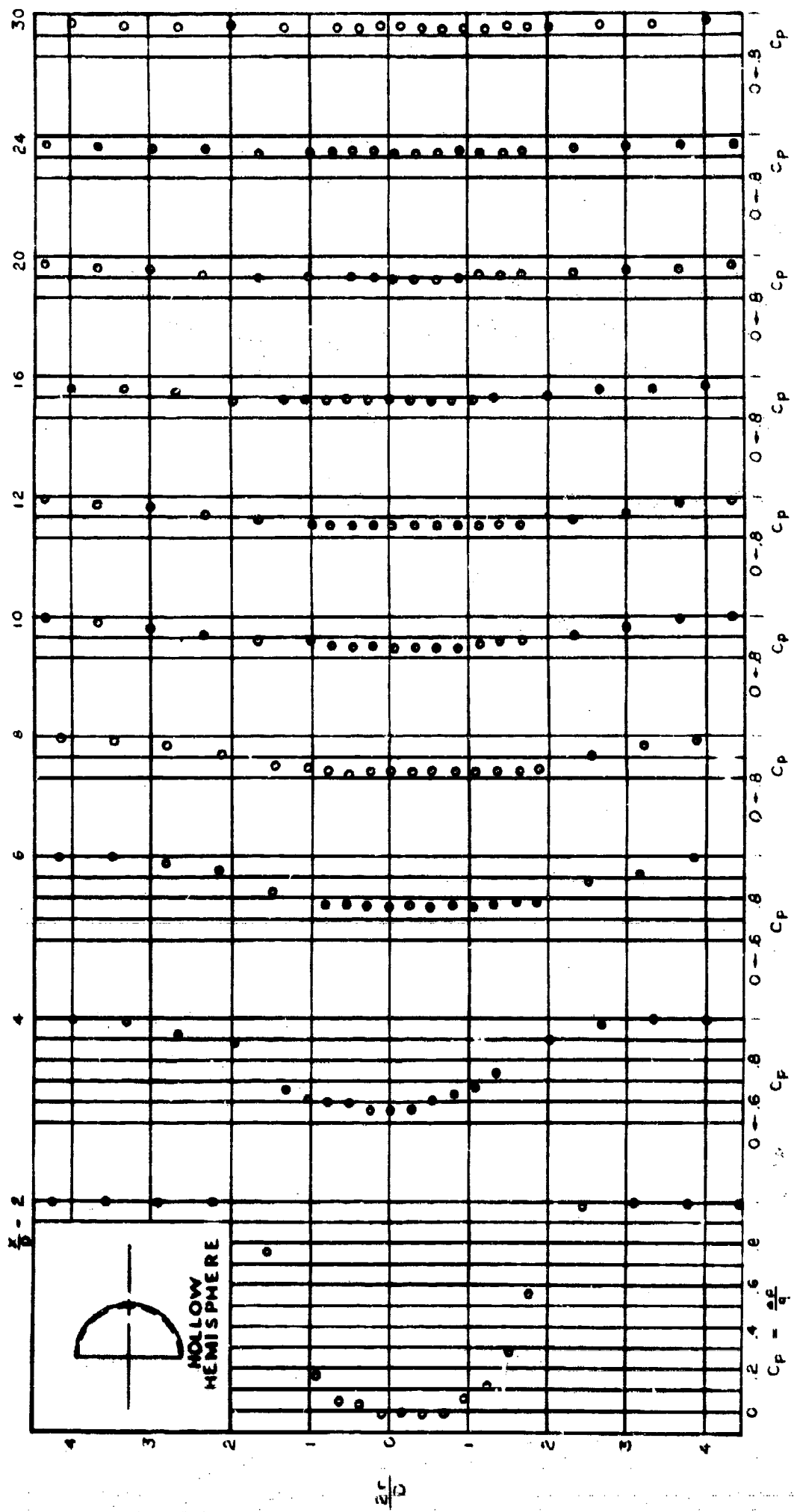


FIG 1-2. EXPERIMENTAL PRESSURE DISTRIBUTION IN THE WAKE OF MODEL A,  $C_D=1.40$

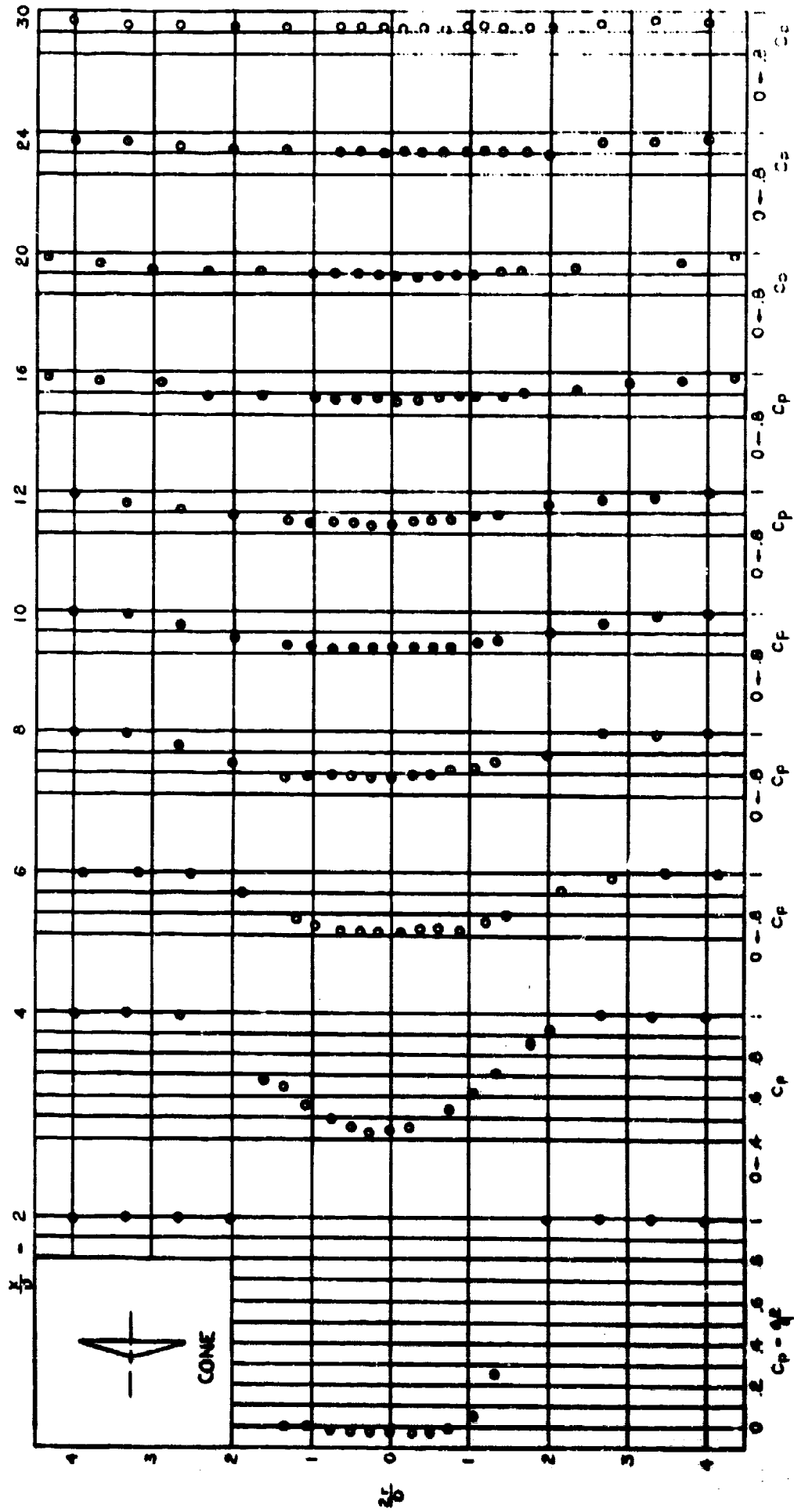


FIG 1-3. EXPERIMENTAL PRESSURE DISTRIBUTION IN THE WAKE OF MODEL B,  $C_D = 0.025$

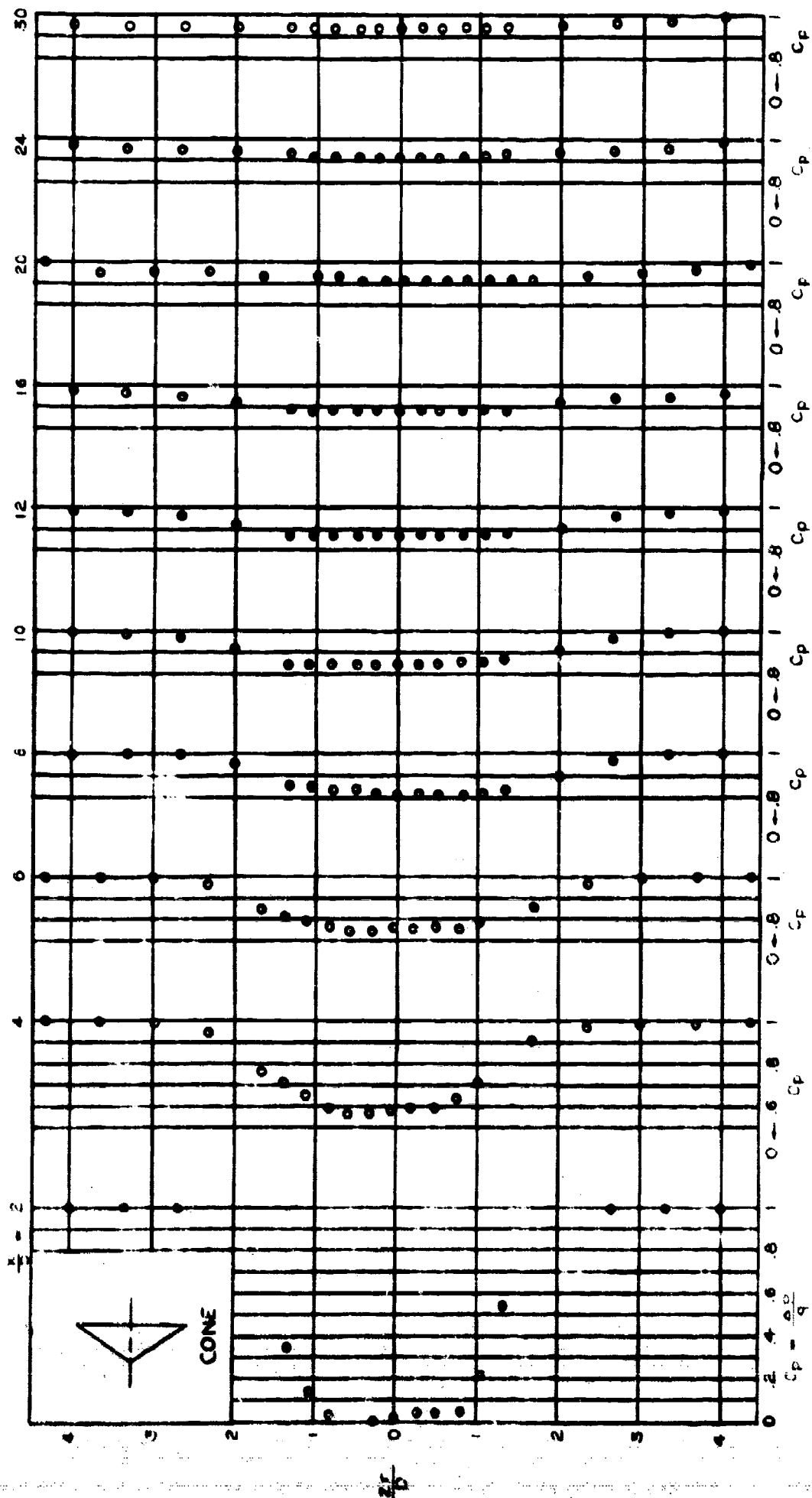


FIG 1-4. EXPERIMENTAL PRESSURE DISTRIBUTION IN THE WAKE OF MODEL C,  $C_D = 0.836$

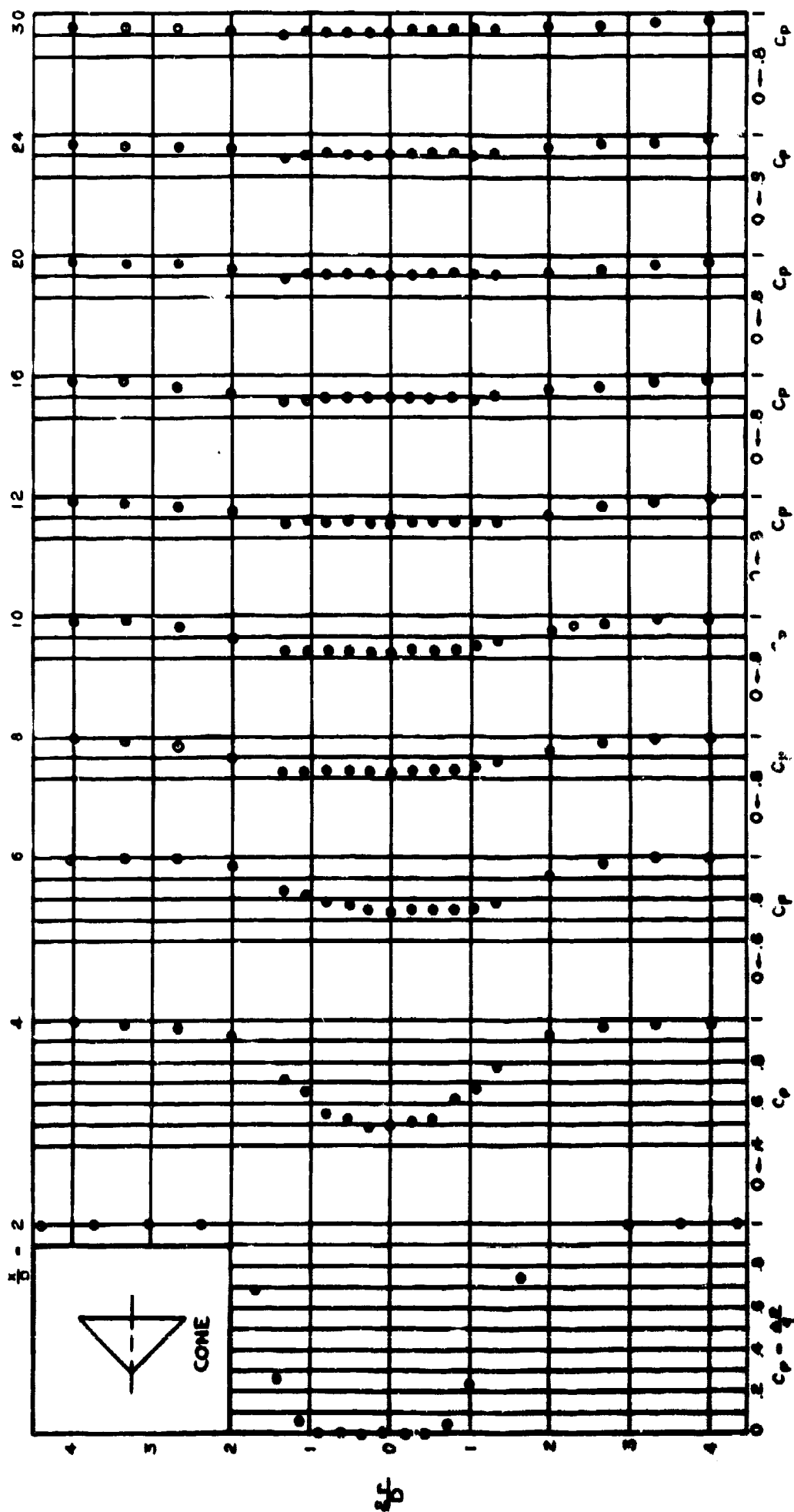


FIG 1-3. EXPERIMENTAL PRESSURE DISTRIBUTION IN THE WAKE OF MODEL D,  $C_D = 0.743$



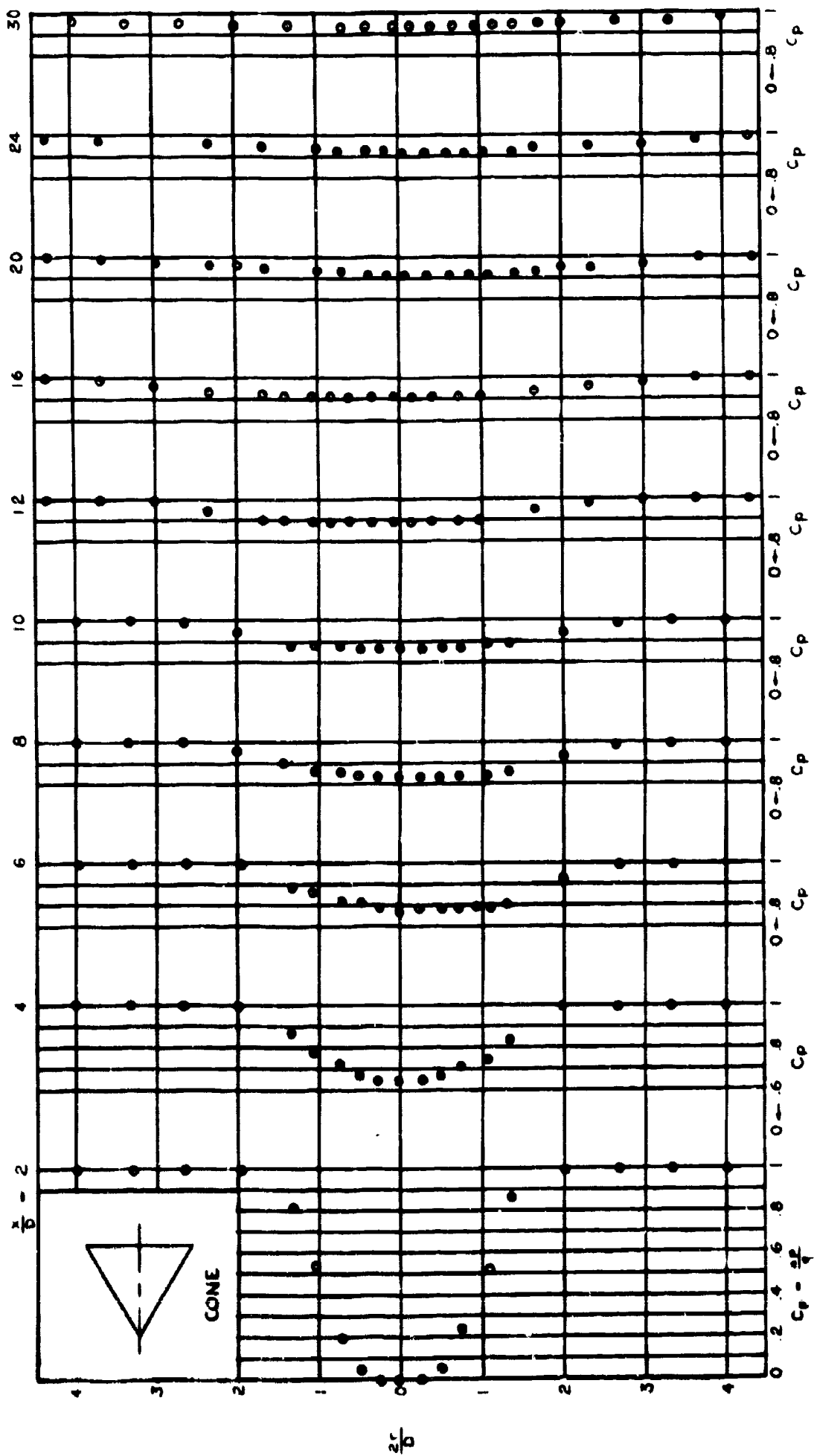


FIG 1-6. EXPERIMENTAL PRESSURE DISTRIBUTION IN THE WAKE OF MODEL E,  $C_D = 0.577$

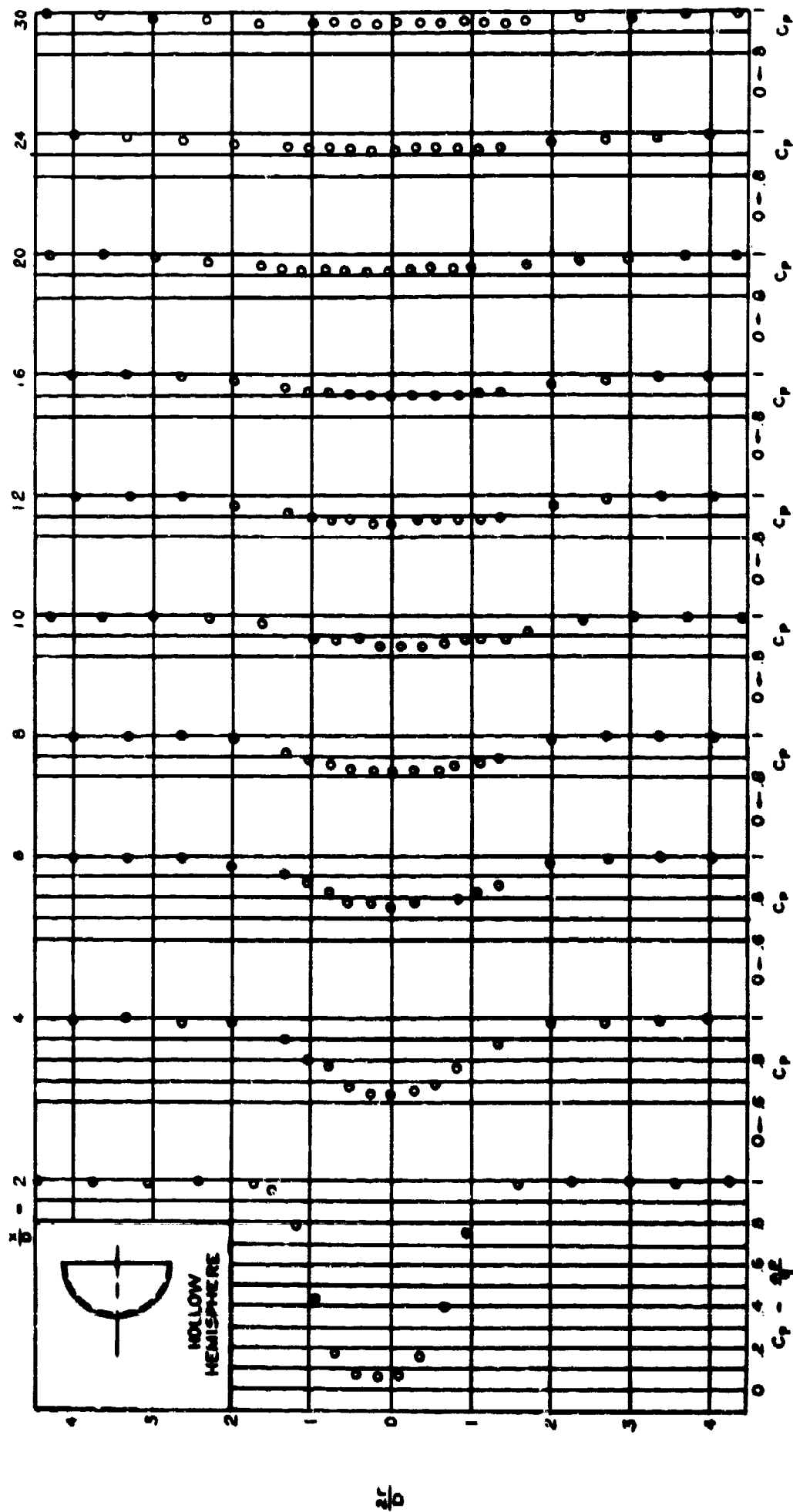


FIG 1-7. EXPERIMENTAL PRESSURE DISTRIBUTION IN THE WAKE OF MODEL F,  $C_D = 0.425$

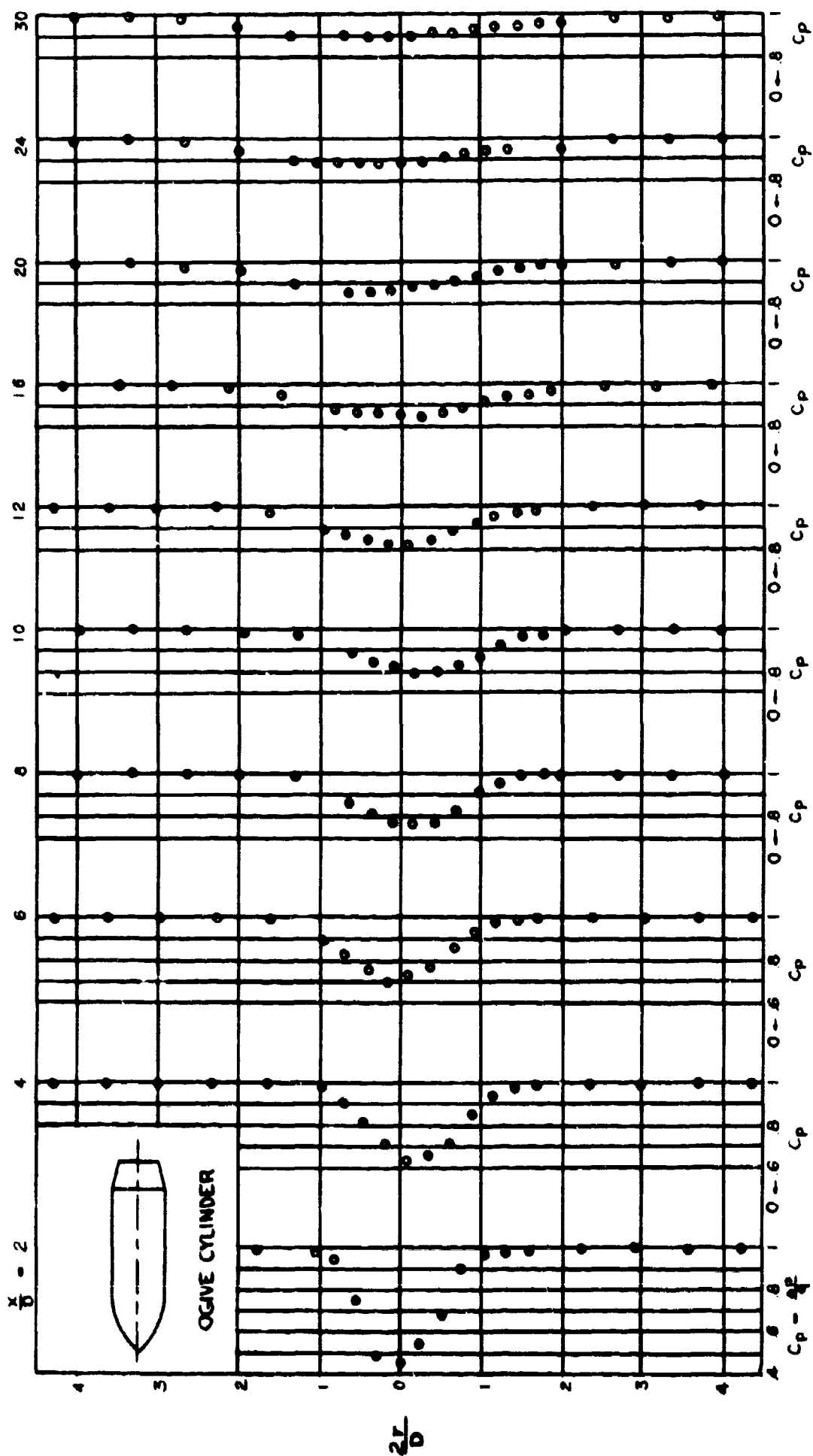


FIG 1-8. EXPERIMENTAL PRESSURE DISTRIBUTION IN THE WAKE OF MODEL G,  $C_D = 0.23$

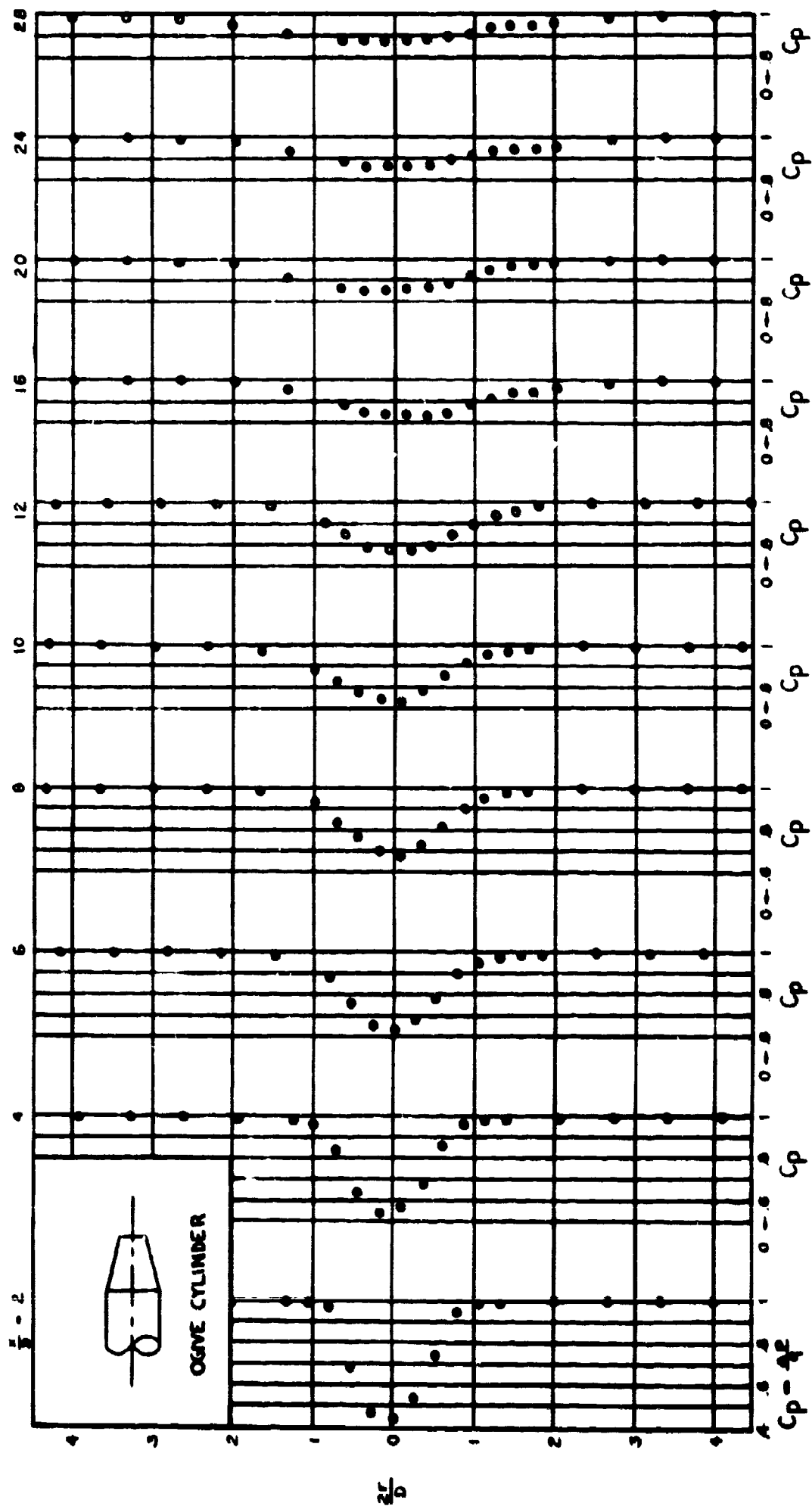


FIG 1-9. EXPERIMENTAL PRESSURE DISTRIBUTION IN THE WAKE OF MODEL H,  $C_D = 0.206$

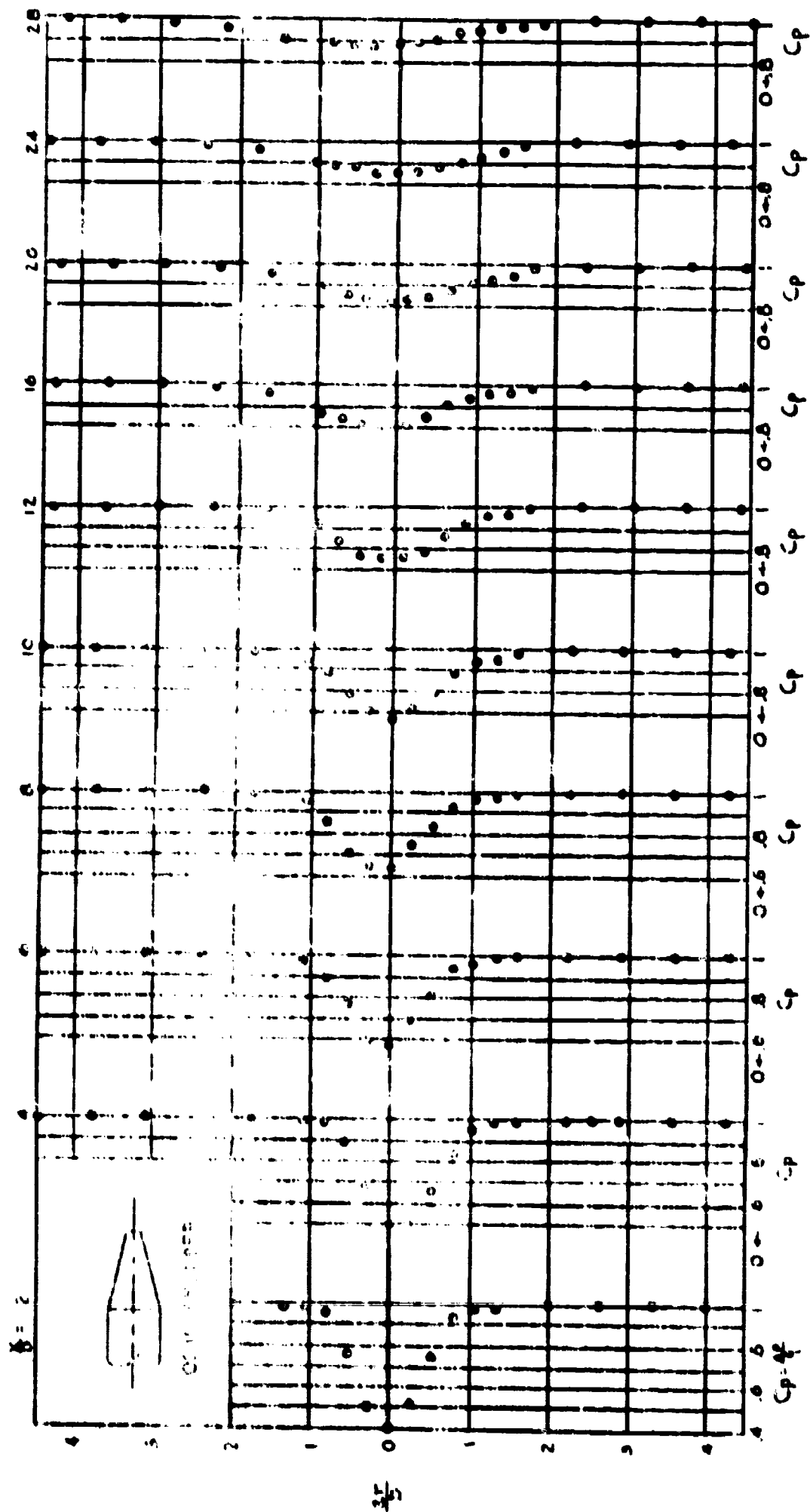


FIG 1-10 EXPERIMENTAL PRESSURE DISTRIBUTION IN THE WAKE OF MODEL 1,  $C_p = 0.197$ .

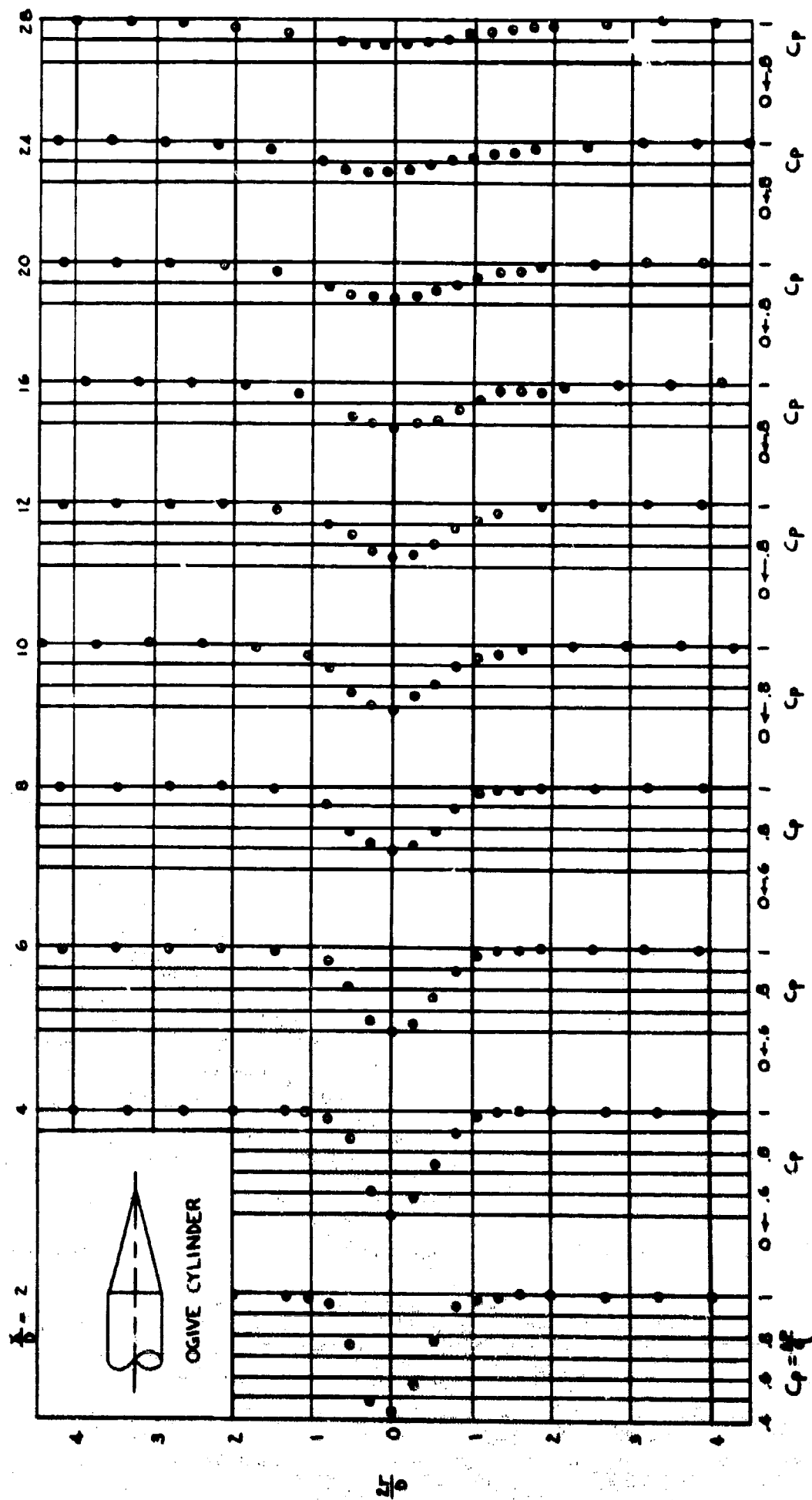


FIG 1-11. EXPERIMENTAL PRESSURE DISTRIBUTION IN THE WAKE OF MODEL J,  $C_D = 0.194$ .

## Project No 4

### 3.0      Investigation of Basic Stability Parameters of Conventional Parachutes

#### 3.1      Introduction

3.1.1      The objective of this study is to determine the characteristic aerodynamic coefficients of fourteen conventional parachute types, using cloth porosity and angle of attack as parameters. The aerodynamic coefficients are 1) tangent or axial force coefficient,  $C_T$ , 2) normal or side force coefficient,  $C_N$ , and 3) pitching moment coefficient,  $C_M$ .

3.1.2      The work performed on this project has been divided into three parts: 1) wind tunnel investigation of parachute models, 2) theoretical stability investigations under dynamic conditions, and 3) effective porosity studies.

#### 3.2      Wind Tunnel Investigation of Parachute Models

The draft of the final technical report entitled "Stability and Drag of Parachutes with Varying Effective Porosity," is currently being revised, and will soon be submitted to the contracting agency for review.

#### 3.3      Theoretical Investigation of the Dynamic Stability of Parachutes

##### 3.3.1      Introduction

3.3.1.1      In Progress Report No 1, Appendix D, the differential equations of the laterally disturbed motion of the parachute under certain simplifying

assumptions were derived in the following form:

$$\begin{aligned}
 (\bar{m}_L + m_{vx})\beta' + (m_{vx} - m_{vy})\alpha' - m_{vy} \frac{s}{r} (\alpha'' + \beta'') = \\
 = \frac{\partial C_L}{\partial \alpha} \alpha + \frac{\partial C_L}{\partial \frac{\omega_s r}{V}} (\alpha' + \beta') - C_D \beta,
 \end{aligned}
 \tag{4.1}$$

$$\begin{aligned}
 \left[ I_{yz} + m_{vy} \left( \frac{s}{r} \right)^2 \right] (\alpha'' + \beta'') - m_{vx} \frac{s}{r} \beta' + (m_{vx} - m_{vy}) \frac{s}{r} \alpha' = \\
 = \frac{\partial C_M}{\partial \alpha} \alpha + \frac{\partial C_M}{\partial \frac{\omega_s r}{V}} (\alpha' + \beta').
 \end{aligned}
 \tag{4.2}$$

The arrangement of the coordinate system, sign convention, and definition of symbols are given in Progress Report No 14, Sec 3.3.1.

3.3.1.2 To solve the system of differential equations (4.1) and (4.2), it was supposed that

$$\alpha = A e^{\lambda \tau} \qquad \beta = B e^{\lambda \tau}, \tag{4.3}$$

where A and B are arbitrary constant,  $\tau = vt/r$ , and  $\lambda$ , which may be real or complex, can be determined from the equation



$$\begin{aligned}
& \left[ I_{vz} (\bar{m}_L + m_{vy}) + \bar{m}_L m_{vy} \left( \frac{s}{r} \right)^2 \right] \lambda^3 + \left\{ \left( \frac{\partial C_L}{\partial \alpha} + C_D \right) \left[ I_{vz} + \bar{m}_L \left( \frac{s}{r} \right)^2 \right] - \right. \\
& \left. - \left( \frac{\partial C_M}{\partial \alpha} \right)_n \bar{m} \frac{s}{r} - (\bar{m}_L + m_{vy}) \left( \frac{\partial C_M}{\partial \frac{\omega_{ar}}{V}} \right)_K - (m_{vx} - m_{vy}) \bar{m}_L \frac{s}{r} \right\} \lambda^2 - \\
& - \left[ \left( \frac{\partial C_M}{\partial \alpha} \right)_n (\bar{m}_L + m_{vx}) - \bar{m}_L \frac{\partial C_L}{\partial \alpha} \frac{s}{r} - C_D (\bar{m}_L + m_{vy}) \frac{s}{r} + \right. \\
& \left. + \left( \frac{\partial C_M}{\partial \frac{\omega_{ar}}{V}} \right)_K \left( \frac{\partial C_L}{\partial \alpha} + C_D \right) \right] \lambda - C_D \left[ \left( \frac{\partial C_M}{\partial \alpha} \right)_n - \left( \frac{\partial C_L}{\partial \alpha} + C_D \right) \frac{s}{r} \right] = 0
\end{aligned}$$

or

$$a\lambda^3 + b\lambda^2 + c\lambda + d = 0. \quad (4.4)$$

This equation is the frequency equation of the system of equations (4.1) and (4.2). Some of the terms are evaluated from the experimental results of the wind tunnel tests conducted under the first part of this project, using the transformations outlined in Progress Report No 12, Sec 3.3.3.10.

3.3.1.3 In Progress Report No 12, the method described above was used to investigate the dynamic stability of a 5 ft Ribless Guide Surface parachute with nominal cloth porosities of 30 and 120 ft<sup>3</sup>/ft<sup>2</sup>-min. During the following reporting period, errors were found in the method, and in Progress Report No 14 the corrected results for the Ribless Guide Surface parachute were presented, together with results of a similar investigation of a Circular Flat parachute with nominal porosity of 120 ft<sup>3</sup>/ft<sup>2</sup>-min and a Ribbon parachute with a geometric porosity of 20% and a prototype nominal diameter of 50 inches.

3.3.1.4 The investigations of the above parachutes were conducted about a position of 0° angle of attack. However, looking at Fig 4-25, Progress

Report No 8, shown here as Fig 4-1, we see that the moment coefficient versus angle of attack curve for the Circular Flat parachute indicates two positions of equilibrium, namely  $0^\circ$  and  $20^\circ$  angle of attack. Further investigation shows that the equilibrium at  $0^\circ$  angle of attack is unstable; i.e., the moments are such that a slight displacement is followed by an increasing displacement (in the wind tunnel investigation of characteristic aerodynamic coefficients, a positive  $C_M$  at positive angles of attack produced a moment restoring the parachute to  $0^\circ$  angle of attack, and a positive  $C_M$  at negative angles of attack caused a further increase in angle of attack. See Fig 4-10, Progress Report No 14). At approximately  $20^\circ$  angle of attack, the parachute is in stable equilibrium, i.e., the moments are such that the parachute returns to  $20^\circ$  if slightly displaced.

3.3.1.5 It is evident that a more meaningful investigation of dynamic stability should be made for the parachute about  $20^\circ$  angle of attack. Therefore, the investigation of the Circular Flat parachute was made at both  $0^\circ$  and  $20^\circ$  angle of attack, using some different assumptions than those made in the original investigation. From Fig 4-11, Progress Report No 14, we see a non-linear variation of  $C_L$  with angle of attack  $\alpha$ . In the original investigation, the analysis was limited to  $0^\circ \leq \alpha \leq 5^\circ$ , where  $C_L$  and  $C_M$  were assumed to be linear.

3.3.1.6 In the present analysis, it was assumed that  $\frac{\partial C_L}{\partial \alpha}$  and  $\frac{\partial C_M}{\partial \alpha}$  have one value in the range  $0^\circ \leq \alpha \leq 10^\circ$  and a different value in the range  $10^\circ \leq \alpha \leq 27.5^\circ$ . Then, from Fig 4-1, where we take tangents to the curve at  $\pm 20^\circ$  and assume an equal but opposite slope through the origin, and

from Figs 4-11 and 4-12, Progress Report No 14, we have for  $0^\circ \leq \alpha \leq 10^\circ$

$$\frac{\partial C_m}{\partial \alpha} = +0.276 \qquad \frac{\partial C_L}{\partial \alpha} = -1.63 \qquad (4.5)$$

and for  $10^\circ \leq \alpha \leq 27.5^\circ$

$$\frac{\partial C_m}{\partial \alpha} = -0.276 \qquad \frac{\partial C_L}{\partial \alpha} = -1.16. \qquad (4.6)$$

These values include corrections for differences in sign convention between theoretical and experimental data.

### 3.3.2 Dynamic Stability about $0^\circ$ Angle of Attack

3.3.2.1 The remaining terms in equation (4.4) above are enumerated in Progress Report No 14, Sec 3.3.3. Substituting these terms and those from equations (4.5) into equation (4.4) we find, for the interval  $0^\circ \leq \alpha \leq 10^\circ$

$$2071.2 \lambda^3 - 224.89 \lambda^2 - 101.73 \lambda - 1.016 = 0. \qquad (4.1a)$$

The roots of equation (4.1a) are found to be

$$\left. \begin{aligned} \lambda_1 &= 0.2861 \\ \lambda_2 &= -0.1677 \\ \lambda_3 &= -0.0097 \end{aligned} \right\} \qquad (4.7)$$

Substituting the above values of  $\lambda$  into the equations (4.3) above yields the equations

$$\left. \begin{aligned} \alpha &= A_1 e^{0.2861 \tau} + A_2 e^{-0.1677 \tau} + A_3 e^{-0.0097 \tau} \\ \phi &= B_1 e^{0.2861 \tau} + B_2 e^{-0.1677 \tau} + B_3 e^{-0.0097 \tau} \end{aligned} \right\} \qquad (4.8)$$

Solving for the arbitrary constants,  $A_i$  and  $B_i$  ( $i = 1, 2, 3$ ) using the initial conditions (at  $t = 0$ ,  $\alpha = \alpha_0 = 30^\circ = 0.0001454$  rad,  $\theta = \theta_0 = 0$ ,  $\omega_\alpha = \omega_\theta = 0$ ) and equation (4.15), Progress Report No 14, and substituting these constants into the equation (4.8), we have (for  $\gamma = vt/r = 48.0 t$ )

$$\begin{aligned}\alpha &= 0.0000564 e^{13.733t} + 0.0000888 e^{-8.05t} - 0.00000012 e^{-0.466t} \\ \theta &= -0.00000169 e^{13.733t} + 0.00000344 e^{-8.05t} - 0.00000336 e^{-0.466t}\end{aligned}\quad (4.9)$$

3.3.2.2 Using the equations (4.9) to describe the motion of the parachute in terms of the vertical and horizontal coordinates ( $X$  and  $Y$ ) and the position angle ( $\alpha + \theta$ ), where (see Progress Report No 12, Sec 3.3.6.5)

$$X = v_0 t \quad (4.10)$$

$$Y = v_0 \int \theta dt, \quad (4.11)$$

we find for  $v_0 = 105$  ft/sec:

$$X = 105 t \quad (4.10a)$$

$$\begin{aligned}Y &= -0.000013 e^{13.733t} - 0.000066 e^{-8.05t} + \\ &\quad + 0.00757 e^{-0.466t} - 0.00749\end{aligned}\quad (4.11a)$$

$$\begin{aligned}(\alpha + \theta) &= 0.0000547 e^{13.733t} + 0.0000939 e^{-8.05t} - \\ &\quad - 0.00000347 e^{-0.466t},\end{aligned}\quad (4.12)$$

3.3.2.3 The equations (4.9), (4.10a), (4.11a) and (4.12) are valid for  $0^\circ \leq \alpha \leq 10^\circ$  by the original assumptions. The values of  $\alpha$  and  $\dot{\alpha}$  as a function of  $t$  are tabulated in Table 4-1 for  $0 \leq t \leq 1.0$  sec. We see that  $\alpha \approx 10^\circ$  after 0.58 sec, and would continue to increase without bound as  $t$  increases if the assumptions remained valid.

### 3.3.3 Dynamic Stability About $20^\circ$ Angle of Attack

3.3.3.1 Again substituting the terms enumerated in Progress Report No 14, Sec 3.3.3, and now using those terms from equation (4.6) in equation (4.4) gives us, for the interval  $10^\circ \leq \alpha \leq 27.5^\circ$

$$2071.1 \lambda^3 + 754.49 \lambda^2 + 216.52 \lambda + 1.9853 = 0. \quad (4.1b)$$

The roots of equation (4.1b) are

$$\left. \begin{aligned} \lambda_1 &= -0.0092 \\ \lambda_2 &= -(0.1774 - 0.2634i) \\ \lambda_3 &= -(0.1774 + 0.2634i) \end{aligned} \right\} \quad (4.13)$$

3.3.3.2 Substituting into the equations (4.5), we have

$$\begin{aligned} \alpha &= A_1 e^{-0.0092\tau} + A_2 e^{-(0.1774 - 0.2634i)\tau} + A_3 e^{-(0.1774 + 0.2634i)\tau} \\ \beta &= B_1 e^{-0.0092\tau} + B_2 e^{-(0.1774 - 0.2634i)\tau} + B_3 e^{-(0.1774 + 0.2634i)\tau} \end{aligned} \quad (4.14)$$

Solving for the arbitrary constants  $A_i$  and  $B_i$  ( $i = 1, 2, 3$ ) using the initial conditions (at  $t = 0$ ,  $\alpha = \alpha_0 = 7.5^\circ = 0.1309$  rad,  $\beta = \beta_0 = 0$ ,  $\dot{\alpha} = \dot{\alpha}_0 = 0$ ) and equation (4.15), Progress Report No 14, we have (for  $\tau = v_0 t / r = 48.0 t$ )

$$\left. \begin{aligned} \alpha &= 0.000157 e^{-0.442t} + 0.161 e^{-0.515t} \sin(12.64t + 54.9^\circ) \\ \beta &= -0.00435 e^{-0.442t} + 0.00486 e^{-0.515t} \sin(-12.64t + 63.9^\circ). \end{aligned} \right\} \quad (4.15)$$

It should be noted in this case that  $\alpha_0 = 7.5^\circ$  represents a displacement of  $7.5^\circ$  from the equilibrium position of  $20^\circ$  angle of attack.

3.3.3.3 Describing the motion of the parachute in terms of the vertical and horizontal coordinates (X and Y) and the position angle ( $\alpha + \beta$ ) we find

$$X = 103t \quad (4.10b)$$

$$Y = 1.032 e^{-0.442t} + 0.0335 e^{-0.515t} \sin(12.64t - 7.99^\circ) - 1.028 \quad (4.11b)$$

$$(\alpha + \beta) = -0.00406 e^{-0.442t} + 0.1654 e^{-0.515t} \sin(12.64t + 54.6^\circ). \quad (4.16)$$

3.3.3.4 Equations (4.15), (4.16) and (4.11b) are tabulated in Table 4-2 for  $0 \leq t \leq 100$  sec. Figure 4-2 presents  $\alpha$  and  $(\alpha + \beta)$  versus  $t$  for  $0 \leq t \leq 1.2$  sec. Figure 4-3 graphically presents the motion of the parachute during descent (note that the scale in the Y direction is considerably larger than that in the X direction). Figures 4-2 and 4-3 may be compared with Figs 4-1 through 4-7 of Progress Report No 15, which present the same information for the Ribbon parachute with 20% geometrical porosity and the Ribless Guide Surface parachutes with nominal porosities of 30 and 120

$\text{ft}^3/\text{ft}^2\text{-min}$ . Again, it should be noted that in Fig 4-2,  $\alpha$  and  $\beta$  are calculated about the  $20^\circ$  angle of attack position.

### 3.3.4 Conclusions

The results of this investigation of the Circular Flat parachute show that:

- A) The condition for weathercock stability, given as

$$\frac{\partial C_m}{\partial \alpha} = \left( \frac{\partial C_m}{\partial \alpha} \right)_h - \left( \frac{\partial C_l}{\partial \alpha} + C_D \right) \frac{S}{r} < 0, \quad (4.17)$$

is not satisfied for the Circular Flat parachute about  $0^\circ$  angle of attack, but is satisfied about  $20^\circ$  angle of attack.

- B) The conditions for dynamic stability, expressed in Routh's criteria as

$$a > 0, b > 0, c > 0, d > 0 \text{ AND } bc > d, \quad (4.18)$$

where  $a$ ,  $b$ ,  $c$  and  $d$  represent the coefficients of the frequency equation (4.4), are not satisfied for  $0^\circ$  angle of attack, but are satisfied for  $20^\circ$  angle of attack.

### 3.3.5 Proposed Work

The dynamic stability of several parachutes with point loads have been presented. Work will now begin to determine the dynamic stability of three parachutes with store. These parachutes are:

- 1) Circular Flat, nominal porosity =  $120 \text{ ft}^3/\text{ft}^2\text{-min}$
- 2) Ribless Guide Surface, nominal porosity =  $120 \text{ ft}^3/\text{ft}^2\text{-min}$
- 3) Ribbon, geometrical porosity = 20%.

### 3.4      **Effective Porosity Studies**

3.4.1      The porosity studies now completed have yielded a wide range of information on the porosity of parachute cloths for sub-critical pressure ratios and altitudes above 50,000 ft. It is now desired to measure porosity at sea level density and at pressure differentials greater than the critical differential pressure for the complete range of air densities.

3.4.2      It is felt that the evaluation of the porosity at pressure ratios above the critical ratio will be of great value in the study of parachute phenomena at supersonic speeds. If the relationship between these high pressure ratios and porosity is known, it may help explain the erratic behavior of parachutes at high speeds.

#### 3.4.3      **New Testing Facility**

3.4.3.1    During the last reporting period, the construction of a facility to determine effective porosity of parachute cloths at sea level density and greater than critical pressure ratios, and to determine effective porosity of ribbon and grid configurations has been completed, and a testing program is being initiated.

3.4.3.2    Figure 4-4 presents a schematic layout of the new facility, and Figs 4-5 and 4-6 are photos of the entire apparatus and the test section, respectively. High pressure air storage is provided by two 130 ft<sup>3</sup> tanks joined to give a total storage capacity of 260 ft<sup>3</sup>, at a pressure of 125 psig. The high pressure air is provided by a two stage Gardner Denver compressor.



Air from the high pressure supply tanks is carried to the test section through a 3 inch diameter pipe, and exhausts from the test section to the atmosphere. The transition section, shown in detailed layout in Fig 4-7, brings the flow from the round pipe to the square test section. Test specimens are held in a metal holder which attaches to the end of the transition section, and the clear plexiglass test section, shown in Fig 4-8, fits around the cloth holder and extends downstream (See Fig 4-9).

3.4.3.3 The mass flow through the test section is determined by a sharp-edged orifice flow meter located just upstream of the transition section (Fig 4-9). A constant pressure ratio is maintained across the test specimen by means of a pneumatically controlled throttling valve which is activated by the pressure regulating system shown schematically in Fig 4-10.

3.4.3.4 Pressure ratios across the flow meter and the test specimen, and pressures necessary to determine densities upstream of the flow meter and test section are recorded through the use of electronic pressure transducers and a Century 809 Recording Light Beam Oscillograph.

#### 3.4.4 Proposed Work

3.4.4.1 The testing program which has been initiated to determine effective porosities of parachute cloths and ribbon and grid configurations at sea level density and at greater than critical pressure ratios will be continued.

3.4.4.2 The effort to find some correlation between the effective

porosity of the wire screens which were tested previously and the geometric properties of the screens will be continued. It is hoped that this will lead to the characteristic dimensions of the screens, and eventually of cloths, so that a meaningful relationship between effective porosity and Reynolds number can be found.

TABLE 4-2. COORDINATES OF PARACHUTE SYSTEM DURING DESCENT

STABILITY ABOUT  $\alpha = 20^\circ$

CIRCULAR FLAT NOM. POR. = 120 FT <sup>3</sup> /FT <sup>2</sup> -MIN			
t (SEC)	$\alpha$ (°)	$\alpha + \beta$ (°)	Y (FT)
0	7°30'	7°30'	0
.01	7°27'	7°25'	-.0006
.02	7°14'	7°11'	-.0017
.03	6°55'	6°50'	-.0032
.04	6°30'	6°23'	-.0054
.05	6°00'	5°51'	-.0080
.06	5°25'	5°18'	-.0112
.07	4°54'	4°41'	-.0149
.08	4°18'	4°06'	-.0188
.09	3°43'	3°28'	-.0230
.10	3°08'	2°53'	-.0276
.20	-34'	-50'	-.0792
.30	-43'	-56'	-.1253
.50	7'	-5'	-.2003
.70	0	-11'	-.2705
1.0	0	-8'	-.3644
1.5	0	-8'	-.4850
2.0	0	-6'	-.6020
3.0	0	-4'	-.7530
5.0	0	-2'	-.9140
10.0	0	C	-1.016
20.0	0	0	-1.028
30.0	0	0	-1.028
100.0	0	0	-1.028

TABLE 4-1. COORDINATES OF PARACHUTE SYSTEM DURING DESCENT

STABILITY ABOUT  $\alpha = 0^\circ$

CIRCULAR FLAT NOM. POR. = 120 FT <sup>3</sup> /FT <sup>2</sup> -MIN		
t (SEC)	$\alpha$ (°)	Y (FT)
0	30°	0
.1	5'	-.00004
.2	8'	-.00020
.3	12'	-.00062
.4	50'	-.00319
.5	3°5'	-.01246
.55	6°10'	-.02482
.58	9°20'	-.03724
.6	12°12'	-.04900
.63	10°40'	-.07392
.635	19°45'	-.07915
.6358	20°0'	-.08003
.7	48°20'	-.19300
.8	190°55'	-.76229
.9	4π+34°	-3.00975
1.0	16π+96°	-11.88110

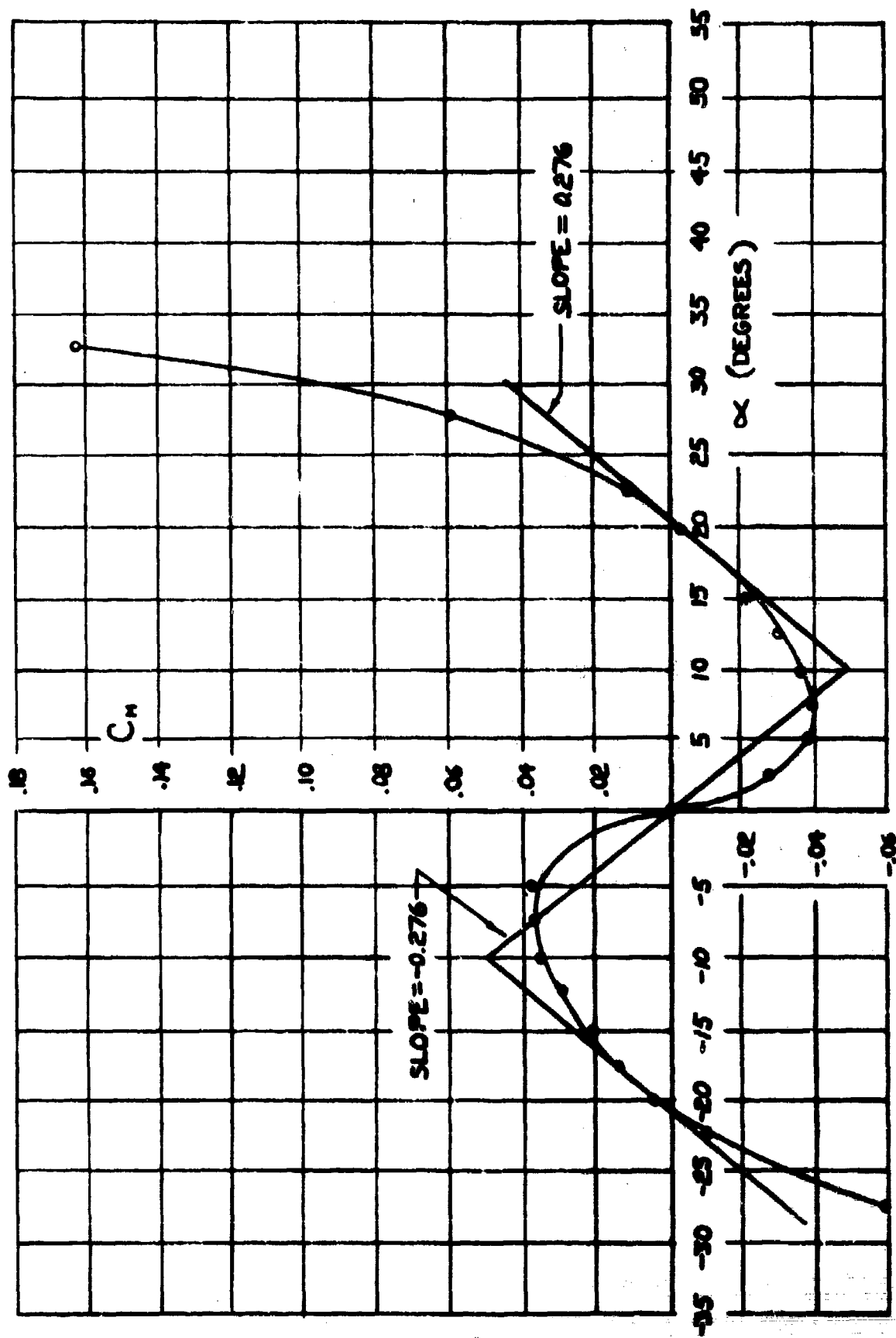
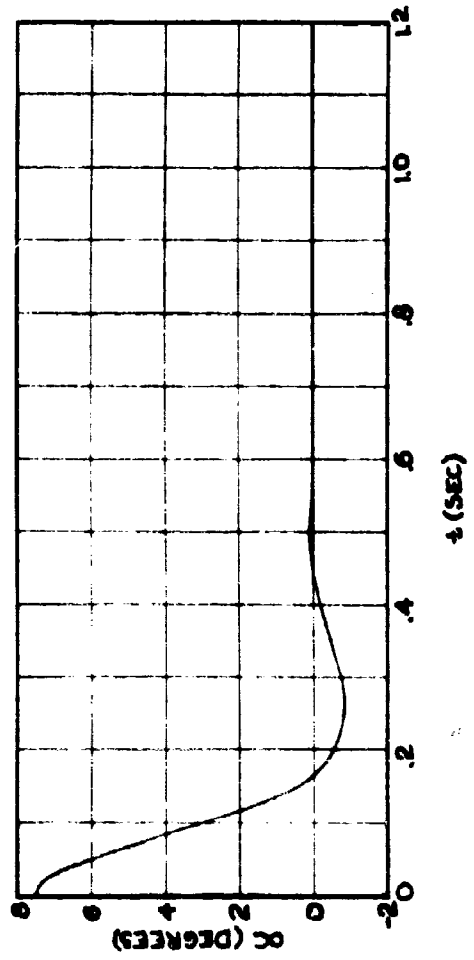


**FIG 4-1. MOMENT COEFFICIENT VS ANGLE OF ATTACK FOR CIRCULAR  
FLAT FABRIC PARACHUTE**  
( $Re = 6 \times 10^6$ , FABRIC MATERIAL: 1.1 OZ, 40 LB NYLON RIPSTOP, NOM POR = 120 FT<sup>2</sup>/MIN-FT.)

$$\alpha = .000144 e^{-.446t} + .1606 e^{-.8515t} [\sin(12.64t + 54^{\circ} 26')] ]$$



$$\alpha + \beta = -.0042 e^{-.446t} + .1630 e^{-.8515t} [\sin(12.64t + 55^{\circ} 56')] ]$$

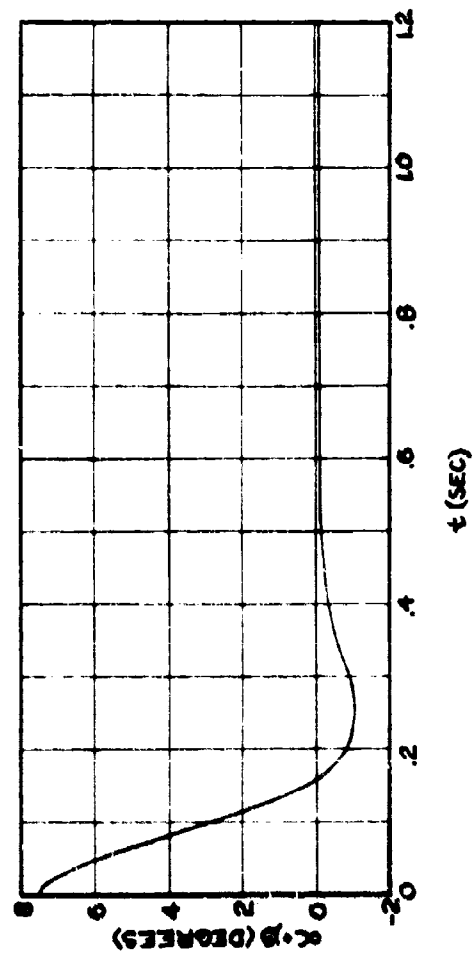


FIG 4-2. STABILITY ABOUT 20° ANGLE OF ATTACK  
 ANGLE OF ATTACK (α) AND ANGLE OF DESCENT (α + β) FOR  
 CIRCULAR FLAT PARACHUTE WITH NOM. POR. = 120 FT<sup>2</sup>/FT<sup>2</sup>-MIN.  
 INITIAL CONDITIONS: V<sub>0</sub> = 105 FT/SEC, α<sub>0</sub> = 7.5°, β<sub>0</sub> = 0, ω<sub>z0</sub> = 0

$$Y = 1.032 e^{-.446t} + .0335 e^{-.8515t} [\sin(12.64t - 7^{\circ} 28')] ] - 1.028$$

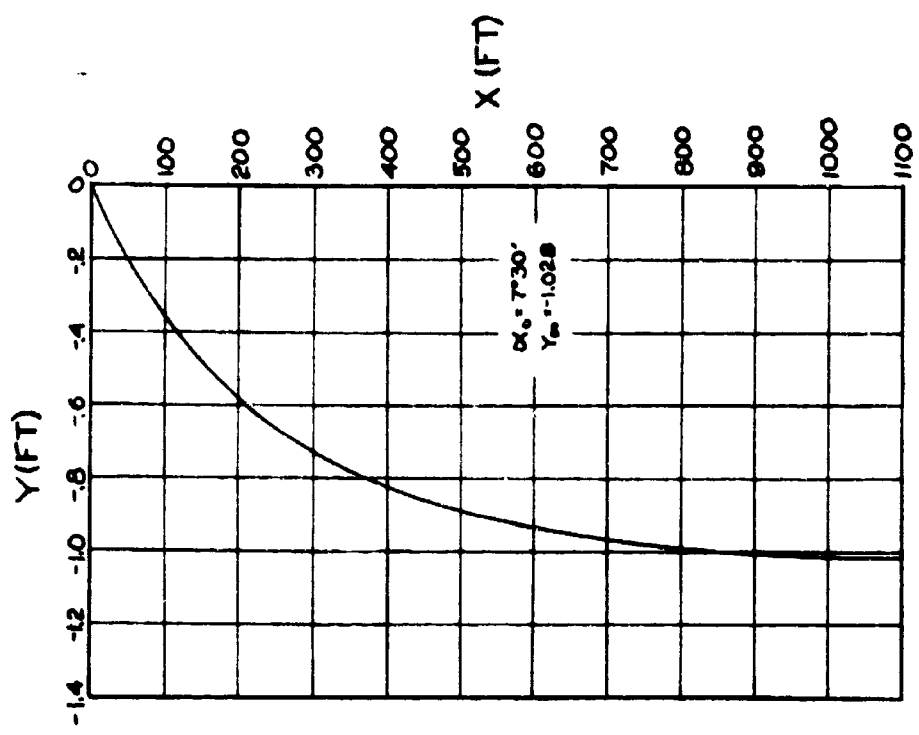


FIG 4-3. GRAPHICAL PRESENTATION OF MOTION  
 DURING DESCENT OF A CIRCULAR FLAT  
 PARACHUTE WITH NOMINAL POROSITY =  
 120 FT<sup>2</sup>/FT<sup>2</sup>-MIN.  
 (INITIAL CONDITIONS : V<sub>0</sub> = 105 FT/SEC, α<sub>0</sub> = 0, ω<sub>z0</sub> = 0)  
 (STABILITY ABOUT α = 20°)

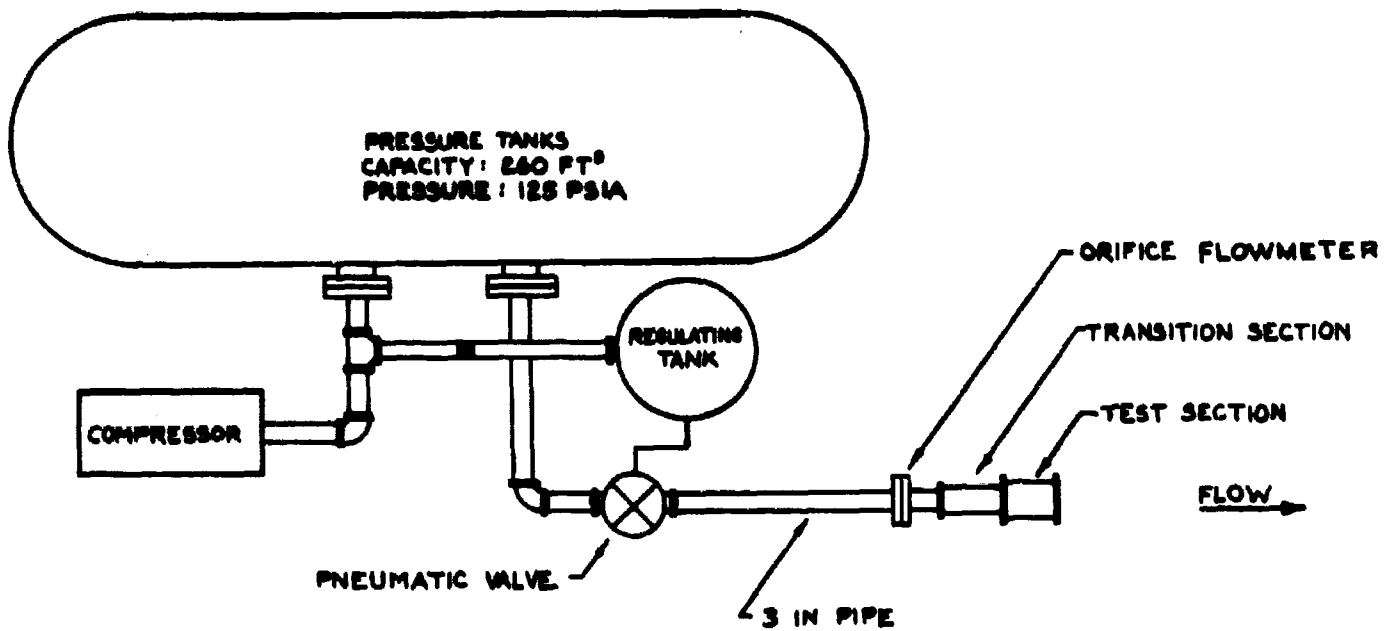


FIG 4-4. SCHEMATIC LAYOUT OF POROSITY TEST APPARATUS

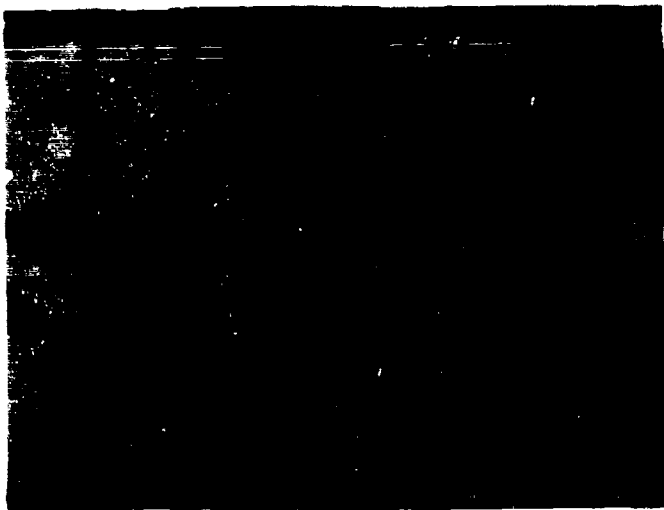


FIG 4-5. POROSITY TESTING FACILITY

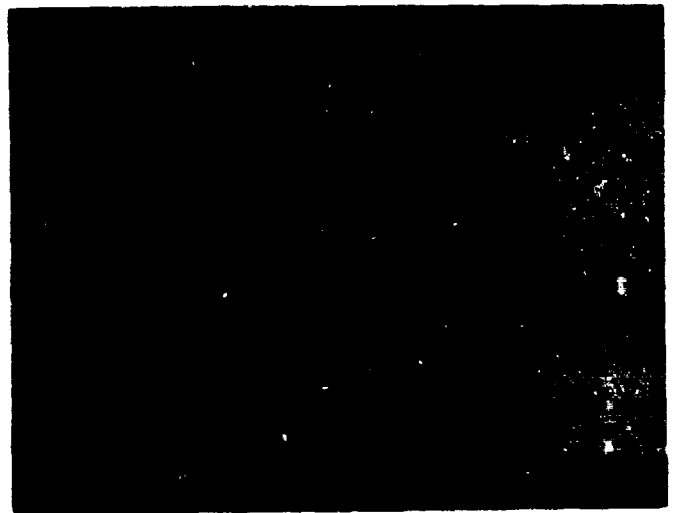


FIG 4-6. TEST SECTION OF POROSITY TESTING FACILITY

AD605978

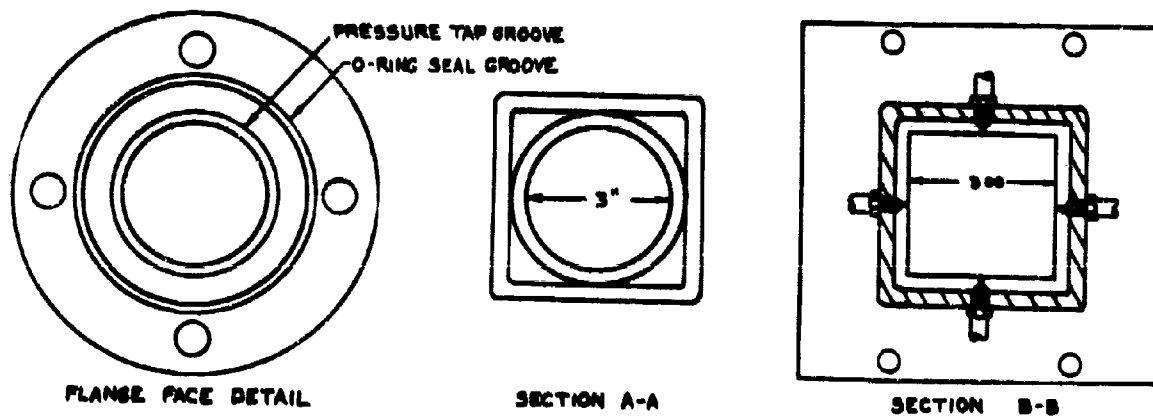


FIG 4-7. DETAIL LAYOUT OF TRANSITION SECTION ( $\frac{1}{8}$  SCALE)

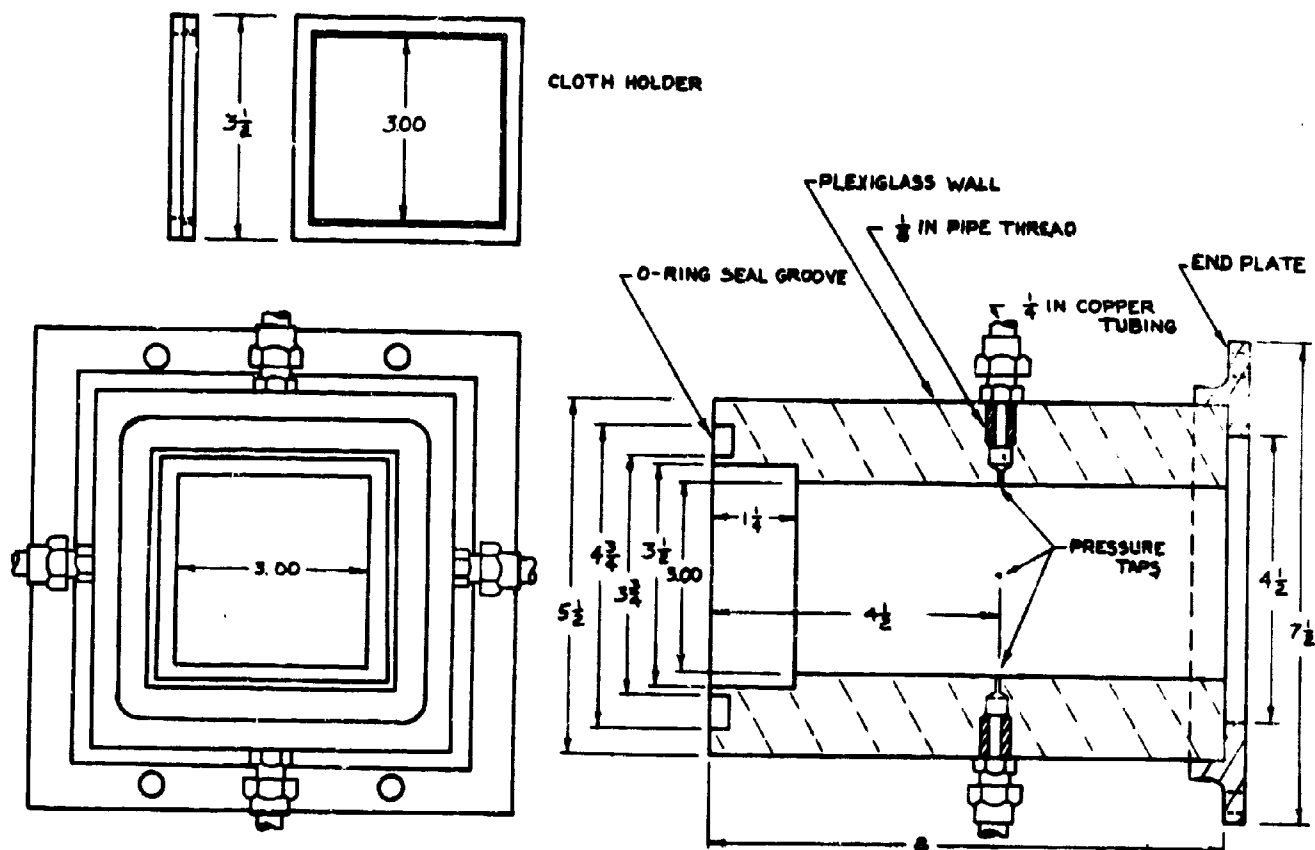


FIG 4-8. DETAIL LAYOUT OF TEST SECTION ( $\frac{1}{8}$  SCALE)

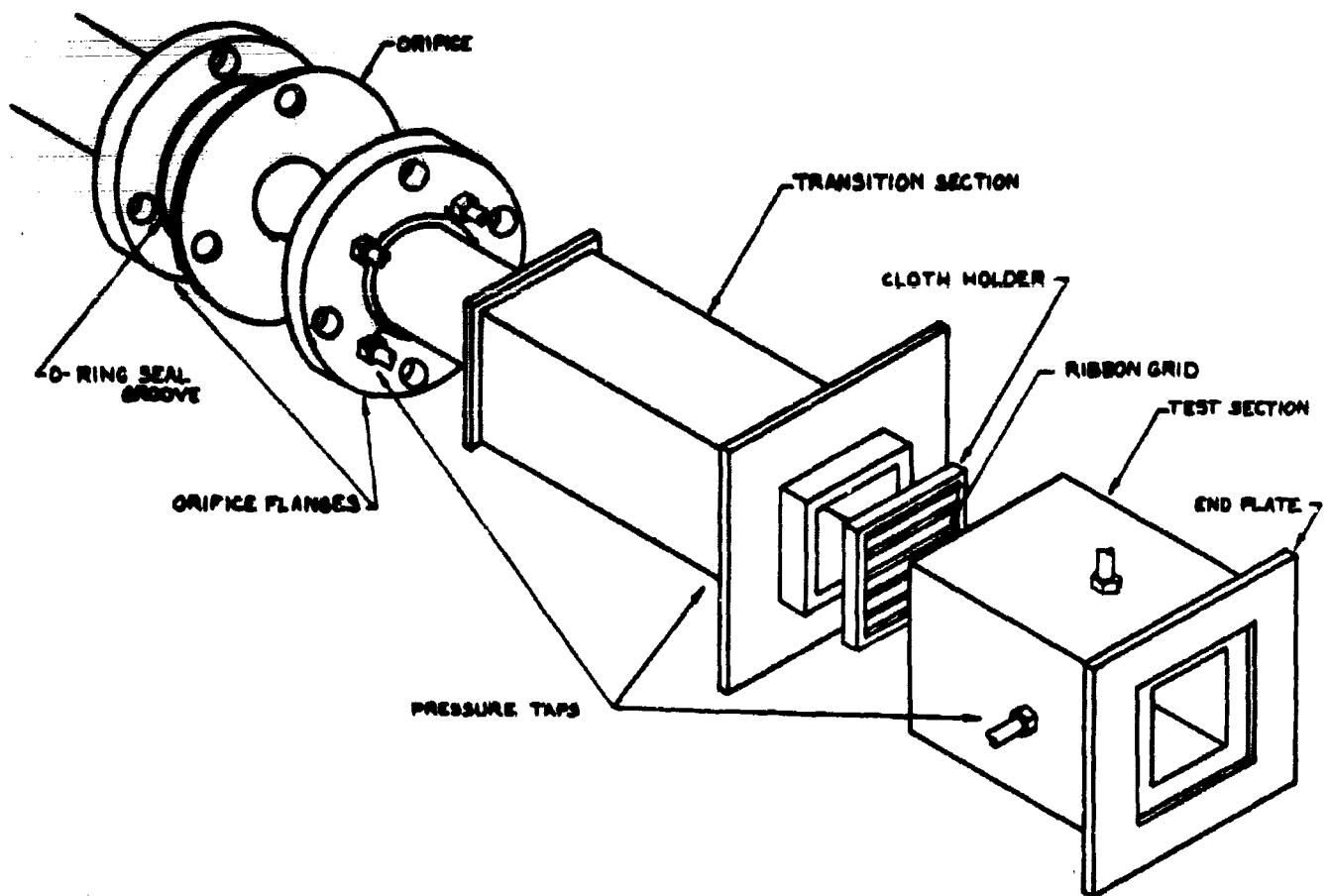


FIG 4-9 EXPLODED VIEW OF FLOWMETER TRANSITION SECTION AND TEST SECTION

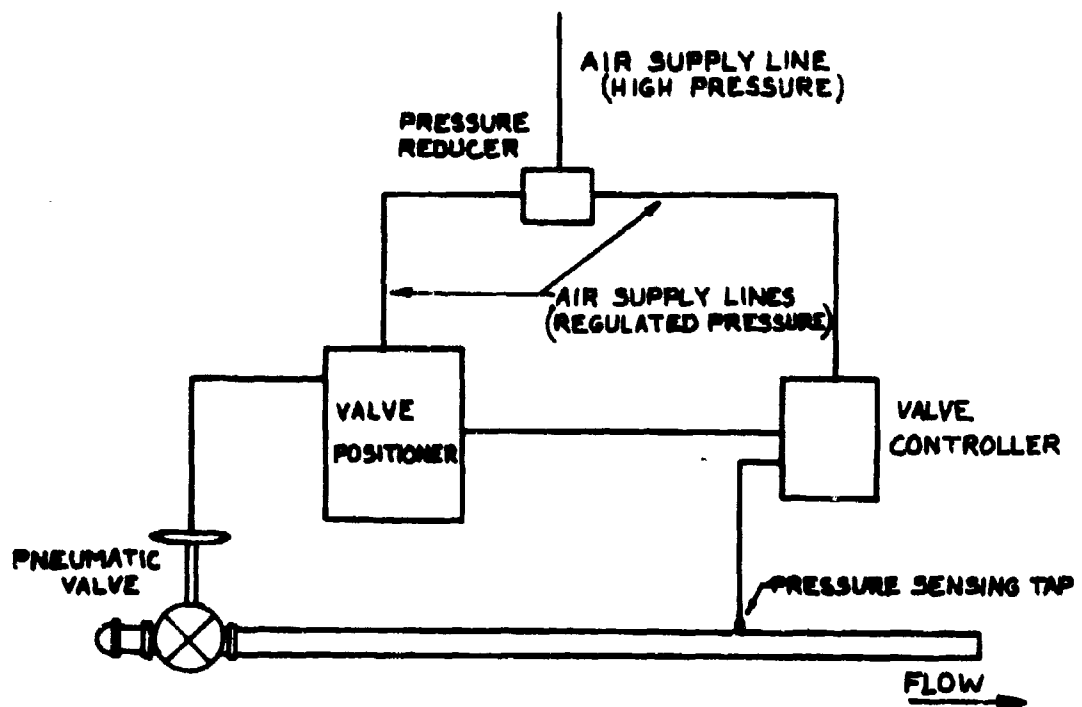


FIG 4-10 SCHEMATIC DIAGRAM OF VALVE CONTROL OPERATION



Project No 6

4.0      Determination of the Minimum Sized Parachute for Stabilization  
of General Aerial Delivery Cargo

4.1      The draft of the final technical report of this project has been completed, and is currently being reviewed.

## Project No 7

### 5.0      Theoretical Study of Supersonic Parachute Phenomena

#### 5.1      Introduction

5.1.1      It is known that conventional parachutes of all types perform more or less satisfactorily in subsonic flow, but become unstable and unsatisfactory retardation devices in supersonic flow. In an attempt to explain this phenomenon, rigid parachute models were studied in supersonic flow and high speed Schlieren photographs were taken. These photographs revealed a highly unstable shock pattern ahead of the canopy. Similar tests of flexible models showed irregular oscillation, structural instability, and eventual destruction of the canopy.

5.1.2      The analysis of the conventional parachute in supersonic flow, and the subsequent development and testing of a supersonic retardation device proceed in the following phases:

- 1) Pressure distribution studies on conventional canopy in supersonic flow
- 2) Water analogy studies in conventional water tow
- 3) Water analogy studies in water table with stationary models
- 4) Wind tunnel stability studies of supersonic parachutes
- 5) Drag studies of supersonic parachutes.

These phases will be reported in respective order in the following sections of this report.

## 5.2 Pressure Distribution Studies in Supersonic Wind Tunnel

5.2.1 As a first step in the analysis of conventional parachutes, the pressure distribution on both the inside and outside surfaces of a conventional ribbon parachute model suspended in the wake of an ogive cylinder forebody was studied. Model geometry, test arrangement, and pressure distribution for Mach numbers of 0.8, 1.2, and 4.5 were presented in Progress Report No 12. Pressure distributions for Mach 3.0 were given in Progress Report No 15.

5.2.2 During this reporting period, tests were made to determine the influence of the ogive-cylinder forebody on the internal and external pressure distributions on the canopy at Mach numbers of 1.08 and 3.0. These tests were made with and without suspension lines, in order to determine their effect on pressure distribution. Previously, the transonic tests were made at Mach 1.2; however, in the wind tunnel now being used, the highest attainable Mach number with the model mounted in the test section was Mach 1.08. Therefore, the transonic studies were continued at this Mach number.

5.2.3 The parachute models and testing procedure were the same as in previous studies. As before, two secondary parachute models were used, one to measure internal and the other to measure external pressures. The suspension lines for these tests were secured at the confluence point by a set of guy wires fastened to the tunnel walls (see Fig 7-1). The pressures were measured on a multiple manometer and photographed during each test. Three tests were conducted for each configuration at both Mach numbers.

### 5.2.4 Results

5.2.4.1 The pressure measurements from three internal and three external pressure distribution tests were averaged in each case. These measurements were then reduced to coefficient form with the pressure coefficient,  $C_p$ , defined as

$$C_p = \frac{P_L - P_S}{q},$$

where  $P_L$  = local pressure on the surface of the model

$P_S$  = free stream static pressure

$q$  = free stream dynamic pressure.

5.2.4.2 Figures 7-2 and 7-3 present the pressure coefficient distribution of the parachute model in free stream with and without suspension lines, respectively, at transonic Mach numbers. For comparison, Fig 7-4 presents these two sets of curves together with the pressure distribution of the model with suspension lines behind an ogive-cylinder forebody (previously presented as Fig 7-11, Progress Report No 12). Similarly, Figs 7-5 through 7-7 present the same sequence of pressure coefficient distributions at Mach 3.0. It is seen that the forebody has only a small influence on either the internal or external pressure coefficient at Mach 1.08 and 3.0. The suspension lines do have noticeable influence on the magnitude of the internal pressure coefficient, especially at Mach 3.0. This increase in internal pressure coefficient is due to the large pressure recovery across the well defined shock ahead of the canopy without suspension lines (see Sec 5.2.4.3). The suspension lines do not noticeably influence the external pressure coefficient at either Mach number.

5.2.4.3 Figures 7-8 and 7-9 are double exposure shadowgraphs of the flow pattern at Mach 3.0 about a parachute model in free stream with and without suspension lines, respectively. It is seen that apparently the suspension lines cause a highly irregular shock pattern ahead of the canopy. In tests without suspension lines, a stable detached shock wave pattern is formed. However, this contradicts previous experience, and efforts are now being made to explain this contradiction, as outlined in Sec 5.2.5.1 below.

### 5.2.5 Proposed Work

5.2.5.1 The pressure distribution studies as specified in the present contract have been completed. However, during the next reporting period, additional wind tunnel tests of several canopies with varying porosities and different methods of mounting will be made to determine the factors which influence the character of the shock wave ahead of the canopy without suspension lines. These tests will be conducted at Mach numbers of 2.0 and 3.0.

5.2.5.2 During the next reporting period, work will begin on the writing of a final report for this phase of the project.

### 5.3 Water Tow Studies

5.3.1 As a second phase of the investigation, a series of two-dimensional water analogy studies have been made to visualize flow patterns within the canopy. These studies were applied first to the analysis of the instability of conventional parachutes, reported in Progress Report No 12, and later to stability studies of various configurations of the so-called spiked parachute, reported in the Supplement to Progress Report No 13.

5.3.2 During this reporting period, a series of tests was performed at Mach 2.0 with the spiked parachute behind an ogive-cylinder forebody with a caliber of 2.5. Tests were run at L/D ratios of 4.5 and 8. The ratio of the parachute model maximum diameter to the forebody diameter was 2.

### 5.3.3 Results

Figures 7-10 and 7-11 show the flow pattern about the spiked parachute behind the forebody (see Progress Report No 15, Fig 7-5, for identification of parameters). For comparison, Fig 7-12 shows the flow pattern about the model in free stream at Mach 2.0. It is seen that the flow patterns are somewhat less defined for the parachute in the wake of the forebody but similar in nature. The stability seems to be unaffected.

### 5.3.4 Proposed Work

Water analogy experiments will be continued in close coordination with supersonic wind tunnel tests of the spiked parachute. Making use of existing property analogies (derived in Progress Report No 1), attempts will be made to determine pressure distribution and relative drag of retardation devices in the water tow tank.

## 5.4 Stationary Model Water Analogy Studies

5.4.1 The advantages of complementing the conventional water tow experiments with studies in a moving water channel were enumerated in Progress Report No 15. Desirable features for the projected facility were indicated and the detail design was begun.

5.4.2 During this reporting period, the design of the main component

parts of the new water channel, including the structural framework and the water ducting and reservoir, was completed. Bids for the construction of these parts were received from local machine shops, but acceptance of a bid was delayed because of the termination of the present contract. Upon authorization in the new contract, a bid will be accepted.

#### 5.4.3      A Description of the New Water Channel

5.4.3.1    Figure 7-13 is a general assembly drawing of the proposed facility, and shows the main features and dimensions. The main components will be described in the following paragraphs of this report.

#### 5.4.3.2    Main Channel and Supporting Structure

The rectangular channel is approximately 20 ft long, 52 inches wide, and 5 inches deep. The channel floor consists of one piece of high grade, mirror finish plate glass 15 ft long and  $\frac{1}{2}$  inch thick. The glass rests on plexiglass support pads mounted on adjustable swivel screws used for fine adjustment in levelling the surface of the glass.

The vertical side walls of the channel are made of 6 x 3 1/2 x 3/8 inch right angle structural steel attached to the top chord of the supporting structure. The channel is supported by two parallel steel trusses 2 1/2 ft deep; its top chords consist of 4 x 2 1/2 inch steel channel sections running the entire length of the structure. The lower chord is made 4 ft shorter at the downstream end of the channel to provide space for the pump and motor drive. At 2 1/2 ft intervals, there are cross ties joining the two top and the two bottom chords. The swivel screws and plastic pads

which support the glass floor of the channel are screwed at intervals into the tie between the top chords. Ties at the lower panel joints support the water supply pipe and ducting. Horizontal diagonal bracing members were avoided in order to have large, unobstructed panels directly beneath the glass floor for photographic purposes.

#### 5.4.3.3 Channel Tilting Mechanism

A uniform slope of the channel is necessary to secure uniform flow velocity. This slope must be adjustable in order to attain the water flow velocity representing a certain Mach number. Variation of the longitudinal slope of the channel is provided by means of the tilting mechanism illustrated in Fig 7-13. At the downstream end of the lower chord, the trusses are mounted on hinge pins. Near the upstream end of the channel, a 1 inch diameter bar is welded transversely to the bottom of the upper chord members. This bar will be carried by two hydraulic rams, one on each side. The hydraulic rams are connected to a hand operated hydraulic pump by means of flexible pressure tubing and shut-off valves. The hydraulic rams have a graduated travel; they can be operated in unison or independently to obtain the desired longitudinal slope and transverse levelling of the channel.

#### 5.4.3.4 Water Supply System

The water supply and storage system consists of a steel tank  $10\frac{1}{2}$  x 3 x  $2\frac{1}{4}$  ft with a capacity of 500 gallons, placed on the floor at the downstream end of the channel so that its length is perpendicular to the channel's longitudinal axis. The pumping equipment consists of a  $7\frac{1}{2}$  hp Westinghouse constant speed, three phase induction motor driving a Worthington Centrifugal pump rated at 250 gallons per minute and a total head of 45 ft.



The motor and pump are mounted on a bed plate set transversely under the downstream cantilever portion of the truss as shown in Fig 7-13. The discharge side of the pump feeds into a short flanged diffusing section which increases the diameter from 4 to 6 inches. The water flows through a 6 inch Walworth gate valve to regulate the flow, and then to a rubber expansion joint which takes up the displacement resulting from tilting of the table and prevents the vibrations of the pump from being transferred to the trusses. The water then flows through a sequence of diffusers and 90 degree bends until it reaches the nozzle approach section which has a constant cross section of 4 x 52 inches. The nozzle approach section is provided with a large removable framed panel for observation of the flow, and incorporates flow straighteners. It leads to the variable nozzle which will be made of a  $\frac{1}{4}$  inch thick aluminum plate hinged to the top of the approach section and converging to any desired opening at the lip. The rotation of the variable nozzle plate about its hinge, which controls the amount of nozzle opening, is controlled by a hand operated gear and lever mechanism.

The water flow from the channel returns to the reservoir by overflowing the downstream end of the channel.

#### 5.4.4 Proposed Work

5.4.4.1 As soon as the necessary authorization from the contracting agency is received, the order for the fabrication of the water channel structural framework, water ducting, and reservoir will be issued to the local machine shop that submitted the best bid.

5.4.4.2 Work will proceed on the detail design of the variable nozzle

mechanism and instrumentation of the water channel, including a depth gage, traversing gear and shadowgraph system. Simultaneously, the available components such as the electric motor, starter switch, water pump, etc, will be readied for installation.

5.4.4.3 As soon as the structure, ducting and reservoir are delivered and the other component parts received, the water channel and component parts will be assembled and carefully aligned in preparation for calibration and initial testing.

## 5.5 Wind Tunnel Stability Tests of Supersonic Parachutes

5.5.1 Utilizing the knowledge obtained from the first two phases of investigation, a retardation device was designed for efficient operation in supersonic flow. Stability studies of this spiked parachute have previously been conducted at Mach numbers of 2.0 and 3.0, as reported in Progress Reports Nos 14 and 15.

5.5.2 Initially, rigidly mounted models were tested at Mach 2.0. The configurations which appeared stable were then tested so that they were free to oscillate and rotate ("pendulum" tests), and it was verified that configurations which were stable when rigidly mounted were also stable when free to oscillate and rotate (see Progress Report No 14, Sec 6.2.1 and 6.2.2). Tests at Mach 3.0 revealed that a larger cone angle was needed to obtain configurations which were stable. The cone half angle was increased from  $20^{\circ}$  to  $34^{\circ}$ , tests were repeated, and stable configurations were found at Mach 3.0.

5.5.3 During this reporting period, tests were conducted to determine

whether the two configurations which were stable at Mach 3.0 were also stable at lower Mach numbers. These tests were made at Mach numbers of 2.0 and 1.14. Models, testing procedure, and sequence of events were the same as in previous studies.

5.5.4 It was feared that the addition of suspension lines to a stable configuration might disturb the flow pattern and cause the configuration to become unstable. Therefore, a model with suspension lines was built (see Fig 7-14). The diameter of the suspension lines is  $1/6$  of maximum canopy diameter. This model was tested at Mach numbers of 1.06, 2.0 and 3.0.

#### 5.5.5 Results

5.5.5.1 Figures 7-15 and 7-16 are Schlieren photos at Mach 2.0 of the two configurations which were stable at Mach 3.0. These configurations are stable, but to a lesser degree than the same configurations with a  $20^\circ$  half-angle cone at Mach 2.0. It was also found that the two configurations which were stable at Mach 3.0 were highly stable at Mach 1.14.

5.5.5.2 Figure 7-17 is a Schlieren photo of the spiked parachute with suspension lines at Mach 3.0. It is seen that in this case the suspension lines do not influence the flow patterns, nor do they affect the stability. This was also true at Mach numbers of 1.06 and 2.0.

#### 5.5.6 Proposed Work

5.5.6.1 A flexible model of a stable configuration of the spiked parachute suitable for testing in a supersonic wind tunnel is presently being fabricated.

During the next reporting period, this model will be tested at Mach numbers of 1.14, 2.0 and 3.0 to determine its stability characteristics.

5.5.6.2 A flexible and a rigid model of the supersonically stable spiked parachute with nominal diameters of 12 inches are being fabricated for subsonic investigation at Mach 0.2. The subsonic stability characteristics will be determined as normal and tangent forces and moment versus angle of attack.

## 5.6 Drag Studies of Supersonic Parachute

5.6.1 During the previous reporting period, several tests were made to determine the drag coefficient of various configurations of the spiked parachute at Mach 3.0, and the results were presented in Progress Report No 15, Sec 6.7.2. During this reporting period, a more extensive series of drag tests were made at Mach 3.0, as well as at Mach numbers of 1.06, 1.14 and 2.0. Figure 7-20 in Progress Report No 15 illustrates the method of mounting the models in the test section for the tests at Mach numbers of 1.06, 2.0, and 3.0, and Fig 7-18 in this report illustrates the test arrangement for drag studies at Mach 1.14. The apparatus shown in Progress Report No 15 was also modified so that the drag of the cone with the canopy positioned behind it could be measured. An electrical strain gage type drag balance was used to record drag data.

5.6.2 The two stable configurations of the spiked parachute were tested at various Mach numbers in these drag studies, as was the model with suspension lines (See Sec 5.5.4 above). In addition, the drag of the 20° half-angle cone alone was measured at Mach numbers of 1.06 and 2.0, and the drags

of the  $34^\circ$  half-angle cone alone and of the canopy alone were measured at Mach numbers of 1.06, 2.0, and 3.0. Several other configurations, both stable and unstable, were tested for drag, using both the  $20^\circ$  and  $34^\circ$  half-angle cones.

### 5.6.3 Results

5.6.3.1 Figure 7-19 presents the drag coefficient,  $C_D$ , of the two supersonically stable configurations versus Mach number based on canopy surface area (see Fig 7-5, Progress Report No 15 for identification of parameters). The sharp peak in drag at transonic Mach numbers is characteristic of all drag producing bodies. However, this peak does not show up for all bodies presented here due to lack of tests over the transonic range. Figure 7-20 shows the drag coefficient of the  $20^\circ$  half-angle cone alone (based on projected area) and with a canopy positioned behind it at various Mach numbers, and Fig 7-21 presents the same information for a  $34^\circ$  half-angle cone. Figure 7-22 presents the drag coefficient of the canopy alone at various Mach numbers. Figures 7-23 through 7-25 present the drag coefficient versus cone location for transonic Mach numbers, Mach 2.0 and Mach 3.0, respectively. These drag coefficients are based on the canopy surface area. Figure 7-26 presents the drag coefficient of the various configurations versus Mach number, based on the total surface area in the configuration. It is believed that the drag coefficient of the complete configuration can be improved through reduction of the surface area (see Sec 5.6.4).

5.6.3.2 As illustrated in Figs 7-20 and 7-21, the presence of a canopy behind the cone greatly decreases the drag of the cone; in fact, drag

measurements of the  $20^\circ$  half-angle cone at Mach 2.0 revealed thrust instead of drag. It was concluded that the presence of the canopy produces a relatively high base pressure on the cone. As seen in Figs 7-23 through 7-25, the drag coefficient of the model with suspension lines is about 16% higher at Mach 1.04 and 10% higher at Mach 3.0 than the drag coefficients of the same model without suspension lines. From Figs 7-23 and 7-24, it is seen that stable configurations with a  $34^\circ$  half-angle cone have higher drag than the equivalent configurations with a  $20^\circ$  half-angle cone.

#### 5.6.4 Proposed Work

As mentioned in Progress Report No 15, Sec 6.7.3.2, an attempt is being made to improve the drag efficiency of the spiked parachute by decreasing the surface area of the canopy. Supersonic wind tunnel drag tests of these revised models will be conducted during the next reporting period.

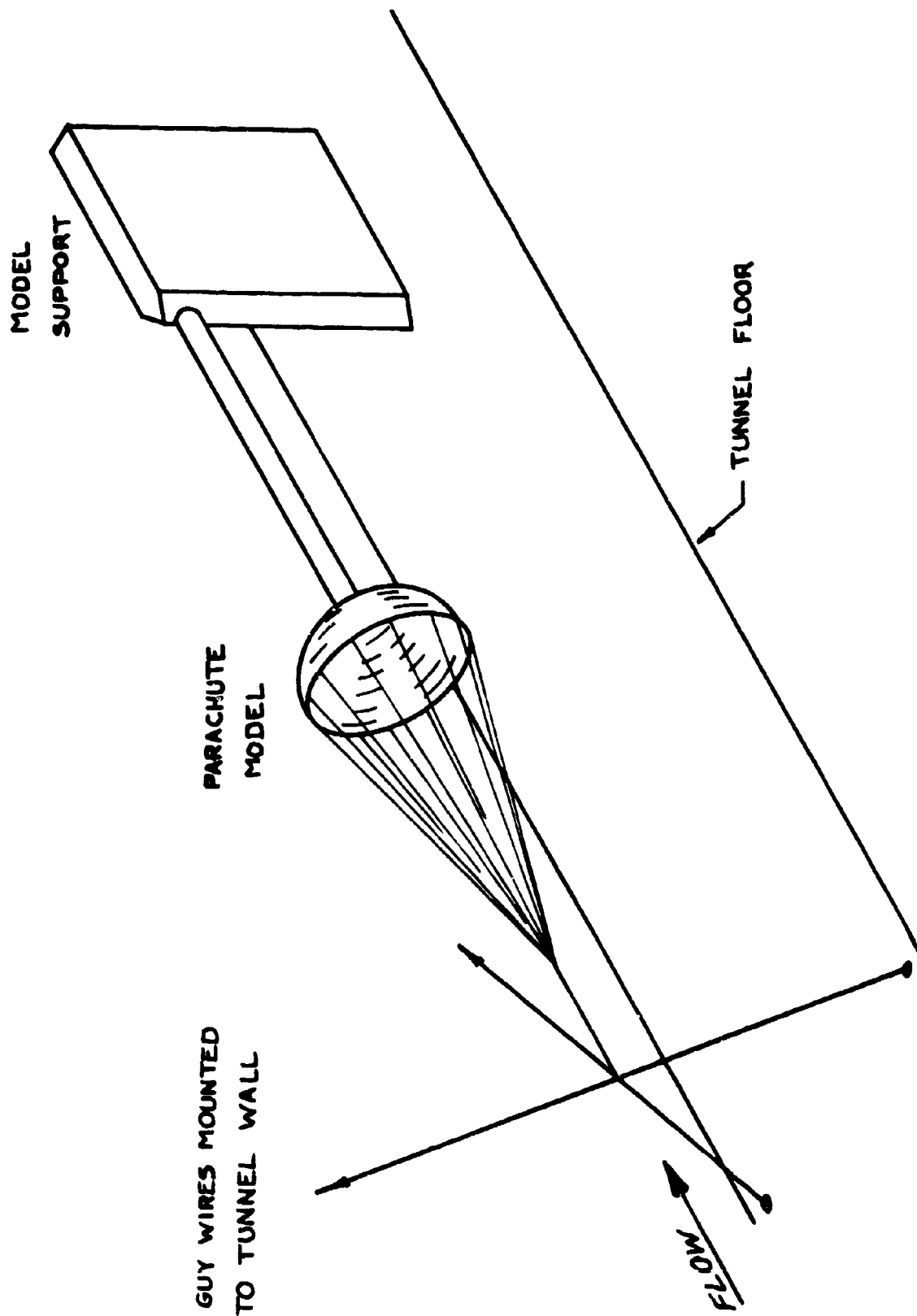


FIG 7-1. TEST ARRANGEMENT FOR PRESSURE DISTRIBUTION STUDIES WITHOUT A FOREBODY AT MACH NUMBERS OF 1.08 AND 3.0

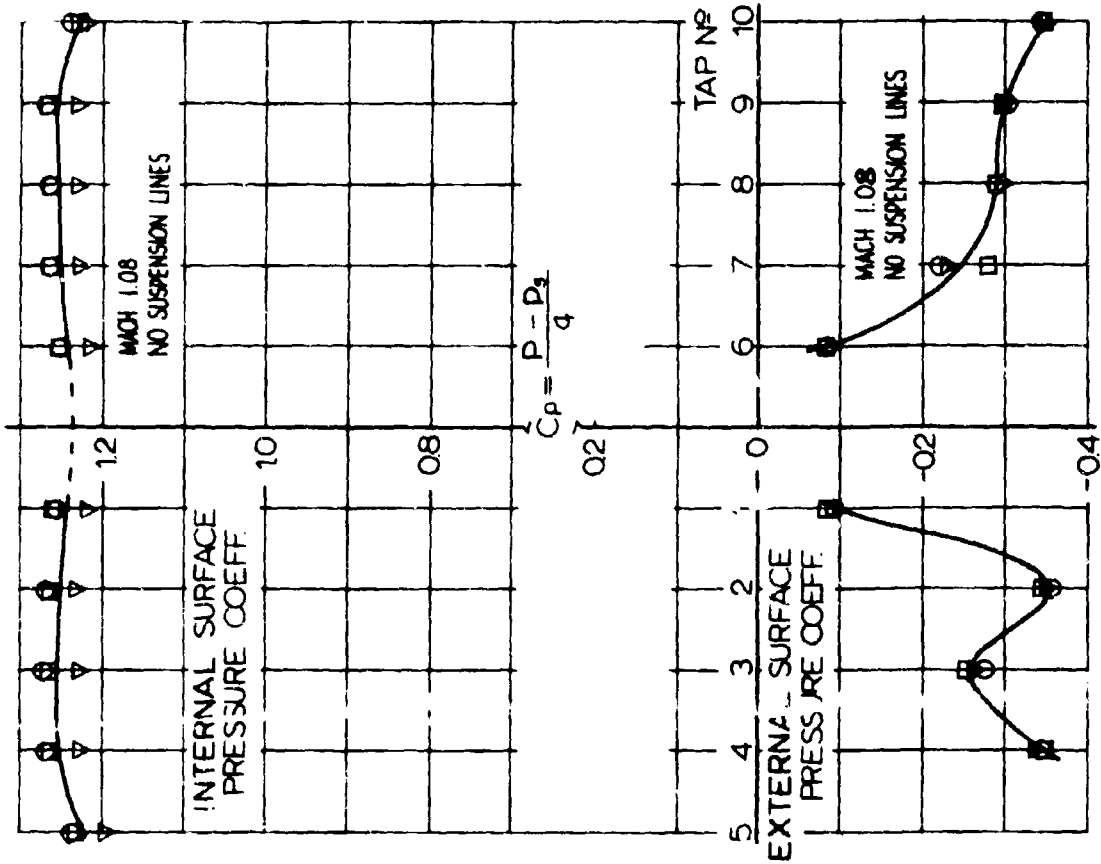


FIG 7-3. PRESSURE COEFFICIENT DISTRIBUTION OF A 26% POROSITY RIBBON PARACHUTE MODEL IN FREE STREAM WITHOUT SUSP. LINES AT TRANSONIC MACH NUMBERS

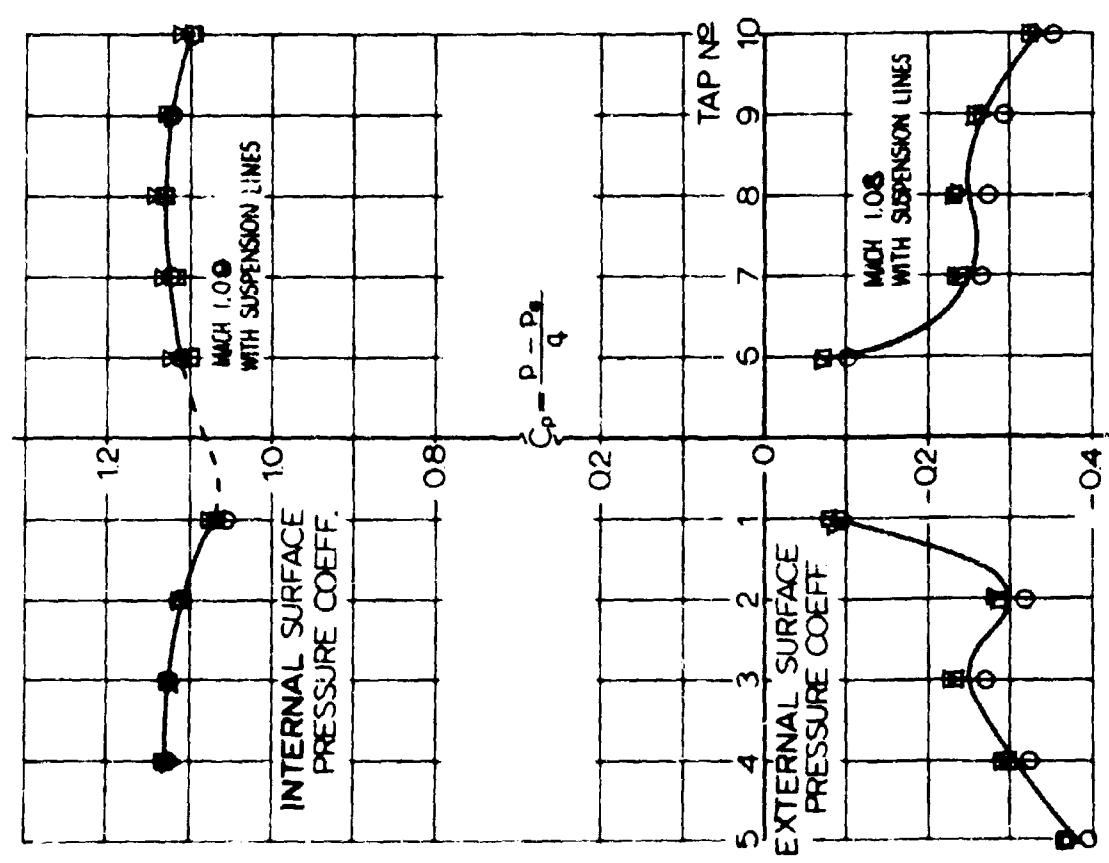


FIG 7-2. PRESSURE COEFFICIENT DISTRIBUTION OF A 26% POROSITY RIBBON PARACHUTE MODEL IN FREE STREAM WITH SUSPENSION LINES AT TRANSONIC MACH NUMBERS



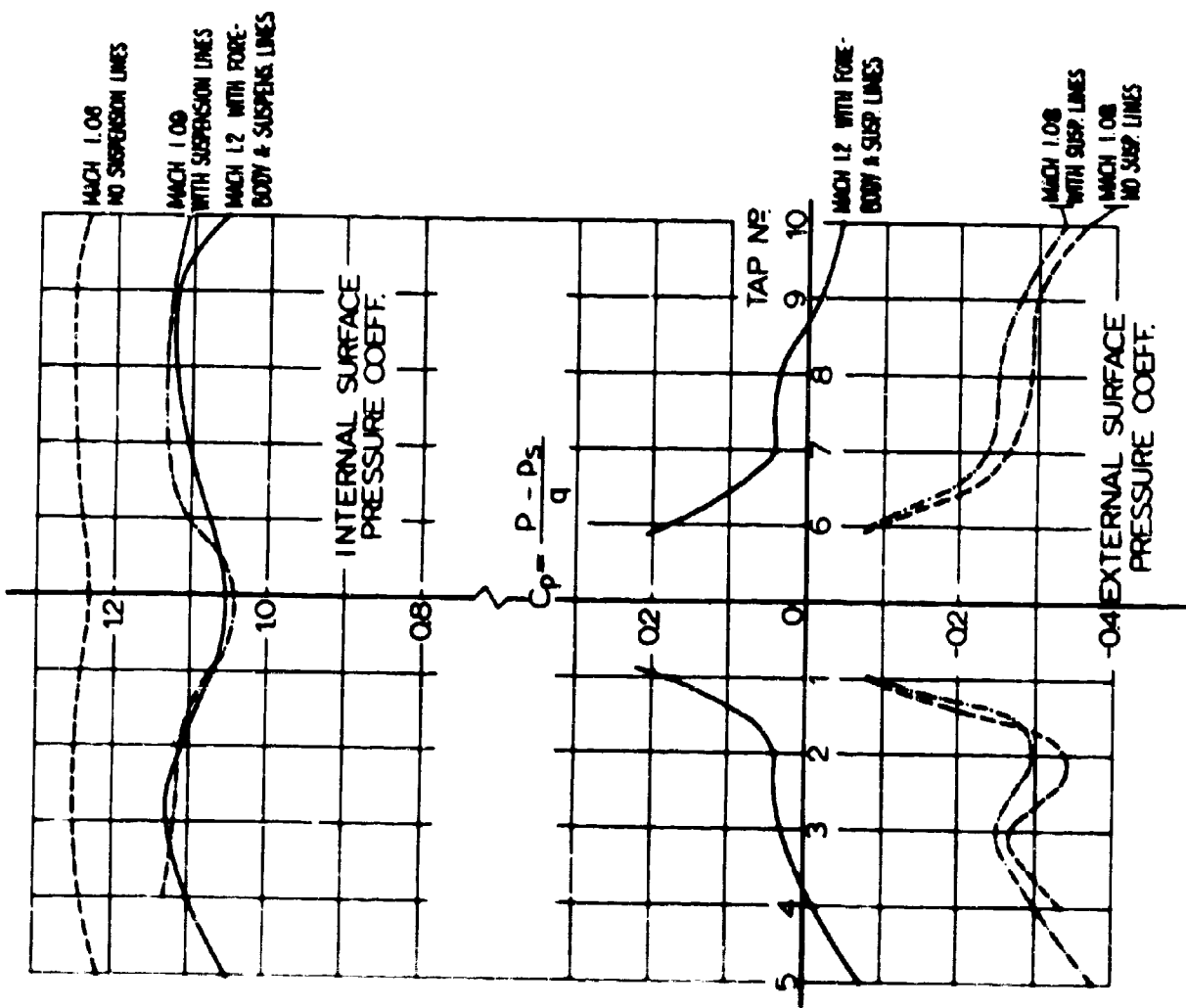


FIG 7-4. PRESSURE COEFFICIENT DISTRIBUTION OF A 26% POROSITY RIBBON PARACHUTE MODEL AT TRANSONIC MACH NUMBERS

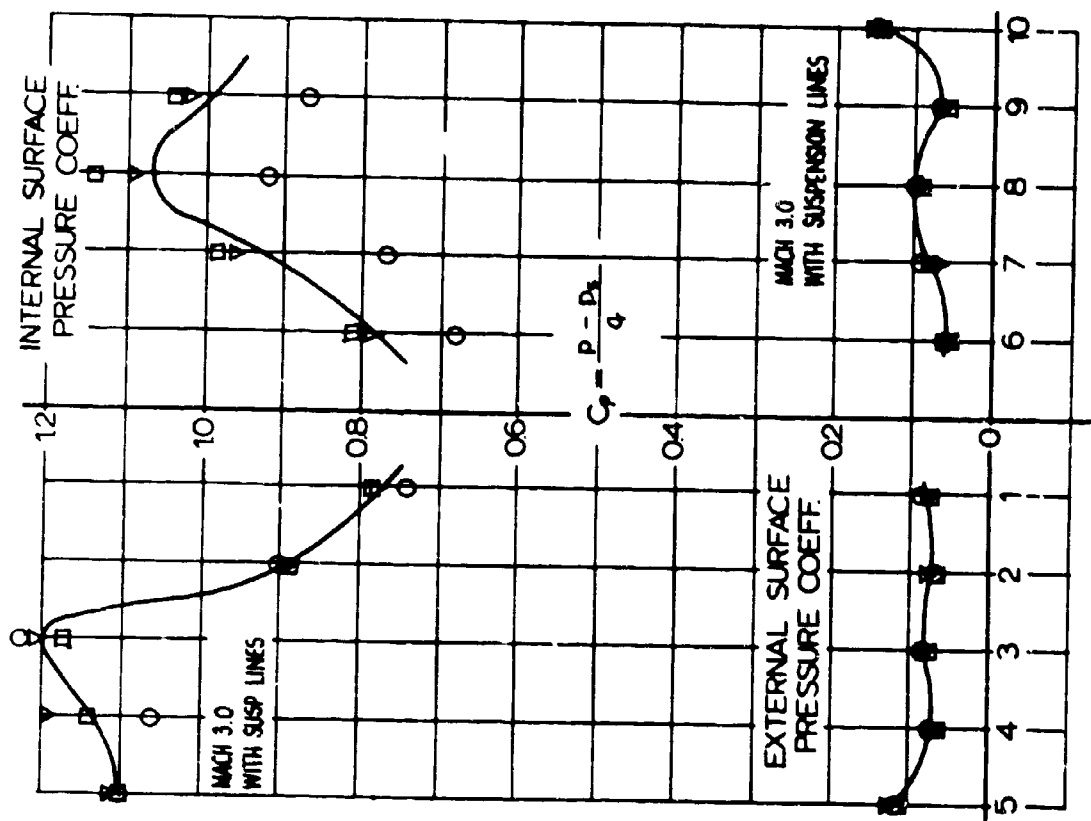


FIG 7-5. PRESSURE COEFFICIENT DISTRIBUTION OF A 26% POROSITY RIBBON PARACHUTE MODEL IN FREE STREAM WITH SUSP. LINES AT MACH 3.0

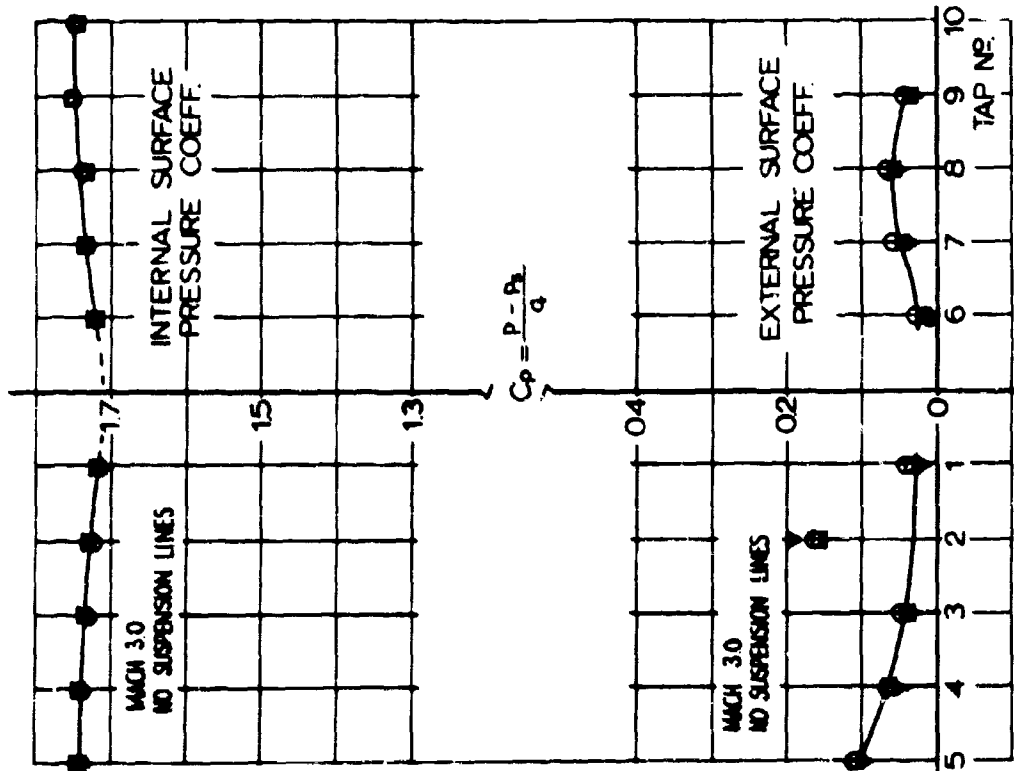


FIG 7-6. PRESSURE COEFFICIENT DISTRIBUTION OF A 26% POROSITY RIBBON PARACHUTE MODEL IN FREE STREAM WITHOUT SUSP. LINES AT MACH 30

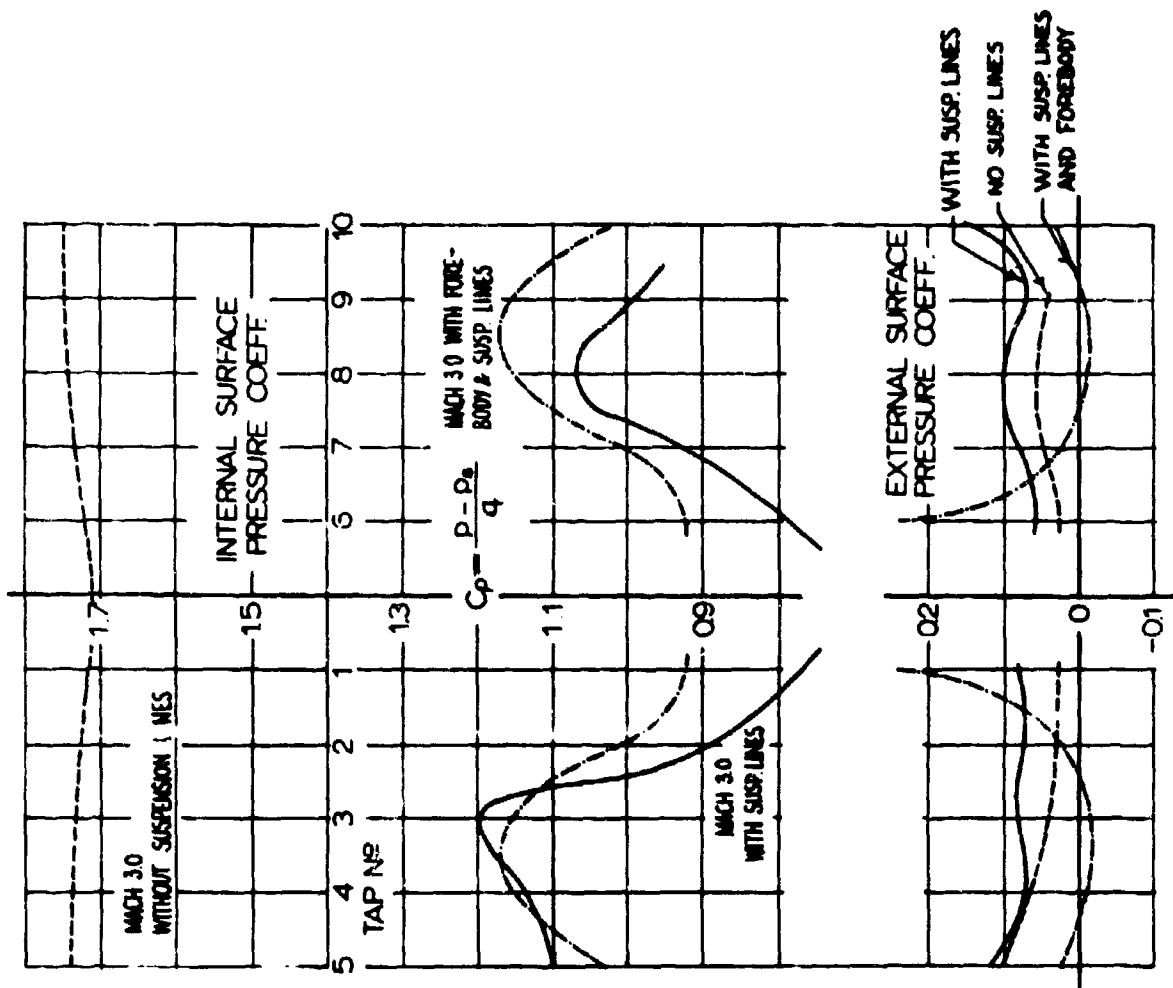


FIG 7-7. PRESSURE COEFFICIENT DISTRIBUTION OF A 26% POROSITY RIBBON PARACHUTE MODEL AT MACH 30



FIG 7-8. DOUBLE EXPOSURE SHADOWGRAPH OF RIBBON PARACHUTE MODEL WITH  
SUSPENSION LINES IN FREESTREAM AT MACH 3.0.

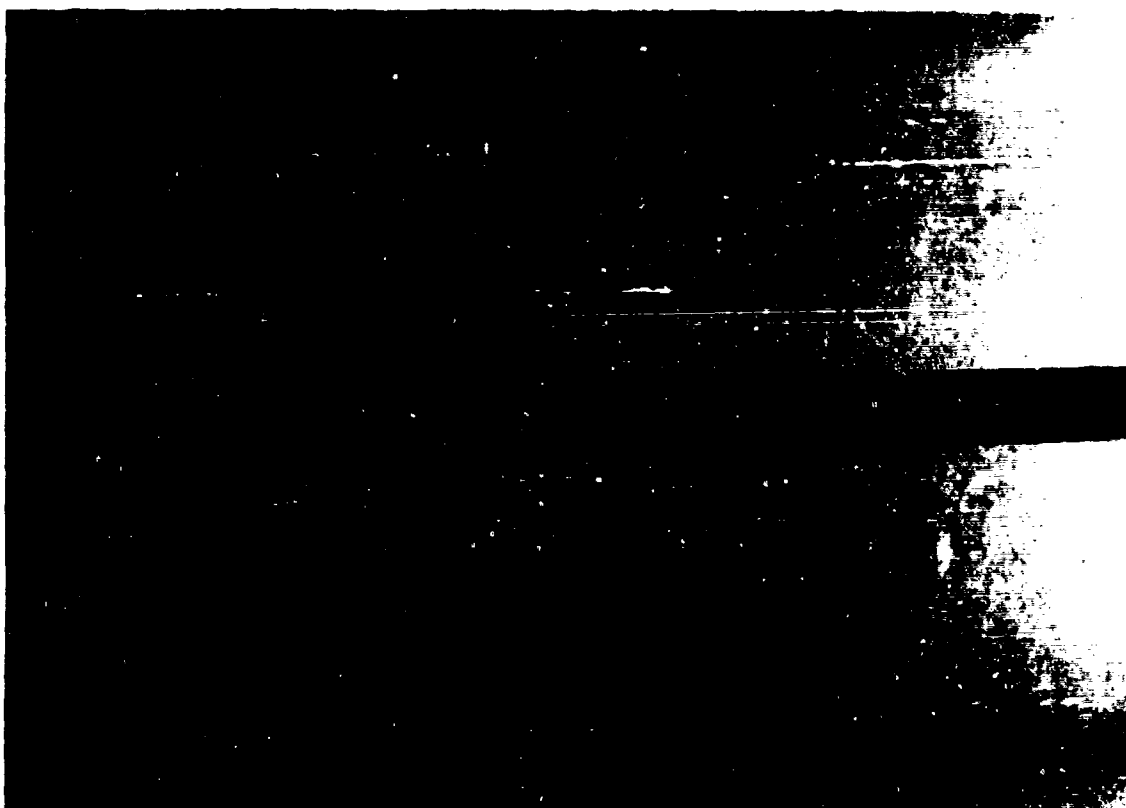


FIG 7-9. DOUBLE EXPOSURE SHADOWGRAPH OF RIBBON PARACHUTE WITHOUT  
SUSPENSION LINES IN FREESTREAM AT MACH 3.0.

AD607976



FIG 7-10. WATER ANALOGY WITH DYE AT  $M_1 = 2.0$  OF A STABLE CONFIGURATION  
BEHIND A FOREBODY AT  $L/D = 4.5$ ;  $H/D_1 = 0.57$ ,  $D_0/D_1 = 0.52$ ,  
 $1/D_1 = 0.35$ .

np605973



FIG 7-11. WATER ANALOGY WITH DYE AT  $M_1 = 2.0$  OF A STABLE CONFIGURATION  
BEHIND A FOREBODY AT  $L/D = 8$ ;  $H/D_1 = 0.57$ ,  $D_0/D_1 = 0.52$ ,  
 $1/D_1 = 0.35$ .



FIG 7-12. WATER ANALOGY WITH DYE AT  $M_1 = 2.0$  OF A STABLE CONFIGURATION;  
 $H/D_1 = 0.57$ ,  $D_0/D_1 = 0.52$ ,  $1/D_1 = 0.35$ .

7-11-58

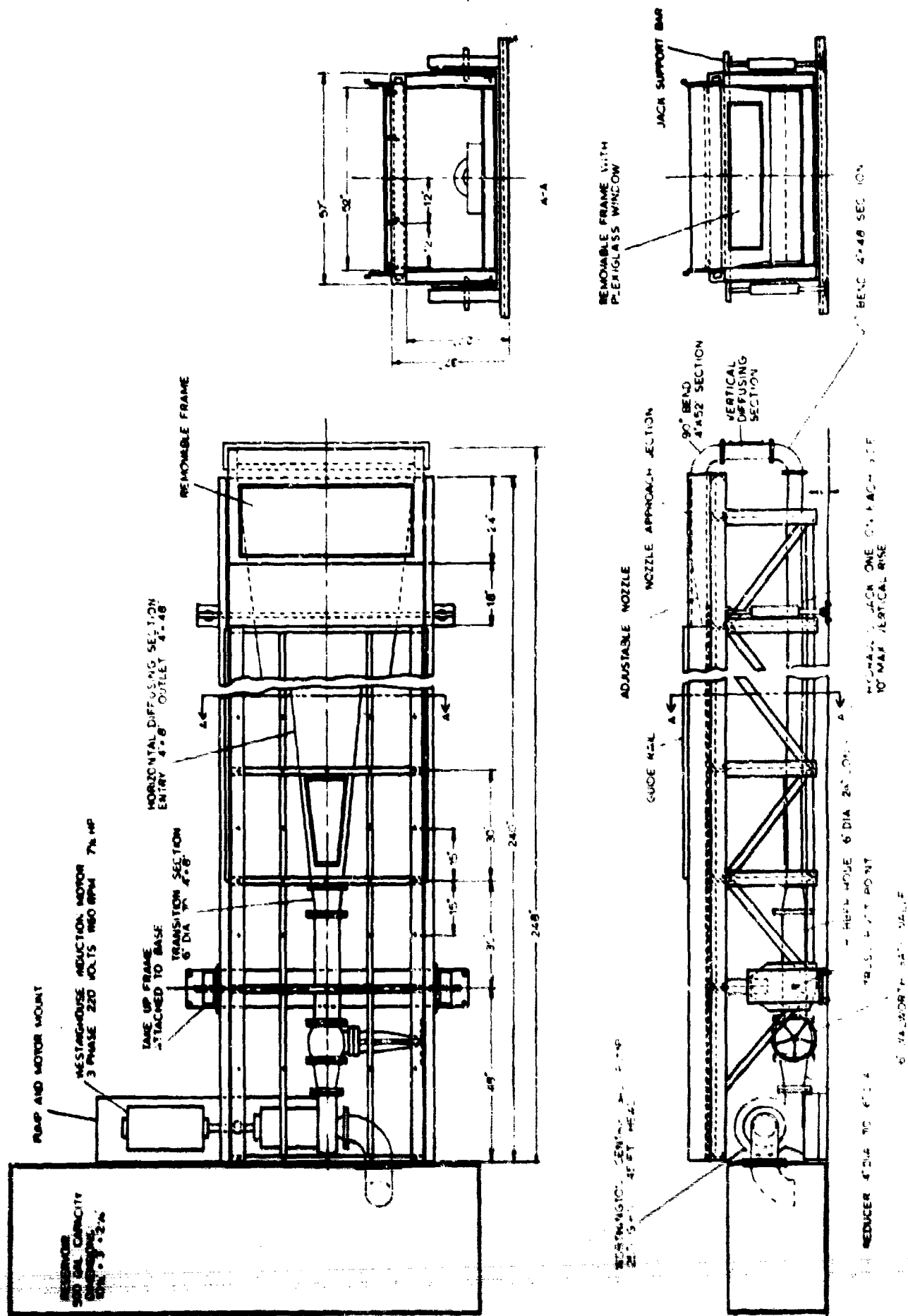


FIG 7-13. FLOW CHANNEL. GENERAL. ASSEMBLY

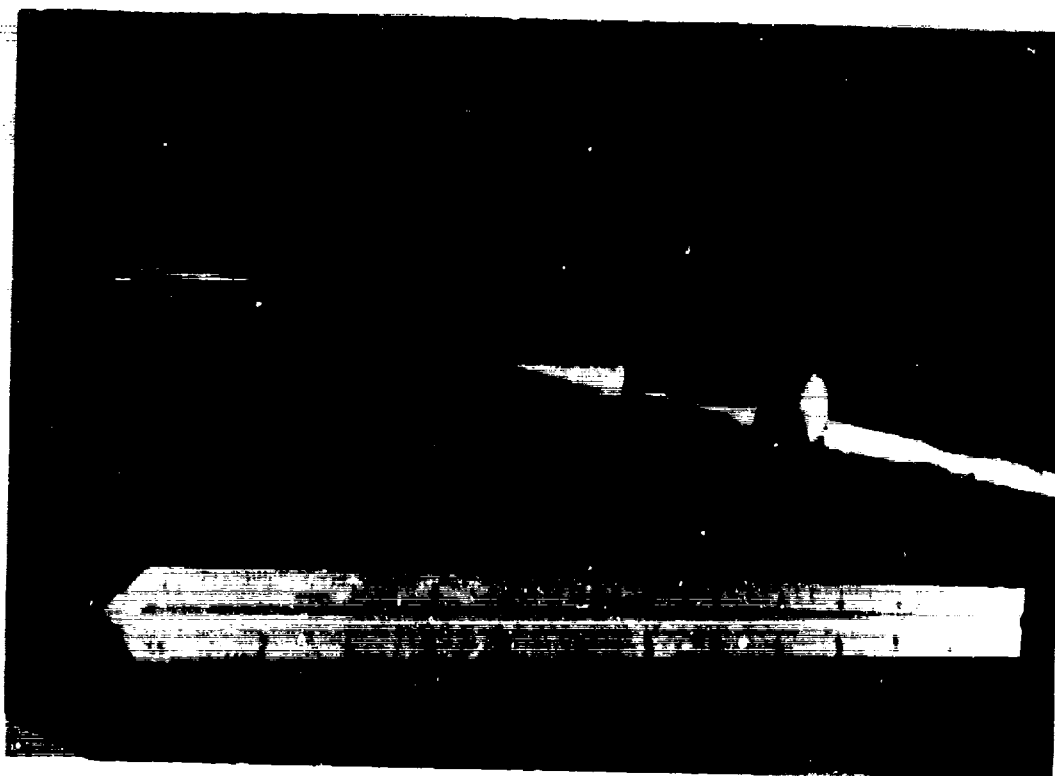


FIG 7-14. SPIKED PARACHUTE MODEL WITH SUSPENSION LINES;  $\Theta = 34^\circ$   
 $H/D_1 = 0.681$ ,  $D_o/D_1 = 0.898$ ,  $1/D_1 = 0.35$ .

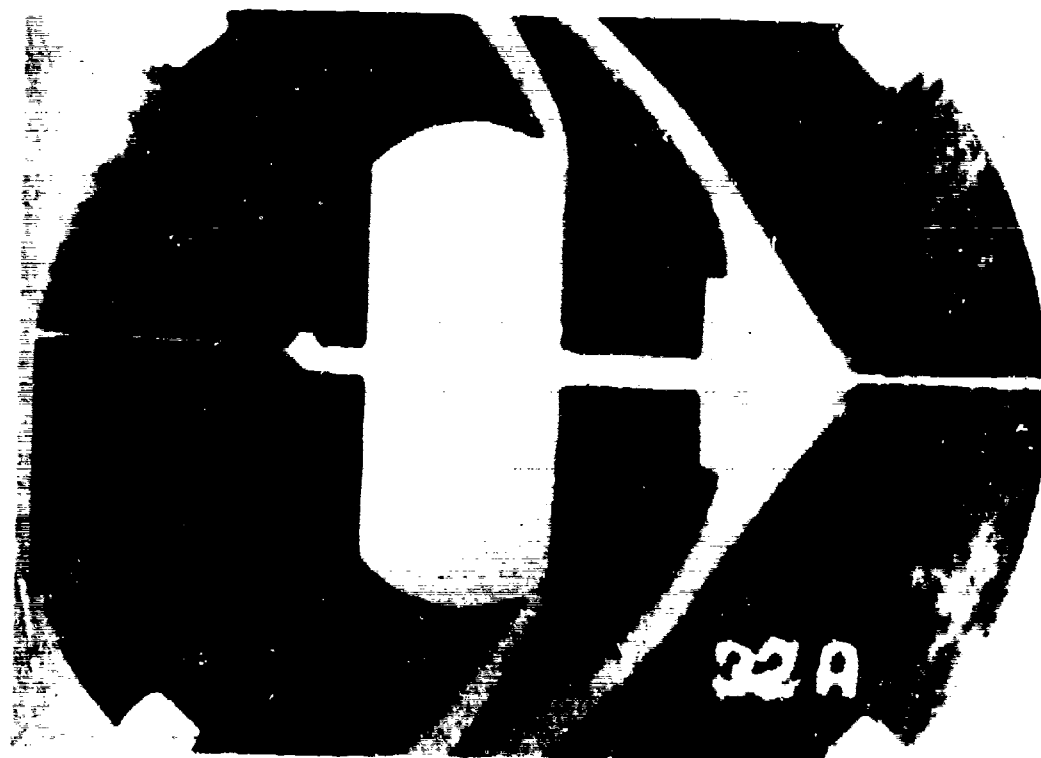


FIG 7-15. STABLE CONFIGURATION IN PENDULUM TESTS AT  $M_1 = 2.00$ ;  
 $\Theta = 34^\circ$ ,  $H/D_1 = 0.681$ ,  $D_o/D_1 = 0.898$ ,  $1/L_1 = 0.35$ .

ADAC-978



FIG 7-16. STABLE CONFIGURATION IN PENDULUM TESTS AT  $M_1 = 2.00$ ;

$\Theta = 34^\circ$ ,  $H/D_1 = 0.421$ ,  $D_0/D_1 = 0.898$ ,  $1/D_1 = 0.35$ .

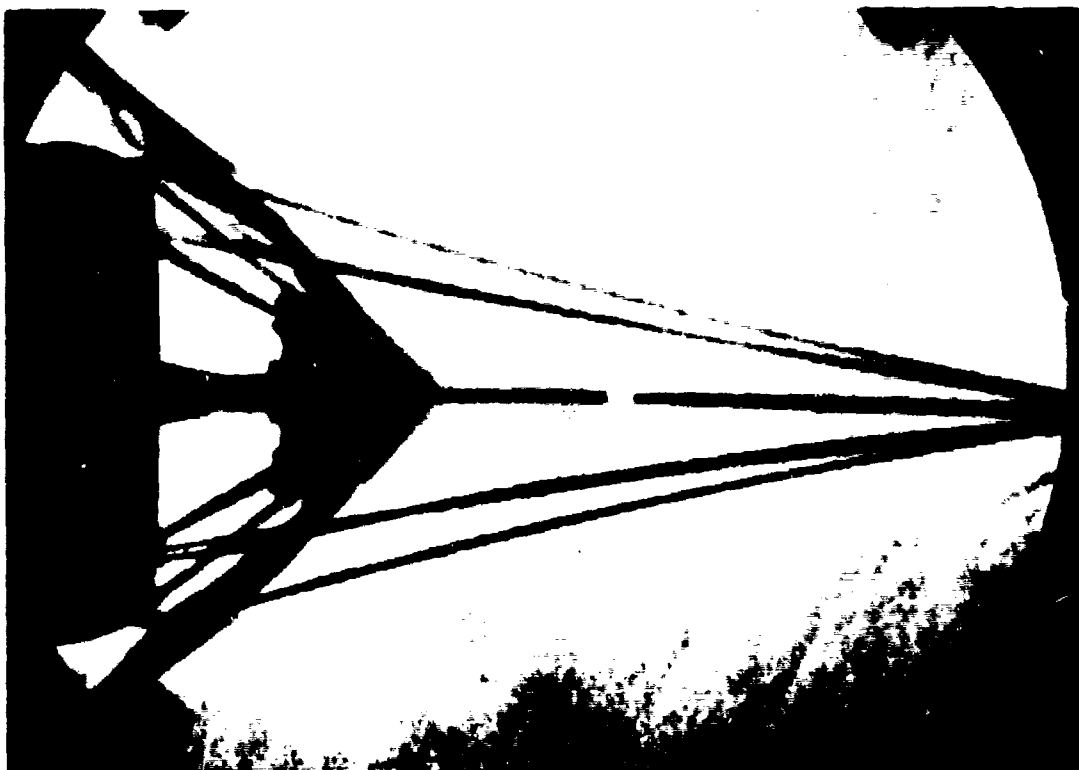


FIG 7-17. STABLE CONFIGURATION WITH SUSPENSION LINES AT  $M_1 = 3.0$ ;

$\Theta = 34^\circ$ ,  $H/D_1 = 0.681$ ,  $D_0/D_1 = 0.898$ ,  $1/D_1 = 0.35$ .

0260773



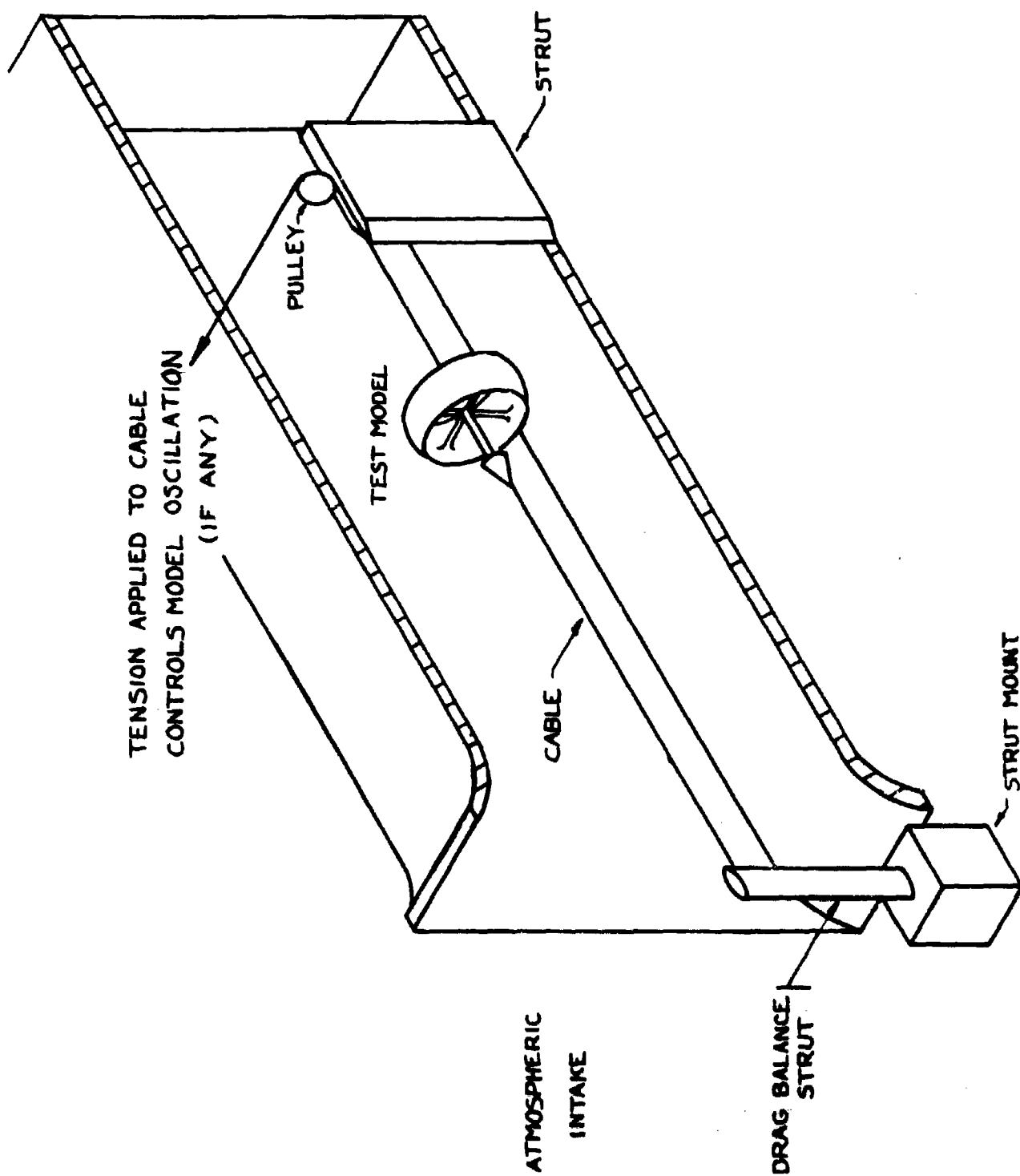


FIG 7-18. CUTAWAY OF WIND TUNNEL ILLUSTRATING TEST ARRANGEMENT FOR DRAG STUDIES AT MACH 1.14

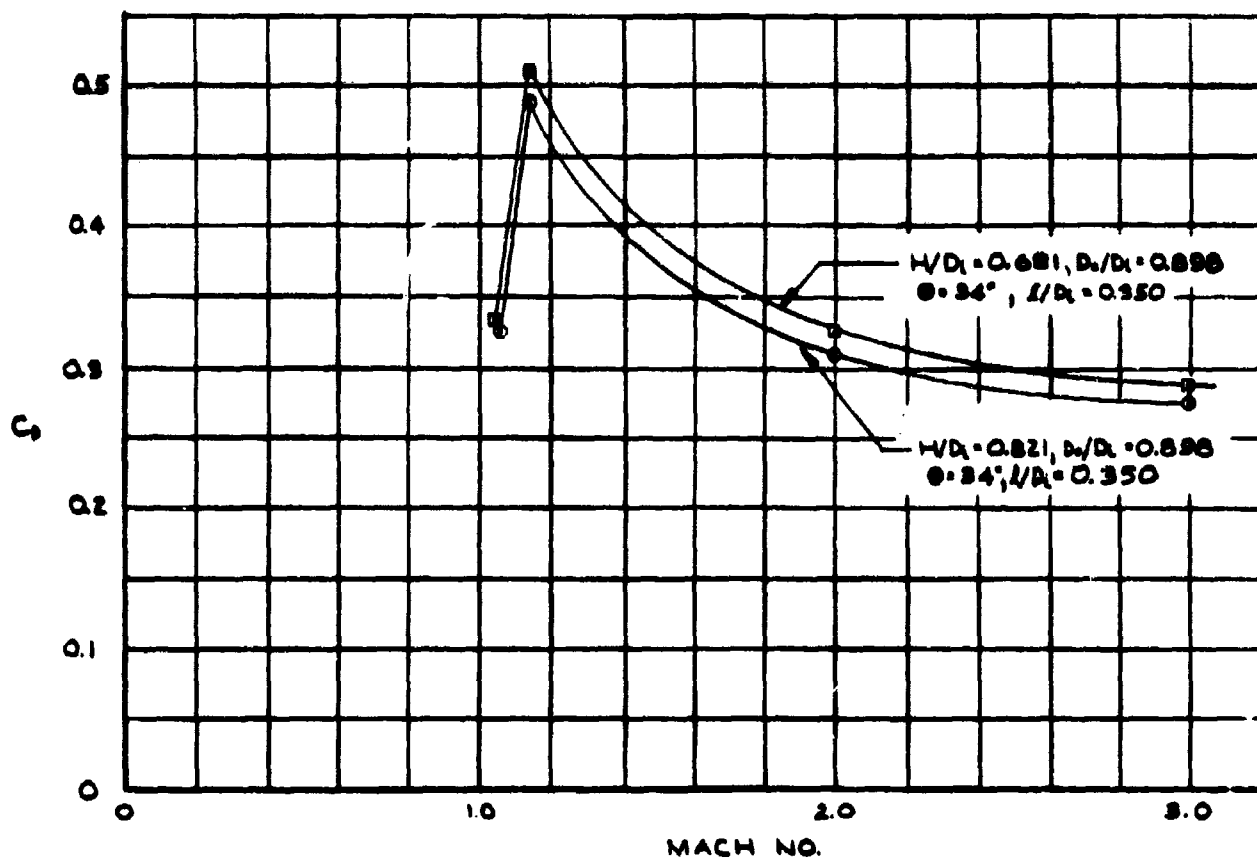


FIG 7-19. DRAG COEFFICIENT OF TWO STABLE CONFIGURATIONS VS. MACH NUMBERS (BASED ON CANOPY SURFACE AREA)

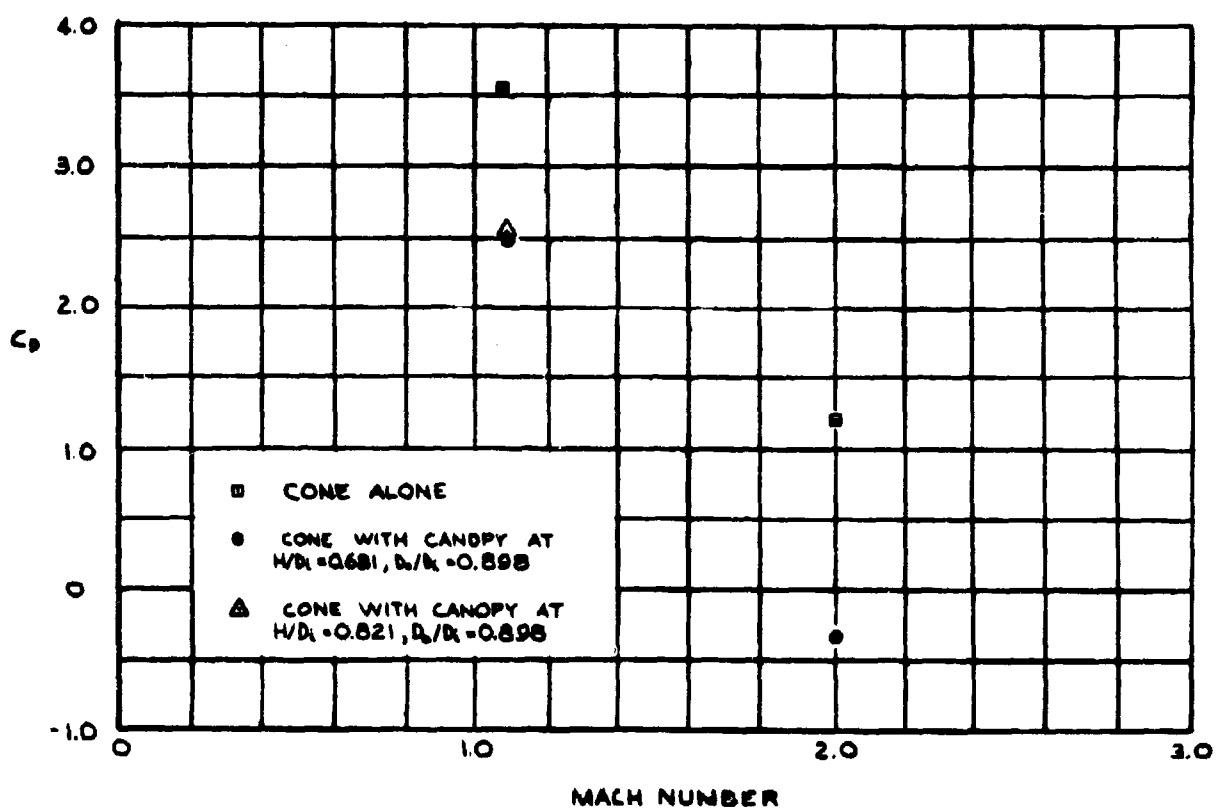


FIG 7-20. DRAG COEFFICIENT OF CONE,  $\theta = 20^\circ$ , VS. MACH NUMBER (BASED ON CONE PROJECTED AREA)

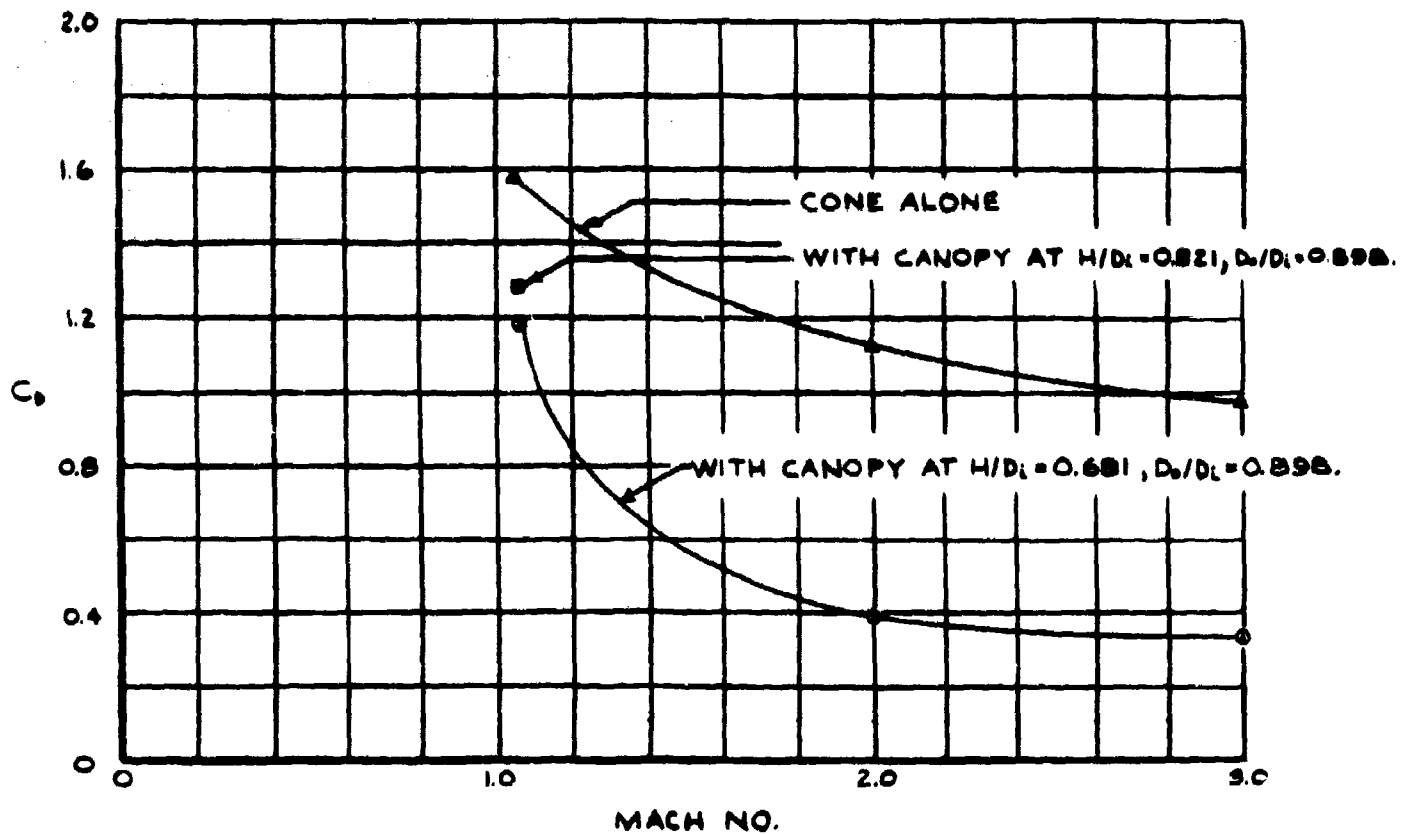


FIG 7-21. DRAG COEFFICIENT OF CONE,  $\theta = 34^\circ$ , VS. MACH NUMBER  
(BASED ON CONE PROJECTED AREA)

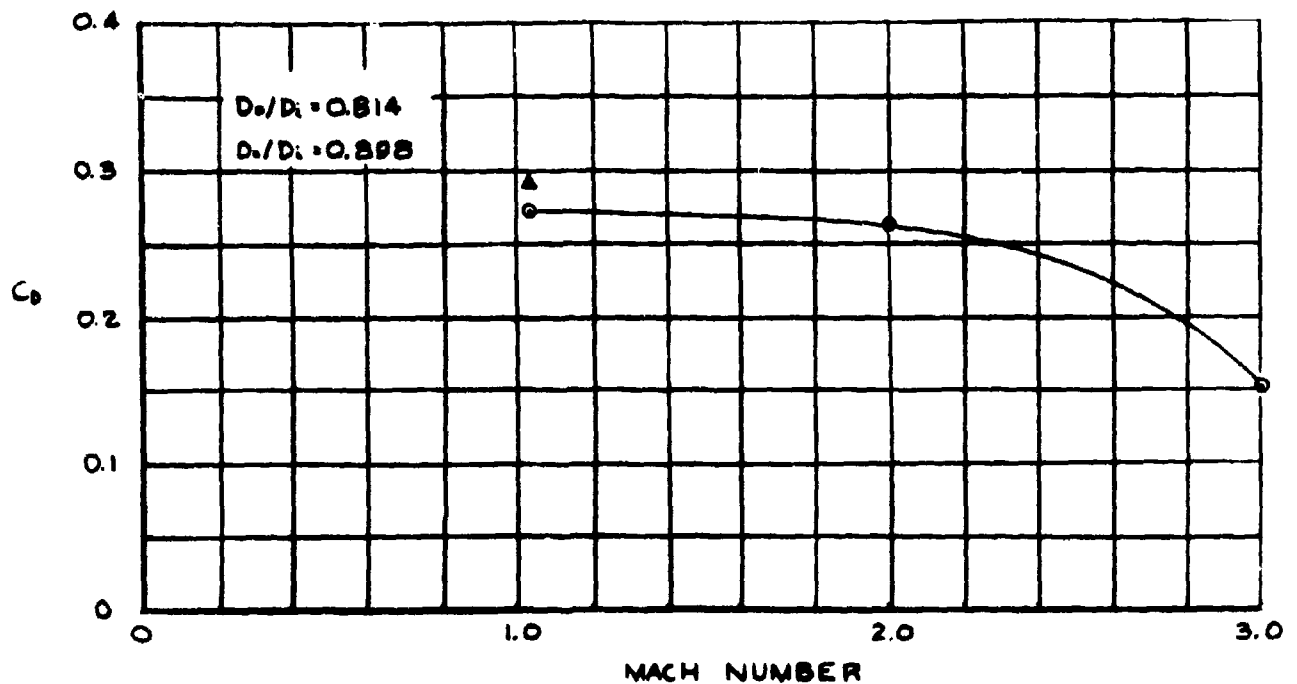


FIG 7-22. DRAG COEFFICIENT OF CANOPY VS. MACH NUMBER  
(BASED ON SURFACE AREA)

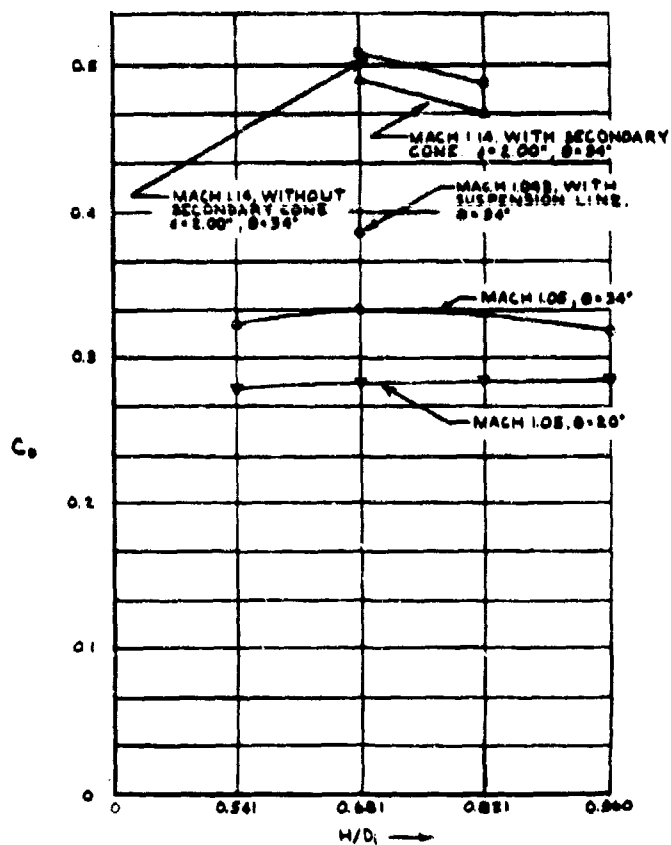


FIG 7-23. DRAG COEFFICIENT VS. CONE LOCATION OF CONFIGURATIONS STUDIED AT TRANSONIC SPEEDS. CONE LENGTH = 1.25",  $D_1/D_2 = 0.898$ . (BASED ON CANOPY SURFACE AREA)

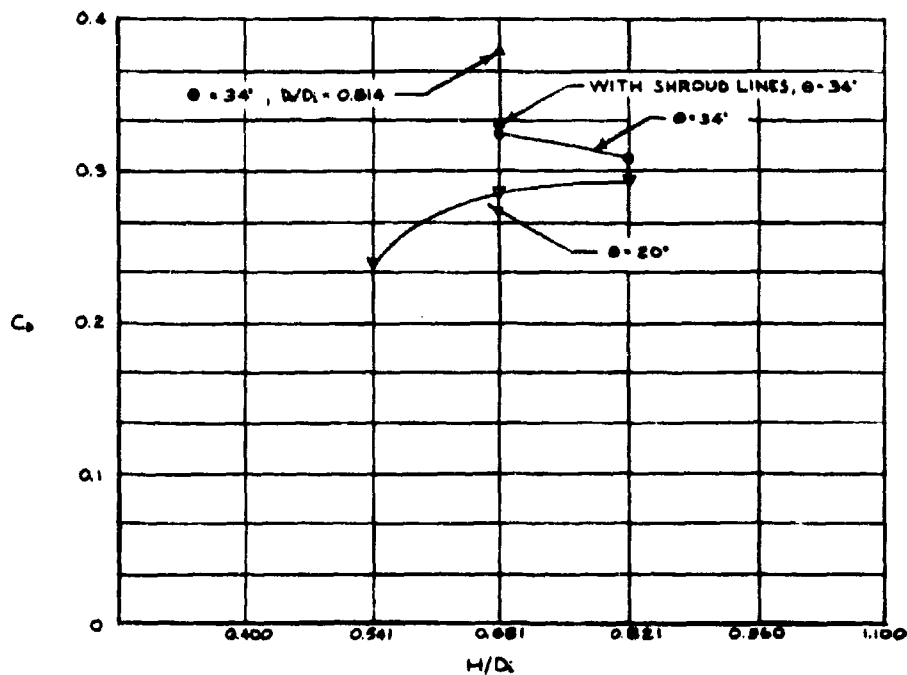


FIG 7-24. DRAG COEFFICIENT VS. CONE LOCATION OF CONFIGURATIONS STUDIED AT MACH 2.0. CONE LENGTH = 1.25",  $D_1/D_2 = 0.898$ . (BASED ON CANOPY SURFACE AREA)

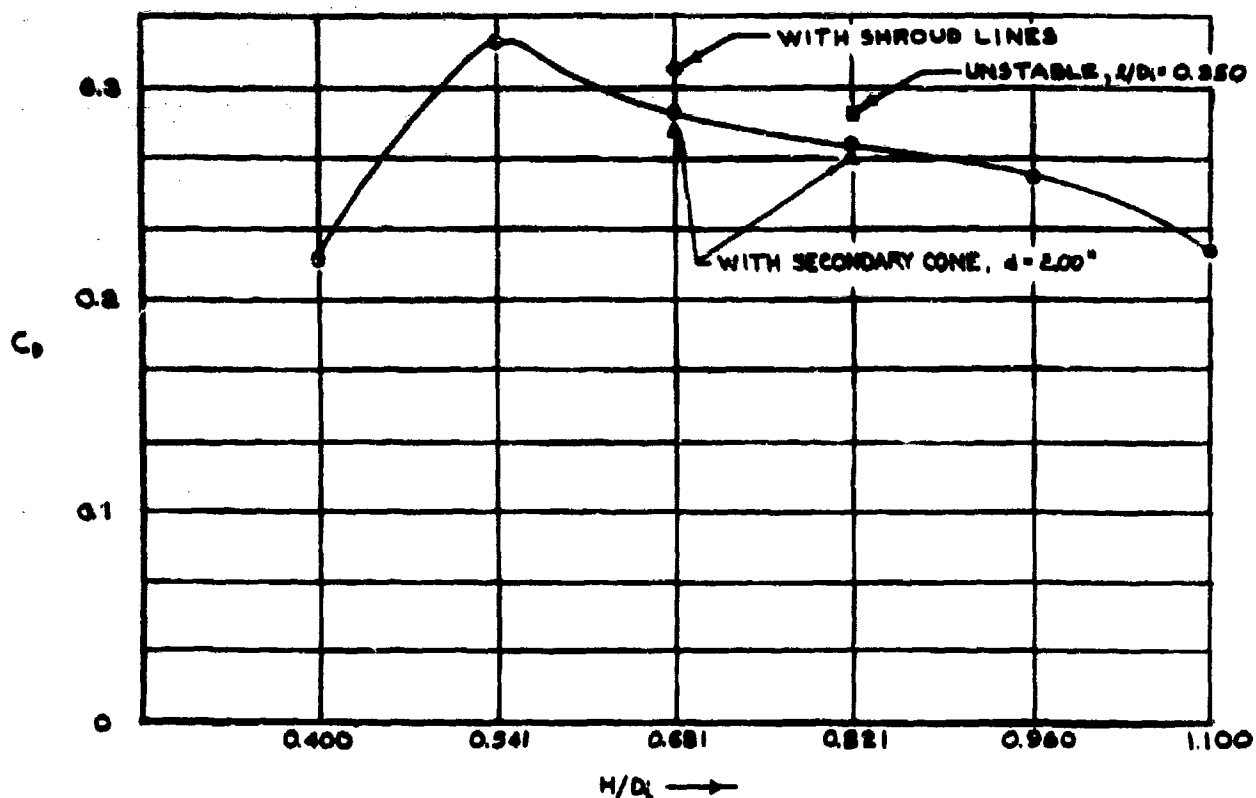


FIG 7-25. DRAG COEFFICIENT VS. CONE LOCATION OF CONFIGURATIONS STUDIED AT MACH 3.0. CONE HALF ANGLE =  $34^\circ$ , CONE LENGTH = 1.25",  $D_o/D_i = 0.898$ . (BASED ON CANOPY SURFACE AREA)

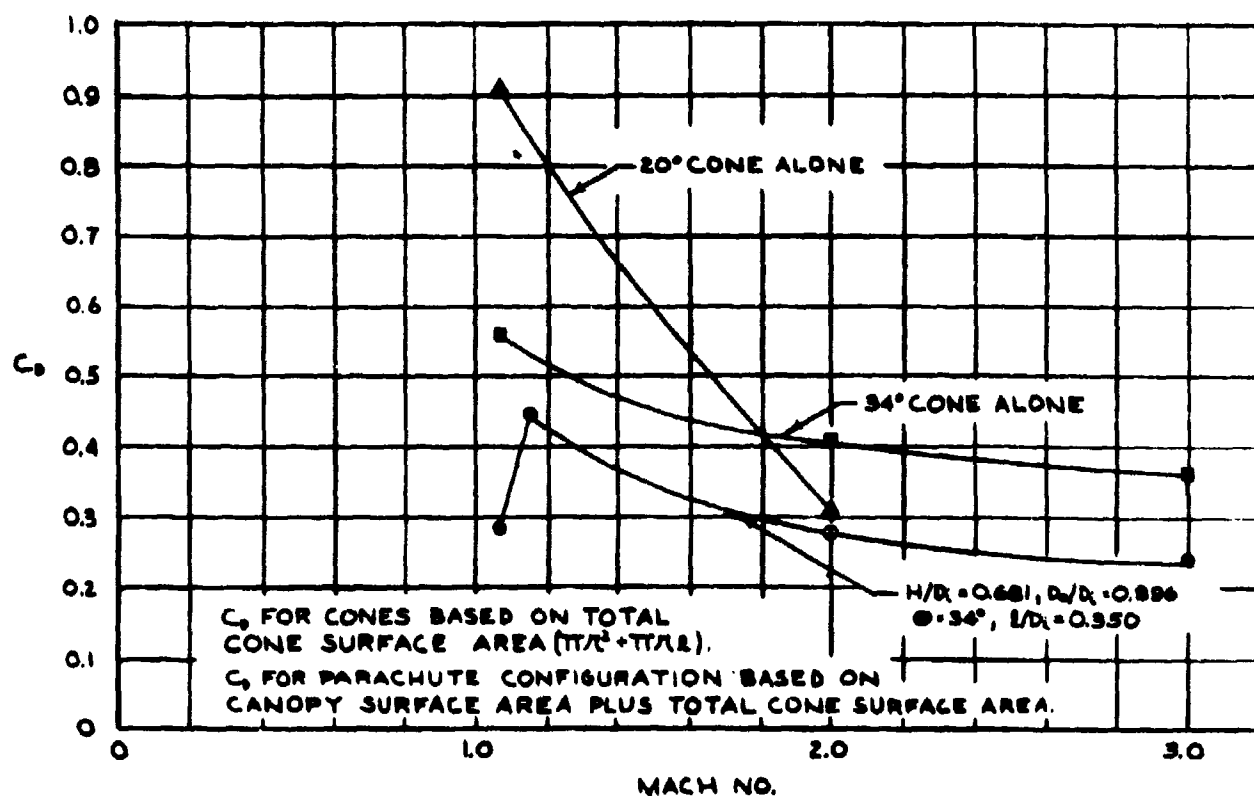


FIG 7-26. DRAG COEFFICIENT BASED ON TOTAL SURFACE AREA VS. MACH NUMBER FOR SEVERAL CONES AND CONFIGURATIONS

## Project No 8

### 6.0 Theoretical Analysis of the Dynamics of the Opening Parachute

#### 6.1 Introduction

6.1.1 In Progress Report No 12, an analytical method was submitted by which the filling time of a circular flat parachute could be calculated. In Progress Report No 14, an analytical method was given for determining the opening forces when the filling time is known. Both of these analytical methods were based on the assumptions that the drag area,  $C_D S$ , of an inflating canopy increases linearly with time, and that the drag coefficient,  $C_D$ , remains constant during the inflation process, implying a linear increase of projected canopy area with time.

6.1.2 Studies which were made to check the validity of these assumptions were described in Progress Report No 14. These experiments showed that the assumption of constant  $C_D$  was nearly correct. However, the experimental size-force studies showed that the projected area varies more nearly parabolically than linearly with time. Therefore, the analytical methods for calculating filling time and opening forces have been revised using the assumption of parabolic variation of drag area with time. These new analytical methods, which include improvements in the method of converting launching velocity to velocity at the beginning of inflation as reported in Progress Report No 15, are presented in this report.

6.1.3 In Progress Report No 15, revisions in the experimental test setup for studying the size-force history of the inflating parachute were reported.

A new suspended mass system was described, and problems concerning the magnitude of the suspended mass were outlined. During this reporting period, a series of wind tunnel tests were made in order to study the relationship between suspended mass and opening force. These studies are reported in Sec 6.4.

6.1.4 Another series of wind tunnel experiments were conducted to measure the pressure distribution over the outer surface of the inflating parachute canopy. The models representing various stages of the inflating parachute were described in Progress Report No 15, Sec 7.4.1. The data from these experiments is currently being reduced, and results will be reported in the next progress report.

## 6.2 Analytical Investigation of Parachute Inflation Time

### 6.2.1 Introduction

6.2.1.1 When a parachute is deployed downstream of a body, it is in a deflated elongated shape, and the net gain of the air flowing in and out of the parachute alters the shape of the canopy until a final shape of inflation is reached. During this process of inflation a retarding force acts upon the load connected to the parachute, and the magnitude of this force is a function of the duration of the inflation, usually called opening time. Therefore, the determination of the opening time is a very important matter.

6.2.1.2 Approximations have been made of the filling time from movies, but these are dependent on definite restrictive conditions such as canopy loading,

equilibrium velocity, etc (Ref 1, p 4-2-3). These methods are in general unsatisfactory.

6.2.1.3 Analytical methods for determining the filling time of a parachute have been attempted in which simplified shapes were assumed for the inflating canopy to reduce the complexity of the problem (Ref 2). However, these methods are still too complicated for practical use. The purpose of this study is to attempt a solution for the filling time under assumptions concerning the inflating canopy shape which are still restrictive, yet lead to a simpler treatment of the problem.

6.2.1.4 Because of the complex physical process involved, and in spite of simplifying assumptions, the analytical expression obtained for filling time is a complicated integral equation which cannot be integrated directly. However, it is possible to perform a numerical integration for any particular case.

#### 6.2.2 List of Symbols

- a = Speed of sound (ft/sec)
- A = Dimensionless constant =  $10 W / g \rho D_0^3$
- E = Constant =  $3(C_{DS})_{max} t_f / D_0^3$  (sec/ft)
- c = Effective porosity  $u/v$
- $C_D$  = Drag coefficient of parachute
- $C_{DS}$  = Drag area of inflating parachute canopy (ft<sup>2</sup>)
- d = Diameter of canopy mouth
- D = Projected diameter of canopy during inflation (ft)



$D_0$  = Nominal diameter of parachute canopy (ft)  
 $g$  = Acceleration due to Earth's gravity (ft/sec<sup>2</sup>)  
 $K'$  = Apparent mass coefficient  
 $L_s$  = Length of suspension lines (ft)  
 $m_i$  = Included mass (slugs)  
 $m_a$  = Apparent mass (slugs)  
 $M$  = Mach number  
 $p$  = Atmospheric pressure (lb/ft<sup>2</sup>)  
 $p_t$  = Total pressure (lb/ft<sup>2</sup>)  
 $P$  = The instantaneous opening force (lbs)  
 $S$  = Projected area of canopy during inflation (ft<sup>2</sup>)  
 $t_f$  = Filling time (sec)  
 $T$  =  $t/t_f$ , ratio of instantaneous time to filling time  
 $u$  = Velocity of flow through canopy roof (ft/sec)  
 $v$  = Velocity during inflation (ft/sec)  
 $v_{in}$  = Velocity of flow through canopy mouth (ft/sec)  
 $v_0$  = Velocity at the beginning of inflation (ft/sec)  
 $V$  = Canopy volume during inflation (ft<sup>3</sup>)  
 $W$  = Weight of suspended load (lbs)  
 $\rho$  = Air density (slugs/ft<sup>3</sup>)  
 $\sigma$  = Standard Atmosphere density ratio  
 $\alpha$  = Ratio of the length of suspension lines,  $L_s$ , to nominal diameter of the canopy,  $D_0$ .

### 6.2.3 Determination of Basic Working Equation for Filling Time

#### 6.2.3.1 Associated with a parachute moving through air is a drag force

based on the shape of the canopy. This drag force is usually expressed in a form similar to other aerodynamic forces, and is the product of the dynamic pressure of the fluid ( $\frac{1}{2} \rho v^2$ ) and the so-called "drag area" of the parachute ( $C_D S$ ).

6.2.3.2 The primary assumption to be made in this investigation is that the drag area of the inflating canopy increases parabolically with time and that the total filling time is also a consequence of this relationship. Also, it will be assumed that the drag coefficient,  $C_D$ , remains constant for the various shapes that the canopy assumes during the inflation process. Both the above assumptions have been verified experimentally and found reasonably accurate.

6.2.3.3 With the assumption that the drag area increases parabolically with time while the drag coefficient remains constant, a parabolic increase of projected area with time is obtained. Thus, the projected area  $S$  can be expressed as

$$S = \frac{\pi D^2}{4} = K t^2. \quad (8.1)$$

The proportionality constant  $K$  is found from the condition

$$D = D_{\max} \quad \text{when } t = t_f,$$

which gives

$$K = \frac{\pi D_{\max}^2}{4 t_f^2}. \quad (8.2)$$

Considering only circular flat parachutes with nominal diameters,  $D_0$ , and considering the fully inflated canopy to be hemispherical (Fig 8-1),  $D_{\max}$

can be expressed by

$$D_{max} = \frac{2 D_0}{\pi} \quad (8.3)$$

With this relationship, equation (8.2) becomes

$$K = \frac{D_0^2}{\pi t_f^2} \quad (8.4)$$

Substituting this expression for K into equation (8.1) gives

$$S = \frac{D_0^2}{\pi} T^2 \quad (8.5)$$

or

$$D = \frac{2 D_0}{\pi} T \quad (8.6)$$

where

$$T = \frac{t}{t_f} \quad .$$

6.2.3.4 The parachute shape during inflation is assumed to consist of a hemisphere of diameter D and a truncated cone with lower base of diameter D and upper base of diameter d, as shown in Fig 8-2 (Ref 7). This assumption is not exactly correct, since the conical and spherical surfaces should actually join tangentially, which would make the spherical portion slightly more than a hemisphere. This slight difference is neglected. Then, by similarity,

$$\frac{d}{L_s} = \frac{D}{L_s + \frac{D^2}{2} - \frac{\pi D}{4}} \quad (8.7)$$

Substituting the value of  $D$  from equation (8.6) in equation (8.7) gives the value of the instantaneous mouth diameter  $d$  as

$$d = \frac{2D_0}{\pi} \left[ \frac{2L_0 T}{2L_0 + D_0 - D_0 T} \right] . \quad (8.8)$$

6.2.3.5 Parachute canopies are normally constructed of porous fabrics which allow a certain portion of the air inflow to permeate the canopy roof. It is the difference between the mass flow entering the canopy mouth and the mass flow through the canopy roof that causes the canopy to inflate. This may be expressed mathematically as

$$\frac{\pi d^2}{4} v_{in} \rho - \frac{\pi D^2}{2} u \rho = \frac{d}{dt} (\rho V) . \quad (8.9)$$

Since the inflation of the parachute requires little time, changes in altitude are negligible, and it can be assumed that the air density remains constant.

6.2.3.6 It is necessary to express the inflow and outflow velocities,  $v_{in}$  and  $u$ , as functions of the velocity of the system,  $v$ . At the beginning of the inflation process, the inflow velocity is nearly equal in magnitude to the free stream velocity, whereas after complete inflation a stagnation point is formed and the inflow velocity is negligible. As an approximation, it is assumed that the inflow velocity decreases linearly with time, which gives

$$\frac{v_{in}}{V} = 1 - T . \quad (8.10)$$

The flow velocity through the canopy roof is then assumed to be proportional to the inflow velocity. This gives

$$u = c V_{in} , \quad (8.11)$$

where  $c$  is the "effective porosity" of the fabric, defined as the ratio of the outflow velocity to the inflow velocity of the flow through a porous fabric (Ref 5). Thus, for equation (8.11) to hold, the flow velocity just inside the canopy roof must be equal to the inflow velocity through the mouth.

6.2.3.7 Now by substituting equations (8.6), (8.8), (8.10) and (8.11) into equation (8.9) and dividing by  $\phi$ , one obtains

$$\frac{dV}{dt} = \frac{D_s^2 v (1-T) T^2}{\pi} \left[ \left( \frac{2L_s}{2L_s + D_s - D_s T} \right) - 2c \right] . \quad (8.12)$$

By making the substitution

$$dt = t_f dT ,$$

equation (8.12) becomes

$$\frac{dV}{dT} = \frac{D_s^2 v t_f (1-T) T^2}{\pi} \left[ \left( \frac{2L_s}{2L_s + D_s - D_s T} \right) - 2c \right] . \quad (8.13)$$

Equation (8.13) represents the basic working equation for finding the filling time,  $t_f$ . By expressing  $v$  as a function of  $T$  and integrating the right side from  $T = 0$  to  $T = 1$ , and the left side from  $V = 0$  to  $V = V_{\max}$ , a solution for the filling time can be obtained.

#### 6.2.4 The Infinite Mass Case

There are two important cases to be considered when investigating the velocity of the system during inflation of the parachute. The first is called the "infinite mass" case, where the velocity of the system does not change appreciably during inflation and can therefore be considered constant (Ref 1).

To solve for the filling time in the infinite mass case, equation (8.13) can be directly integrated with  $v$  constant and equal to  $v_0$ , the velocity at the beginning of inflation. Putting equation (8.13) in integral form, one obtains

$$\frac{D_0^2 v_0 t_f}{\pi} \int_0^1 T^2 (1-T) \left[ \left( \frac{2L_s}{2L_s + D_0 - D_0 T} \right)^2 - 2c \right] dT = \int_0^{V_{\max}} dV. \quad (8.14)$$

Integrating Equation (8.14) gives

$$V_{\max} = \frac{D_0^2 v_0 t_f}{\pi} \left[ \frac{8L_s^2(2L_s + D_0)}{D_0^3} \ln \frac{2L_s}{2L_s + D_0} - \frac{12L_s^2(2L_s + D_0)^2}{D_0^4} \ln \frac{2L_s}{2L_s + D_0} + \right. \\ \left. + \frac{2L_s(4L_s + D_0)}{D_0^2} - \frac{2L_s(12L_s^2 + 9L_s D_0 + D_0^2)}{D_0^3} - \frac{c}{6} \right]. \quad (8.15)$$

But  $V_{\max}$  can be expressed as

$$V_{\max} = \frac{2D_0^3}{3\pi^2}. \quad (8.16)$$

Substituting equation (8.16) in equation (8.15), the value of  $t_f$  can be obtained as

$$t_f = 2D_0 / 3\pi v_0 \left[ \frac{8L_s^2(2L_s + D_0)}{D_0^3} \ln \frac{2L_s}{2L_s + D_0} - \frac{12L_s^2(2L_s + D_0)^2}{D_0^4} \ln \frac{2L_s}{2L_s + D_0} + \right. \\ \left. + \frac{2L_s(4L_s + D_0)}{D_0^2} - \frac{2L_s(12L_s^2 + 9L_s D_0 + D_0^2)}{D_0^3} - \frac{c}{6} \right] \quad (8.17)$$

Equation (8.17) gives a relation for finding the filling time for the infinite mass case. If the length of the suspension lines  $L_s$  is taken equal to the nominal diameter of the canopy  $D_0$ , the value of the filling time  $t_f$  for the infinite mass case can be simplified to

$$t_f = \frac{2D_0}{3\pi v_0 \left( 0.059 - \frac{c}{6} \right)} \quad (8.18)$$

## 6.2.5 The Finite Mass Case

6.2.5.1 The second case to be considered is the "finite mass" case, in which the velocity of the system does change appreciably during the inflation process. This case is much more complicated than the infinite mass case, and Newton's Second Law of Motion must be used in the investigation. Newton's Second Law states that an unbalanced force which acts on a body produces a rate of change in the momentum of the body equal to the unbalanced force. It can be written as

$$\frac{d(mV)}{dt} = F \quad (8.19)$$

In the case of an inflating parachute, the force  $F$  is the aerodynamic drag force,  $F = (\rho/2)C_D S v^2$ , and the mass term  $m$  includes the mass of the suspended load  $W/g$ , the mass of the air trapped in the canopy, called included mass  $m_i$ , and a term called "apparent" mass  $m_a$ , which results from the transfer of energy to the surrounding air of a body moving through the air. The mass of the parachute canopy and suspension lines is neglected. It is necessary to investigate both the included and apparent masses before attempting to determine the velocity during inflation.

6.2.5.2 As mentioned before, the included mass is the mass of the air trapped within the parachute canopy and can be expressed as  $m_i = \rho V$ . An expression for the canopy volume is then necessary. The volume of the canopy is (See Fig 8-2)

$$V = V_{\text{hemisphere}} + V_{\text{frustum}} \quad (8.20)$$

$$V = \frac{2}{3} \pi \left(\frac{D}{2}\right)^3 + \left[ \frac{\pi}{3} \left(\frac{D}{2}\right)^2 \sqrt{\left(L_s + \frac{D_s}{2} - \frac{\pi D^2}{4}\right) - \frac{D^2}{4}} - \frac{\pi}{3} \left(\frac{d}{2}\right)^2 \sqrt{L_s^2 - \frac{d^2}{4}} \right]$$

Substituting equations (8.6) and (8.8) into equation (8.20) gives

$$V = \frac{2 D_s^3 T^2}{3 \pi} \left\{ \left[ \frac{1}{4} + 2 \left( \frac{L_s}{2 L_s + D_s - D_s T} \right)^3 \right] \sqrt{\left( \frac{2 L_s}{D_s} + 1 - T \right)^2 - \frac{4 T^2}{\pi^2}} + \frac{T}{\pi} \right\} \quad (8.21)$$



Then the included mass  $m_i$  can be expressed as

$$m_i = \frac{2D_0^3 T^2 \rho}{3\pi} \left\{ \left[ \frac{1}{4} + 2 \left( \frac{L_s}{2L_s + D_0 - D_0 T} \right)^3 \right] \sqrt{\left( \frac{2L_s}{D_0} + 1 - T \right)^2 - \frac{4T^2}{\pi^2}} + \frac{T}{\pi} \right\}. \quad (8.22)$$

6.2.5.3 To illustrate the significance of the included mass, Table 8-1 was prepared. This table gives the included mass of various inflated parachutes at sea level density assuming that the length of the suspension lines  $L_s$  is equal to the nominal diameter,  $D_0$ , of the canopy. It shows that for retardation parachutes, the included mass may be an important item and in each particular situation the effect of the included mass should be investigated in order to determine its significance. Since this study is concerned mainly with the general retardation problem, the included mass term will be considered in the analysis.

$D_0$ (ft)	$m_i$ (slugs)	$m_i$ (lb)
20	1.283	41.4
28	3.540	114.0
40	10.270	330.5
60	34.700	1119.0

TABLE 8-1. INCLUDED MASS OF FULLY INFLATED PARACHUTES OF VARIOUS DIAMETERS

6.2.5.4 During the inflation of a parachute canopy, the flow pattern and kinetic energy of the air surrounding the canopy undergo extreme changes due to the unsteadiness of motion and the changing shape of the canopy. This

change of energy results in a force and is related to an increase in mass called the "apparent" mass (Ref 3). For regular solid bodies, such as spheres, in potential flow the apparent mass can be developed exactly. It is possible to express the apparent mass of solid bodies of revolution as

$$m_a = K' \pi R^3 \rho \quad (8.23)$$

where R is the radius of the body and K' is a constant determined by the shape of the body. For a solid sphere,  $K' = 0.666$  and for a solid flat disc,  $K' = 0.849$  (Ref 4).

6.2.5.5 Heinrich (Ref 5) attempted experimentally to determine the apparent mass of fully inflated parachutes of various types made out of porous cloth, and found that a value of  $K' = 0.25$  gave a close approximation. Since theoretical approaches to the problem of apparent mass consider only solid bodies, it appears that the most applicable assumption for the apparent mass of an inflating parachute should be based on this experimental work done with porous fabrics. Therefore, it will be assumed that the apparent mass of the fully inflated parachute has a coefficient of  $K' = 0.25$ , the value provided in Ref 5. This coefficient apparently changes in value during the inflation process, because if the assumption were made that it remained constant, the canopy would have an apparent mass equal to that of a fully inflated parachute with a projected diameter equal to the projected diameter of the inflating canopy. The inflating canopy is more streamlined in shape than an inflated canopy of the same nominal diameter, and therefore its apparent mass will be less. Under these considerations, the approximation is made that the apparent

mass coefficient varies linearly with time during inflation, reaching a maximum value of 0.25 at full inflation. This is apparently the upper limit and shall be expressed as

$$K' = 0.25 T. \quad (8.24)$$

The apparent mass from equation (8.23) can then be expressed as

$$m_a = 0.25 \pi R^3 \rho T. \quad (8.25)$$

With  $R = D/2 = D_0/\pi T$ , equation (8.25) can be written as

$$m_a = \frac{\rho D_0^3}{4 \pi^2} T^4. \quad (8.26)$$

Equation (8.26) gives the value of the apparent mass; from the equation it can be seen that it is not small and hence cannot be neglected.

6.2.5.6 The total mass,  $m$ , which was defined as the sum of the suspended load  $W/g$ , the included mass  $m_1$  and the apparent mass  $m_a$  can now be expressed as

$$m = \frac{W}{g} + m_1 + m_a \quad (8.27)$$

Substituting the values of  $m_1$  and  $m_a$  from equations (8.22) and (8.26), respectively, gives

$$m = \frac{W}{g} + \rho D_0^3 \left[ \frac{2T^2}{3\pi} \left\{ \frac{1}{4} - 2 \left( \frac{L_s}{2L_s + D_0 - D_0 T} \right)^3 \right\} \right. \\ \left. + \sqrt{\left( \frac{2L_s}{D_0} + 1 - T \right)^2 - \frac{4T^2}{\pi^2}} + \frac{T}{\pi} \right] + \frac{T^4}{4\pi^2}. \quad (8.28)$$

In view of the coming integration it is necessary to simplify the above expression. The expression

$$\frac{2T^2}{3\pi} \left\{ \left[ \frac{1}{4} - 2 \left( \frac{L_s}{2L_s + D_0 - D_1 T} \right)^3 \right] \sqrt{\left( \frac{2L_s}{D_0} + 1 - T \right)^2 - \frac{4T^2}{\pi^2}} + \frac{T}{\pi} \right\} + \frac{T^4}{4\pi^2} \quad (8.29)$$

can be simplified by letting

$$\alpha = \frac{L_s}{D_0} \quad (8.30)$$

Then the expression (8.29) can be written as

$$\frac{2T^2}{3\pi} \left\{ \left[ \frac{1}{4} - 2 \left( \frac{\alpha}{2\alpha + 1 - T} \right)^3 \right] \sqrt{(2\alpha + 1 - T)^2 - \frac{4T^2}{\pi^2}} + \frac{T}{\pi} \right\} + \frac{T^4}{4\pi^2} \quad (8.31)$$

6.2.5.7 In general, the value of  $\alpha$  for conventional parachutes is between 0.75 and 1. The numerical values of the expression (8.29) were found for both  $\alpha = 0.75$  and  $\alpha = 1.0$  for values of  $T$  between 0 and 1 in 0.1 intervals. These values are tabulated in Tables 8-2 and 8-3, and plotted in Fig 8-3. It is evident from the figure and tables that the values of  $\alpha$  in the interval 0.75 to 1 does not have any significant effect on the value of the expression (8.29) in the region of interest  $0 < T < 1.0$ . From Fig 8-3 it can be seen that this expression can be approximated closely by the parabola  $T^2/10$ .

6.2.5.8 Using this simplification of the last paragraph, the total mass can be expressed as

$$m = \frac{W}{g} + \frac{\rho D_0^3 T^2}{10} \quad (8.32)$$

Substituting equation (8.32) in Newton's Law [equation (8.19)] gives

$$\frac{d}{dt} \left[ v \left( \frac{W}{g} + \frac{\rho D_o^3 T^2}{10} \right) \right] = -\frac{1}{2} \rho v^3 (C_D S). \quad (8.33)$$

But by the fundamental assumption that drag area varies parabolically with time the instantaneous drag area  $C_D S$  can be expressed as

$$C_D S = (C_D S)_{\max} T^2. \quad (8.34)$$

Substituting equation (8.34) and simplifying equation (8.33) gives

$$(A + T^2) \frac{dv}{dT} + v \frac{d}{dT} (A + T^2) = -BT^2 v^2, \quad (8.35)$$

where

$$A = \frac{10W}{g\rho D_o^3} \quad (8.36)$$

$$B = \frac{5(C_D S)_{\max} t_f}{D_o^3} \quad (8.37)$$

or

$$\frac{1}{v^2} \frac{dv}{dT} + \frac{2T}{(A + T^2)} \frac{1}{v} = -\frac{BT^2}{A + T^2}. \quad (8.38)$$

Defining  $1/v$  as  $x$ , one gets

$$\frac{dx}{dT} - \frac{2T}{A + T^2} x = \frac{BT^2}{A + T^2}, \quad (8.39)$$

Equation (8.39) is an ordinary linear differential equation and can be solved to give

$$x = \frac{B(A + T^2)}{2} \left( \frac{1}{\sqrt{A}} \tan^{-1} \frac{T}{\sqrt{A}} - \frac{T}{A + T^2} \right) + C(A + T^2) \quad (8.40)$$

where C is a constant of integration, or

$$\frac{1}{v} = \frac{B(A+T^2)}{2} \left( \frac{1}{\sqrt{A}} \tan^{-1} \frac{T}{\sqrt{A}} - \frac{T}{A+T^2} \right) + C(A+T^2). \quad (8.41)$$

The constant is evaluated by using the condition that  $v = v_0$  when  $T = 0$ , and finally the value of instantaneous velocity can be expressed as

$$v = \frac{v_0}{\frac{BV_0}{2} \left[ \frac{A+T^2}{\sqrt{A}} \tan^{-1} \frac{T}{\sqrt{A}} - T \right] + \frac{A+T^2}{A}} \quad (8.42)$$

6.2.5.9 Substituting into the basic working equation (8.13) the value of  $v$  given by equation (8.42) and writing the resultant equation in integral form, the following expression is obtained, from which the filling time for the finite mass case can be determined:

$$\int_0^{v_{max}} dv = \int_0^1 \frac{\frac{D_0^2 v_0 (1-T) T^2 t_f}{\pi} \left[ \left( \frac{2L_s}{2L_s + D_0 - D_0 T} \right)^2 - 2c \right]}{\frac{BV_0}{2} \left[ \frac{A+T^2}{\sqrt{A}} \tan^{-1} \frac{T}{\sqrt{A}} - T \right] + \frac{A+T^2}{A}} dT. \quad (8.43)$$

The right hand expression cannot be integrated directly without making serious assumptions and simplifications. Therefore, to determine the filling time accurately, a numerical integration of the expression is necessary. This is further complicated by the fact that the integrand contains  $t_f$ , which necessitates the use of a trial and error solution.

#### 6.2.6 Numerical Solution

Since it is not possible to integrate equation (8.43), the following numerical method can be used to determine the filling time for any given case:

- (1) Calculate the volume of the fully inflated parachute  $V_{\max}$  by assuming it to be a hemisphere

$$V_{\max} = \frac{2 D_p^3}{3\pi^2} .$$

- (2) Calculate the corresponding value of  $c$ , the effective porosity, as outlined in Progress Report No 14, Sec 7.2.1.
- (3) Calculate the velocity at the beginning of inflation  $v_0$  as outlined in Progress Report No 15, Sec 7.2.
- (4) Assume a value of the filling time  $t_f$  which appears to be in the right order and calculate the value of the integrand

$$f(T, t_f) = \frac{\frac{D_p^2 V_0 t_f}{\pi} T^2 (1-T) \left[ \left( \frac{2L_p}{2L_p + D_p - D_p T} \right)^2 - 2c \right]}{\frac{B V_0}{2} \left[ \frac{A+T^2}{\sqrt{A}} \tan^{-1} \frac{T}{\sqrt{A}} - T \right] + \frac{A+T^2}{A}} \quad (8.44)$$

for  $T$  varying from 0 to 1 in intervals of 0.1. These calculations can be made conveniently on a calculation sheet as shown in Fig 8-4.

- (5) Plot the value of the integrand obtained under (4) above versus  $T$ , and measure the area under the curve with the help of a planimeter. This area represents the numerical value of

the right hand side of equation (8.43). If this value is equal or approximately equal to the volume of the parachute canopy calculated under (1) above, the assumed filling time represents a satisfactory approximation of the filling time.

- (6) If the process under (5) does not show satisfactory agreement, take several values of  $t_f$  and repeat operations (4) and (5).
- (7) Compare again and if no satisfaction is reached, plot a curve showing the measured areas obtained in the preceding operations versus the assumed values of the filling time, and from this find the particular value of  $t_f$  for which the value of the curve equals the volume of the canopy. This value gives the calculated value of filling time.

### 6.3 Analytical Investigation of Parachute Opening Force

6.3.1 The force experienced by a parachute canopy during the inflation process can be found by Newton's Law

$$P = - \frac{W}{g} \frac{dv}{dt} \quad (8.45)$$

The value of  $dv/dt$  can be found from equation (8.39)

$$\frac{dv}{dt} = \frac{1}{t_f} \frac{dv}{dT} = - \frac{1}{t_f} \frac{2Tv + BT^2v^2}{A + T^2}$$

or

$$\frac{dv}{dt} = - \frac{Tv}{t_f} \left( \frac{2 + BTv}{A + T^2} \right) \quad (8.46)$$

where the value of  $v$  is given by equation (8.42).



Substituting the value of  $dv/dt$  from equation (8.46) into equation (8.45), the force experienced by the inflating canopy can be expressed as

$$P = \frac{WTV}{gt_f} \left[ \frac{2 + BTv}{A + T^2} \right] . \quad (8.47)$$

6.3.2 It is not possible to find the maximum opening force, the opening shock, directly from equation (8.47) above. Therefore, using the value of  $t_f$  found by the analytical method in Sec 6.2 above, the value of  $P$  given above is calculated for  $T$  ranging from 0 to 1 in intervals of 0.01. These calculations can be made on a calculation sheet such as the one shown in Fig 8-5. The values of  $P$  are then plotted versus  $T$ , and a smooth curve drawn through the points. From this curve, the value of the opening shock can be found as desired.

### 6.3.3 Comparison of Theoretical and Experimental Results

6.3.3.1 In order to check the accuracy of the analytical method for calculation of opening forces and filling times, results are compared with the experimental data presented in Ref 8. To cover the range of experimental data given in this reference, five launching velocities were chosen, namely,  $V_L = 100, 150, 200, 250$ , and  $300$  knots. Three different altitudes of  $7,000, 14,000$ , and  $20,000$  ft were chosen as in the reference. These launching velocities were converted to velocities at the beginning of inflation and presented in Fig 8-3, Progress Report No 15. Since it is more accurate to compare opening forces, calculations will be made based on the theory described above for a 28 ft circular flat parachute at the above values of launching velocity and altitude.

6.3.3.2 Preliminary calculations of opening forces have been made for an altitude of 20,000 ft, and Fig 8-6 compares experimental and theoretical values for that altitude. It is seen that the calculated values are lower than the experimental results, but are of the right magnitude. It is noted that the discrepancy does not vary with the launching velocity. These results are tentative and subject to revision. No judgment of the theory should be made until opening forces for altitudes of 7,000 and 14,000 ft are compared with experimental results.

#### 6.4 Size-Force history of Inflating Parachutes in a Wind Tunnel

6.4.1 During this reporting period, a series of tests were made to determine the proper magnitude of suspended mass which should be used to represent the finite mass case of parachute opening. The revised suspended mass system, shown in Fig 8-7, was described in detail in Progress Report No 15, Sec 7.3.3. The range of weights,  $W_s$ , of the suspended mass, including the weight cart, was from 2.00 to 5.25 lbs. These weights were used in conjunction with two circular flat parachutes with nominal diameters of 16 inches and 4 ft.

6.4.2 Figures 8-8 and 8-9 present typical force-time histories for the two parachutes using various values of suspended mass,  $W_s$ . During the test runs, high-speed movies were taken from such a position that the behavior of the suspension lines and canopy could be observed. Close examination of these films showed the parachutes to behave normally. The range of values of  $W_s$  did affect the opening time to a slight extent.

6.4.3 The important question is whether the finite or the infinite mass case of parachute opening is actually being represented. If the suspended mass is too great, the infinite mass case may be represented, and the value of  $W_s$  would have to be decreased in order to obtain the finite mass case as desired. Let us use  $F_{\max}$  to denote the maximum opening force (opening shock) between parachute and suspended mass, and  $F_c$  to denote the force obtained with constant velocity on the fully inflated parachute (steady state, infinite mass case), defined as

$$F_c = (C_D S)_{\max} q_f, \quad (8.48)$$

where  $(C_D S)_{\max}$  = maximum drag area of the canopy

$q_f$  = free stream dynamic pressure.

For the infinite mass case,  $F_{\max} > F_c$ . However, for the finite mass case, the opening shock is

$$F_{\max} = X (C_D S)_{\max} q_f = X F_c, \quad (8.49)$$

where the amplification factor,  $X < 1$ . Then  $F_{\max} < F_c$ .

6.4.4 At the dynamic pressure used in the tests of the 4 ft circular flat parachute, and using the appropriate  $(C_D S)_{\max}$ , the force  $F_c$  is approximately 65 to 75 lbs. Therefore, the finite mass case is represented for the range of values of  $W_s$  in question.

6.4.5 At the dynamic pressure used in the tests of the 16 inch circular flat parachute, and using the appropriate  $(C_D S)_{\max}$ , the force  $F_c$  is between 2 and 3 lbs. From Fig 8-9 we see that a suspended mass of 2.0 lbs represents a

borderline between the infinite and finite mass cases, where the opening shock is nearly equal to the "steady state" force,  $F_c$ .

6.4.6 Since the parachute travel distance in the test section of the wind tunnel is limited, it has been decided to use a 3 ft nominal diameter circular flat parachute together with a suitable value of  $W_g$  in future studies in order to insure that the parachute is completely open at the end of the run.

## 6.5 Proposed Work

6.5.1 Based on the analytical methods given in Sec 6.2 and 6.3 above, calculations will be made for opening time and opening forces of a 28 ft circular flat parachute at altitudes of 7,000, 14,000, and 20,000 ft and launching velocities of 100, 150, 200, 250, and 300 knots. These results will be compared with experimental results from Ref 8.

6.5.2 The deviation between experimental and theoretical results will be studied, and efforts will be made to further improve the theory so that results can be brought into closer agreement.

6.5.3 A series of size-force studies will be made in the subsonic wind tunnel using a 3 ft circular flat parachute with a suitable value of suspended mass to represent the finite mass case. High-speed movies of the opening canopy will be made while a simultaneous force-time history is being recorded.

6.5.4 The pressure distribution over the outer surface of models repre-

senting intermediate shapes of the inflating parachute canopy will be determined. As mentioned in Sec 6.1.4 above, these experiments have been made, and data is currently being reduced. This will be completed and the results presented in the next progress report.

6.5.5 A series of seven models of various shapes of the inflating parachute similar to the ones made for the external pressure distribution (described in Progress Report No 15, Sec 7.4.1) are being made. These models will be used to measure the pressure distribution over the internal surfaces of the inflating parachute canopy.

#### REFERENCES

- 1) United States Air Force Parachute Handbook, WADC Technical Report 55-265, 1956.
- 2) O'Hara, F.: Notes on the Opening Behavior and the Opening Forces of Parachutes, Royal Aeronautical Society Journal, November, 1949.
- 3) Von Karman, T.: Note on Analysis of the Opening Shock of Parachutes at Various Altitudes, 1945.
- 4) Milne-Thomson, L. M.: Theoretical Hydrodynamics, The Macmillan Co, New York, 1955.
- 5) Heinrich, H. G.: Experimental Parameters in Parachute Opening Theory, Aero Engineering Review, June, 1956.
- 6) Wilcox, B.: The Calculation of Filling Time and Transient Loads for a Parachute Canopy during Deployment and Opening, Research Report SC-4151 (TR), Sandia Corporation, February, 1958.
- 7) Foote, J. R. and Scherberg, M. G.: Dynamics of the Opening Parachute, WADC Report.
- 8) Freeman, H. F. and Rosenberg, C.: High Altitude and High Airspeed Tests of Standard Parachute Canopies, AFFTC TR 58-32.

①	T	0	0.1	0.2	0.3	0.4	0.5	0.6	0.7	0.8	0.9	1.0
②	T <sup>2</sup>	0	0.01	0.04	0.09	0.16	0.25	0.36	0.49	0.64	0.81	1.0
③	2T <sup>2</sup> /3	0	0.00212	0.00849	0.01910	0.03395	0.05305	0.07639	0.10398	0.13581	0.17189	0.21221
④	$2\sqrt{\frac{K}{K+1-T}}$	0.09400	0.06104	0.06934	0.07924	0.09110	0.10546	0.12302	0.14466	0.17174	0.20000	0.25000
⑤	$\frac{1}{2} - ④$	0.19600	0.18896	0.18066	0.17076	0.15890	0.14454	0.12698	0.10534	0.07826	0.04400	0
⑥	(2K+1-T) <sup>2</sup>	6.25000	5.76000	5.29000	4.84000	4.41000	4.00000	3.61000	3.24000	2.89000	2.56000	2.25000
⑦	4T <sup>2</sup> /π <sup>2</sup>	0	0.00405	0.01621	0.03648	0.06485	0.10132	0.14590	0.19859	0.25938	0.32828	0.40529
⑧	⑥ - ⑦	6.25000	5.75595	5.27379	4.80352	4.34515	3.89868	3.46410	3.04141	2.63062	2.23172	1.84471
⑨	√⑧	2.50000	2.39916	2.29649	2.19170	2.08451	1.97451	1.86121	1.74396	1.62192	1.49390	1.35420
⑩	T/π	0	0.03183	0.06366	0.09549	0.12732	0.15916	0.19099	0.22282	0.25465	0.28648	0.31831
⑪	⑤ × ⑨	0.49000	0.45335	0.41488	0.37425	0.33123	0.28540	0.23634	0.18371	0.12693	0.06573	0
⑫	⑩ + ⑪	0.49000	0.48918	0.47854	0.46974	0.45855	0.44456	0.42733	0.40653	0.38158	0.35221	0.31831
⑬	③ × ⑫	0	0.00103	0.00406	0.00897	0.01557	0.02358	0.03264	0.04227	0.05182	0.06054	0.0675
⑭	T <sup>4</sup>	0	0.00010	0.00160	0.00810	0.02560	0.06250	0.12960	0.24010	0.40960	0.65610	1.0
⑮	T <sup>4</sup> /4π <sup>2</sup>	0	0	0.00004	0.00021	0.00065	0.00158	0.00328	0.00608	0.01038	0.01662	0.02533
⑯	⑬ + ⑮	0	0.00103	0.00410	0.00918	0.01622	0.02516	0.03592	0.04835	0.06220	0.07716	0.09288

TABLE 8-2. NUMERICAL VALUES OF  $\frac{2T^2}{3\pi} \left\{ \frac{1}{4} - 2\left(\frac{\alpha}{2\alpha+1-T}\right)^2 \right\} \sqrt{(2\alpha+1-T)^2 - \frac{4T^2}{\pi^2} + \frac{T}{\pi}} + \frac{T^4}{4\pi^2}$   
FOR  $\alpha = 0.75$

①	T	0	0.1	0.2	0.3	0.4	0.5	0.6	0.7	0.8	0.9	1.0
②	T <sup>2</sup>	0	0.01	0.04	0.09	0.16	0.25	0.36	0.49	0.64	0.81	1.0
③	2T <sup>2</sup> /3π	0	0.00212	0.00849	0.01910	0.03395	0.05305	0.07639	0.10398	0.13581	0.17189	0.21221
④	$2\sqrt{\frac{K}{K+1-T}}$	0.07408	0.08200	0.09110	0.10162	0.11380	0.12700	0.14226	0.16438	0.18782	0.21596	0.25000
⑤	$\frac{1}{2} - ④$	0.17592	0.16800	0.15890	0.14838	0.13620	0.12200	0.10574	0.08562	0.06218	0.04404	0
⑥	(2K+1-T) <sup>2</sup>	9.00000	8.41000	7.84000	7.29000	6.76000	6.25000	5.76000	5.29000	4.84000	4.41000	4.00000
⑦	4T <sup>2</sup> /π <sup>2</sup>	0	0.00405	0.01621	0.03648	0.06485	0.10132	0.14590	0.19859	0.25938	0.32828	0.40529
⑧	⑥ - ⑦	9.00000	8.40595	7.82379	7.25352	6.69515	6.14868	5.61410	5.09141	4.58062	4.08172	3.59471
⑨	√⑧	3.00000	2.89930	2.79710	2.69324	2.58750	2.47966	2.36941	2.25642	2.14024	2.02035	1.89597
⑩	T/π	0	0.03183	0.06366	0.09549	0.12732	0.15916	0.19099	0.22282	0.25465	0.28648	0.31831
⑪	⑤ × ⑨	0.52776	0.48708	0.44446	0.39962	0.35242	0.30252	0.25054	0.19319	0.13308	0.06877	0
⑫	⑩ + ⑪	0.52776	0.51891	0.50812	0.49511	0.47974	0.46168	0.44153	0.41601	0.38773	0.35525	0.31831
⑬	③ × ⑫	0	0.00110	0.00431	0.00946	0.01629	0.02449	0.03373	0.04326	0.05266	0.06106	0.06755
⑭	T <sup>4</sup>	0	0.00010	0.00160	0.00810	0.02560	0.06250	0.12960	0.24010	0.40960	0.65610	1.0
⑮	T <sup>4</sup> /4π <sup>2</sup>	0	0	0.00004	0.00021	0.00065	0.00158	0.00328	0.00608	0.01038	0.01662	0.02533
⑯	⑬ + ⑮	0	0.00110	0.00435	0.00967	0.01694	0.02607	0.03701	0.04934	0.06304	0.07768	0.09288

TABLE 8-3. NUMERICAL VALUES OF  $\frac{2T^2}{3\pi} \left\{ \frac{1}{4} - 2\left(\frac{\alpha}{2\alpha+1-T}\right)^2 \right\} \sqrt{(2\alpha+1-T)^2 - \frac{4T^2}{\pi^2} + \frac{T}{\pi}} + \frac{T^4}{4\pi^2}$   
FOR  $\alpha = 1.0$

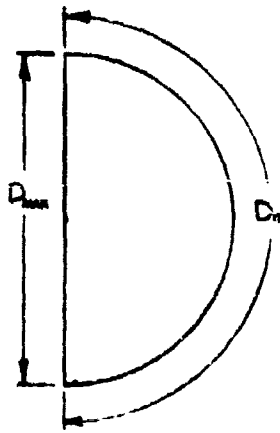


FIG 8-1. SHAPE OF FULLY INFLATED CANOPY

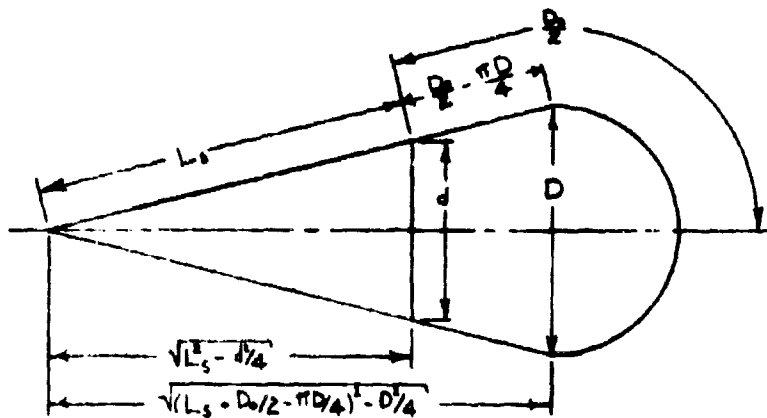


FIG 8-2. PARACHUTE SHAPE DURING INFLATION

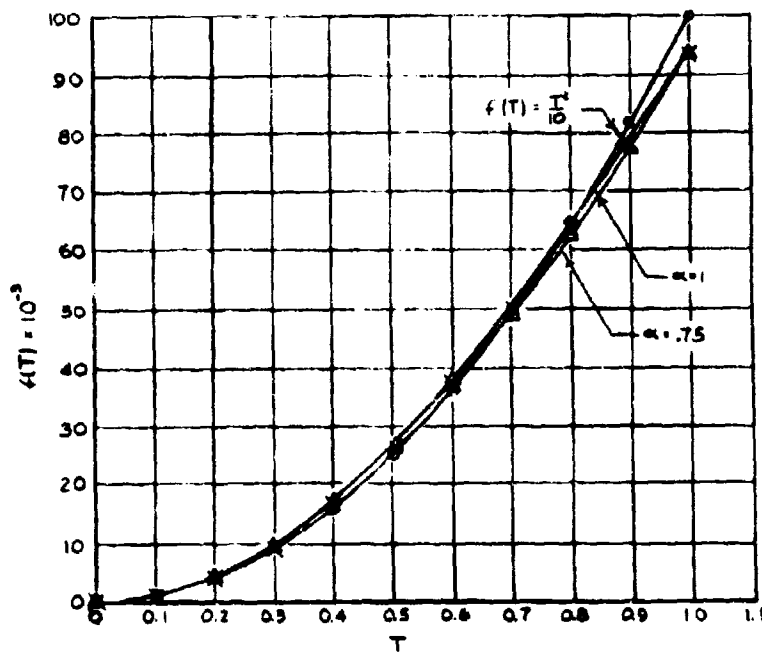


FIG 8-3. APPROXIMATION OF  $f(T)$  IN THE TOTAL MASS





$t_4 =$ 
 $\frac{\text{SEC}}{\text{FT}}$ 
 $C_0 =$ 
 $\frac{\text{FT}}{\text{SEC}}$

$D_0 =$ 
 $\frac{\text{FT}}{\text{SEC}}$ 
 $W =$ 
 $\frac{\text{LBS}}{\text{SEC}}$

$\sigma =$ 
 $\frac{\text{LBS}}{\text{SEC}}$ 
 $\rho =$ 
 $\frac{\text{LBS}}{\text{SEC}}$

$P =$ 
 $\frac{WTV}{g_4} \left[ \frac{2 + BTV}{A + T^2} \right]$

$V =$ 
 $\frac{BW}{Z} \left[ \frac{A + T^2 \tan^2 \frac{T}{A}}{A + T^2} - T \right] + \frac{A + T^2}{A}$

$A =$ 
 $\frac{10W}{990^2}$

$B =$ 
 $\frac{5(C_0^2 t_4)}{D_0^2}$

$\frac{BW}{Z} =$ 
 $\frac{W}{g_4}$

1	T	0.0	0.1	0.2	0.3	0.4	0.5	0.6	0.7	0.8	0.9	1.0
2	T <sup>2</sup>	0.0	0.01	0.04	0.09	0.16	0.25	0.36	0.49	0.64	0.81	1.0
3	A + T <sup>2</sup>											
4	③ ÷ A											
5	③ ÷ A <sup>2</sup>											
6	T/A											
7	TAN <sup>-1</sup> T/A (DEG)											
8	TAN <sup>-1</sup> T/A (RAD)											
9	⑤ x ④											
10	⑥ - T											
11	DW/2 x ⑩											
12	⑪ ÷ ④											
13	V ÷ ④ = V											
14	TV											
15	BTV											
16	BTV ÷ 2											
17	⑬ ÷ ⑬											
18	⑬ x ⑬											
19	W/g <sub>4</sub> x ⑬ = P											

FIG 8-5. CALCULATION SHEET FOR FINDING THE MAX. OPENING FORCE FOR A FLAT CIRCULAR PARACHUTE

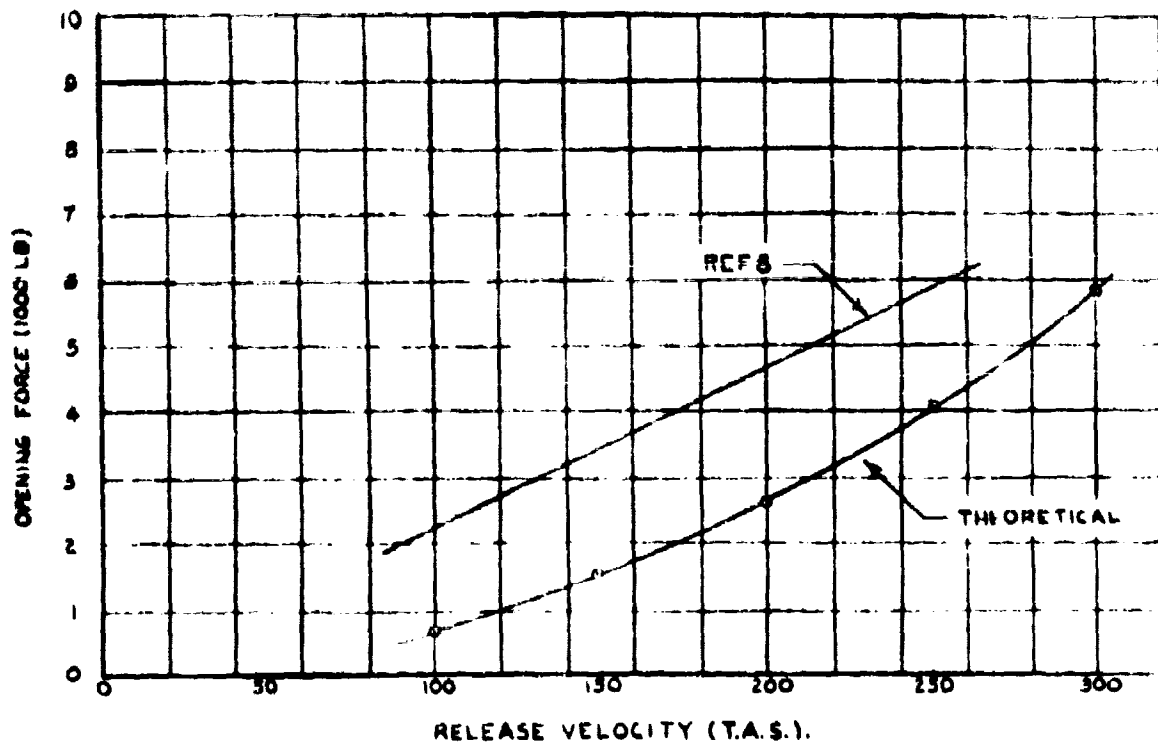


FIG 8-6. COMPARISON OF EXPERIMENTAL AND THEORETICAL VALUES OF OPENING FORCE FOR A 28 FT FLAT CIRCULAR PARACHUTE DEPLOYED AT 20,000 FEET ALTITUDE

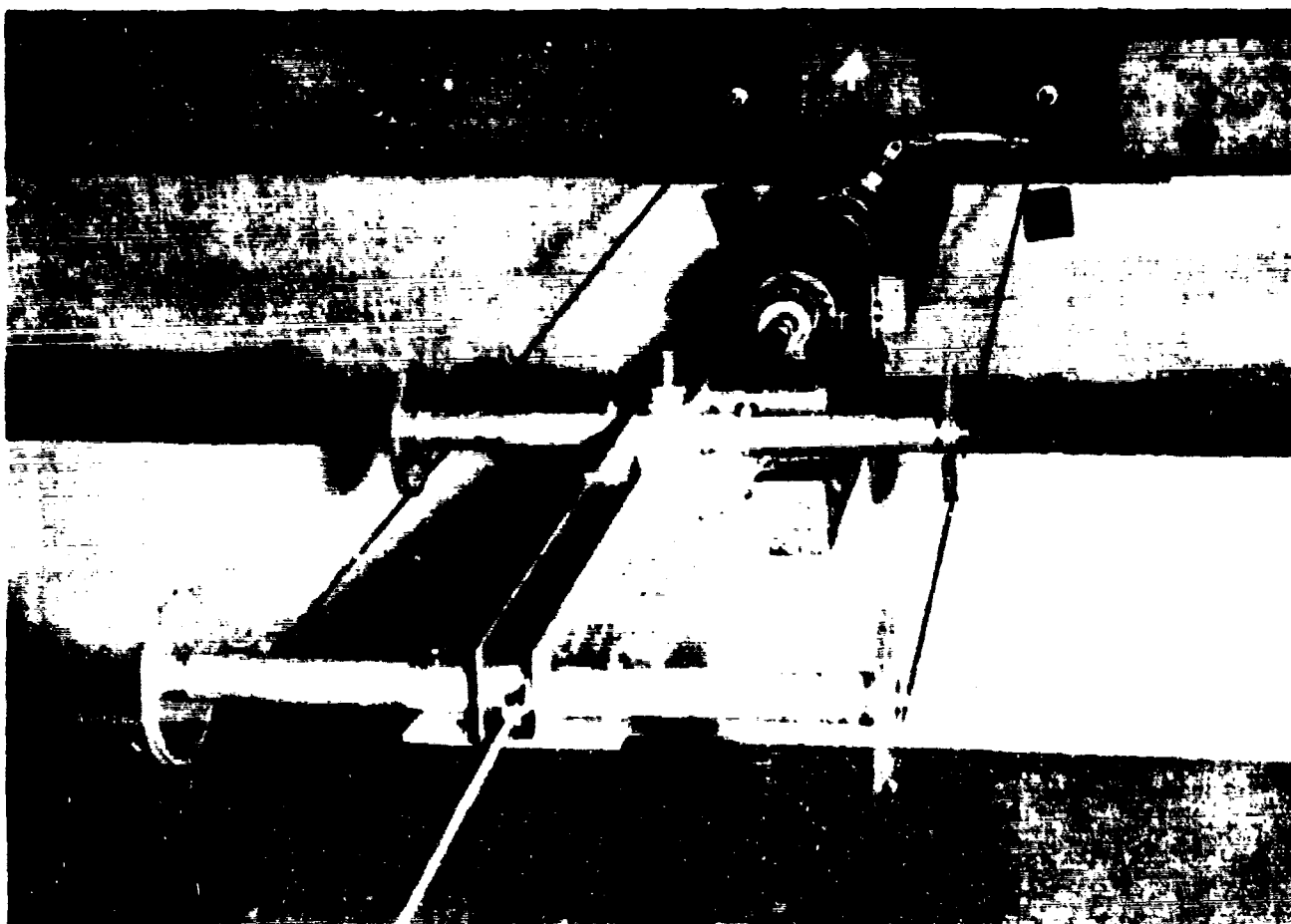


FIG 8-7. SUSPENDED MASS SYSTEM FOR OPENING PARACHUTE STUDY

110605978

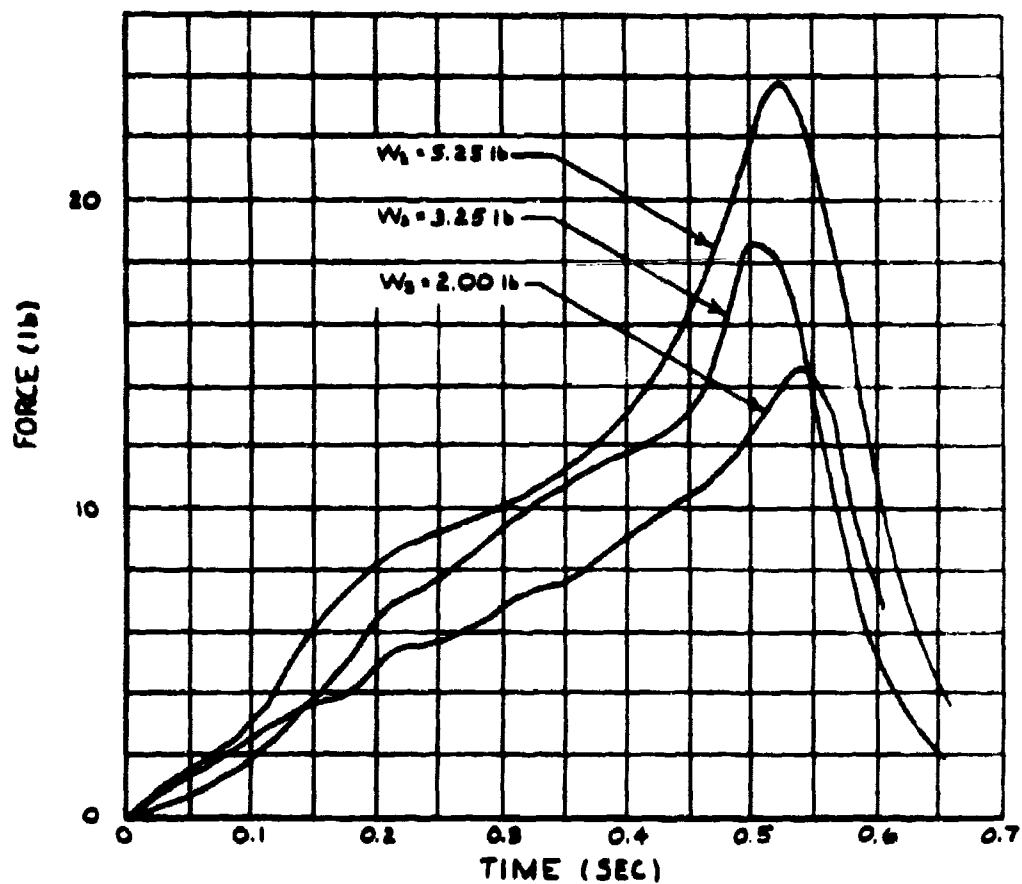


FIG 8-8. TYPICAL FORCE-TIME HISTORIES FOR 4 FT CIRCULAR FLAT PARACHUTE WITH VARIOUS VALUES OF SUSPENDED MASS

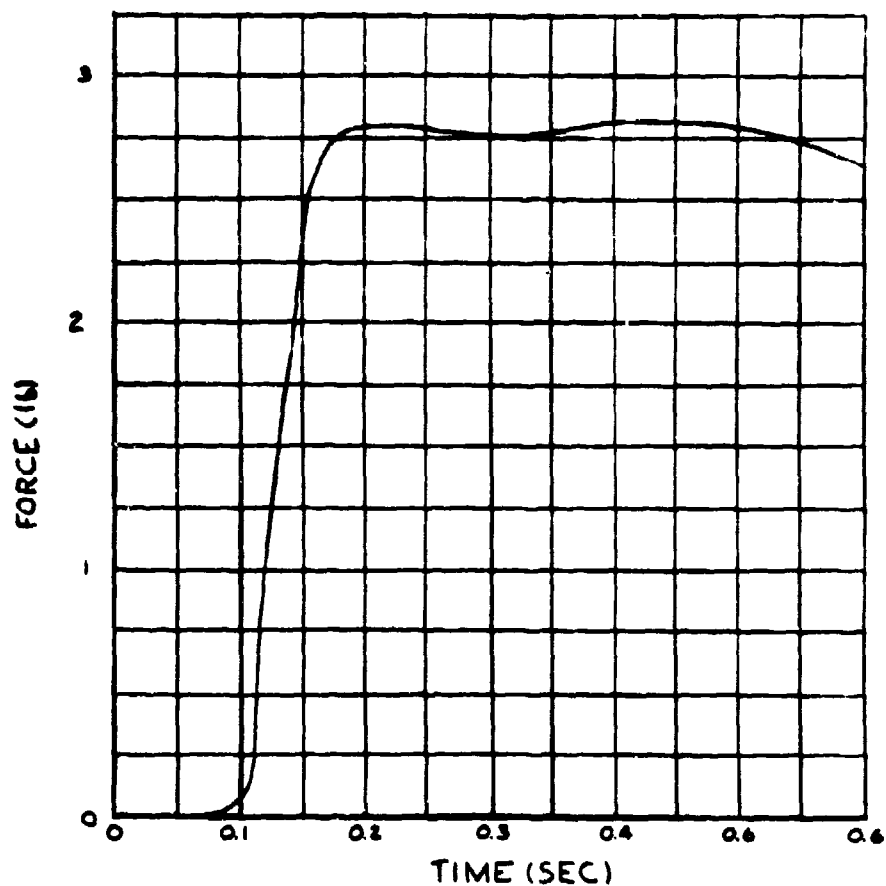


FIG 8-9. FORCE-TIME HISTORY FOR 16 INCH SOLID FLAT PARACHUTE WITH  $W_s = 2.0 \text{ LB}$

## Project No 9

### 7.0      Statistical Analysis of Extraction Time, Deployment Time, Opening Time, and Drag Coefficient for Aerial Delivery Parachutes and Systems

7.1      The draft of the final technical report of this project has been completed, and is currently being reviewed.

## Project No 10

### 8.0 Study of Basic Principles of New Parachutes and Retardation Devices

#### 8.1 Introduction

8.1.1 The objective of this study is to determine the effect of the presence of a blunt primary body ahead of the vortex ring parachute on its drag characteristics and rotational velocity.

8.1.2 The geometrical characteristics of the vortex ring parachute, a description of the apparatus used to measure drag of the model, and the drag and rotational characteristics of the model alone as a function of free stream velocity were presented in Progress Report No 12. The drag coefficient,  $C_D$ , as a function of free stream velocity and Reynolds number over an extended range was presented in Figs 10-2 and 10-3 of Progress Report No 13.

8.1.3 The blunt body in these tests is a simulated A-22 Cargo Container with prototype dimensions 60 x 52 x 43 inches. A 32 ft nominal diameter vortex ring cargo parachute was taken as a reference prototype parachute. Because the vortex ring parachute model has a nominal diameter of 1.48 ft, the simulated container has the dimensions 2.78 x 2.41 x 2.00 inches, with a frontal area of 4.82 square inches. The distance from the confluence point of the parachute model suspension lines to the simulated container is equivalent to a 10 ft riser on the prototype.

#### 8.2 Experiments

8.2.1 To measure the drag of the parachute with blunt body, the simulated A-22 container was mounted in the test section as shown in Fig 10-1, with the drag line for the parachute running freely through the center of the container to the strain gage drag pickup described in Progress Report No 12, Sec 9.2.2 and Figs 10-1 and 10-4.

8.2.2 The drag and rotational characteristics of the model were measured at free stream velocities between 70 and 221 ft/sec, corresponding to a range of dynamic pressures from 1 to 10 inches of water, at intervals of 1 inch water. The tests were conducted as follows:

- 1) The dynamic pressure settings were accurately controlled using a micromanometer reading to 0.001 inch water head.
- 2) Drag measurements were recorded over a period of 5 sec at each increment of dynamic pressure through the use of a Century Recording Oscillograph, thereby allowing an average value to be determined.
- 3) At each increment of dynamic pressure, the rotation of the model was recorded using a high speed movie camera and the method described in Progress Report No 15, Sec 9.3.4.
- 4) When a dynamic pressure of 10 inches of water was reached, the cycle was repeated. A total of three cycles completed the test.

### 8.3 Results

8.3.1 It is found that the drag coefficient for the parachute with the blunt body in front varies from  $C_D = 1.15$  at 50 ft/sec to 1.32 at 220 ft/sec,

as shown in Fig 10-2. This is compared with the results for the parachute alone (Progress Report No 13), where  $C_D = 1.25$  at 50 ft/sec and  $C_D = 1.46$  at 220 ft/sec. Therefore, it is seen that the blunt body decreases the drag coefficient by approximately 8 to 10%, as shown in Fig 10-3.

8.3.2 As shown in Fig 10-4, the rotational velocity varies linearly from 19 rev/sec at 70 ft/sec to 58 rev/sec at 220 ft/sec. The gore tip velocity is also shown in this figure; both rotational and tip velocities are compared with the results for the parachute alone, where the rotational velocity varied linearly from 20 rev/sec at 70 ft/sec to 62 rev/sec at 220 ft/sec.

8.3.3 As a check of the testing method and apparatus a Ribbon parachute model with 20% geometrical porosity and 50-in prototype diameter was tested both in free stream and with the simulated A-22 cargo container using a 10 ft riser. As shown in Fig 10-2, the free stream drag coefficient was  $C_D = 0.58$ . This compares well with previous experimental results. When tested with the blunt body, the drag coefficient varied from  $C_D = 0.55$  at 120 ft/sec to  $C_D = 0.432$  at 170 ft/sec (Fig 10-2), which represents a decrease of the drag coefficient varying from 5 to 25% as shown in Fig 10-3. The Ribbon parachute model displayed some squidding action at the higher velocities, which explains the drop in drag coefficient.

#### 8.4 Proposed Work

8.4.1 An attempt will be made to improve the drag characteristics of the vortex ring parachute through the use of a model of this parachute which has adjustable lines, tuned to optimum efficiency, rather than the model with fixed lines which has been previously tested.



8.4.2 This vortex ring parachute model tuned to optimum efficiency will also be tested in search of a standing vortex ring (See Progress Report No 15, Sec 9.3).

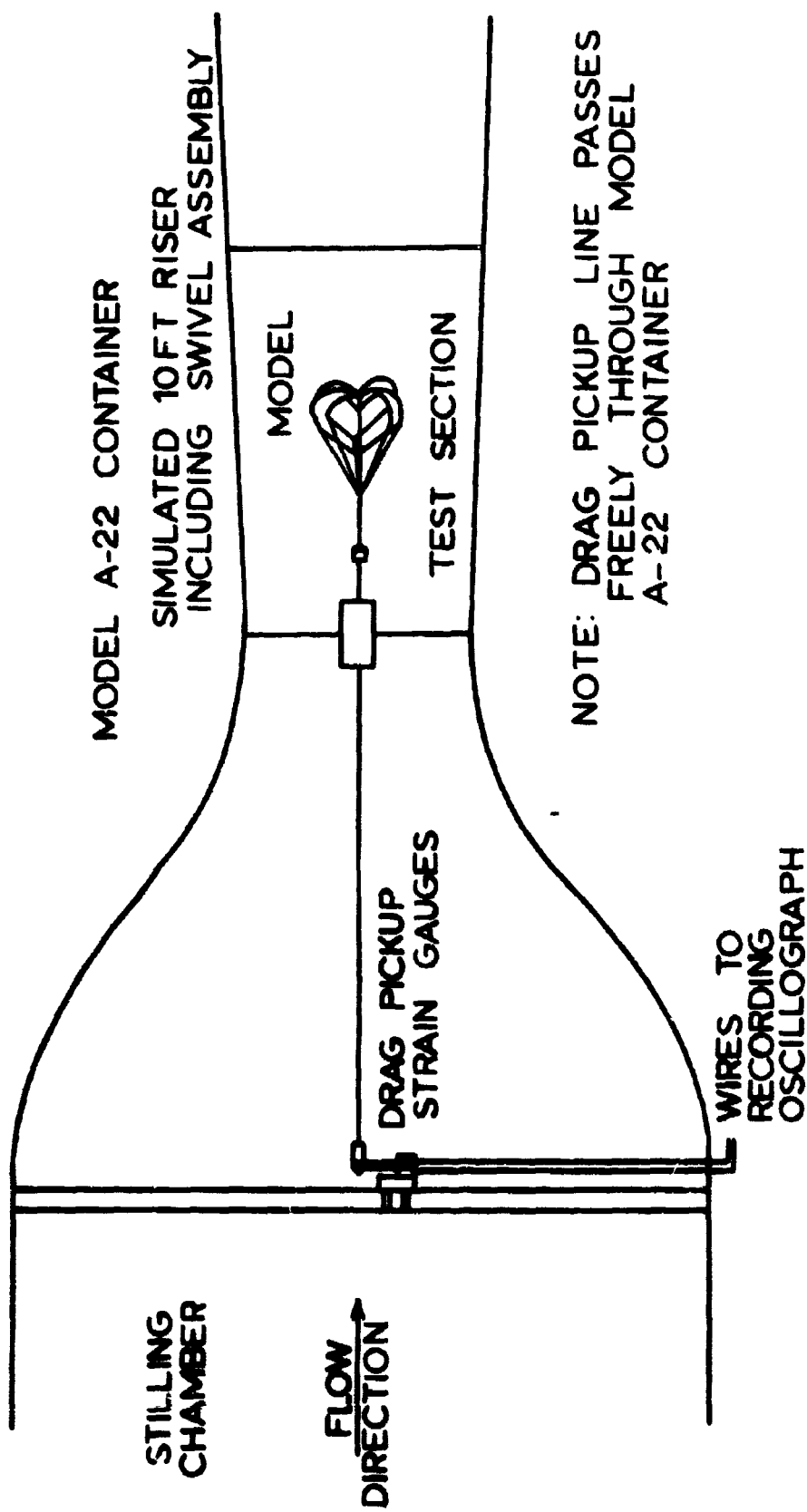


FIG 10-1. SCHEMATIC OF TEST SETUP TO MEASURE DRAG OF THE VORTEX RING PARACHUTE MODEL

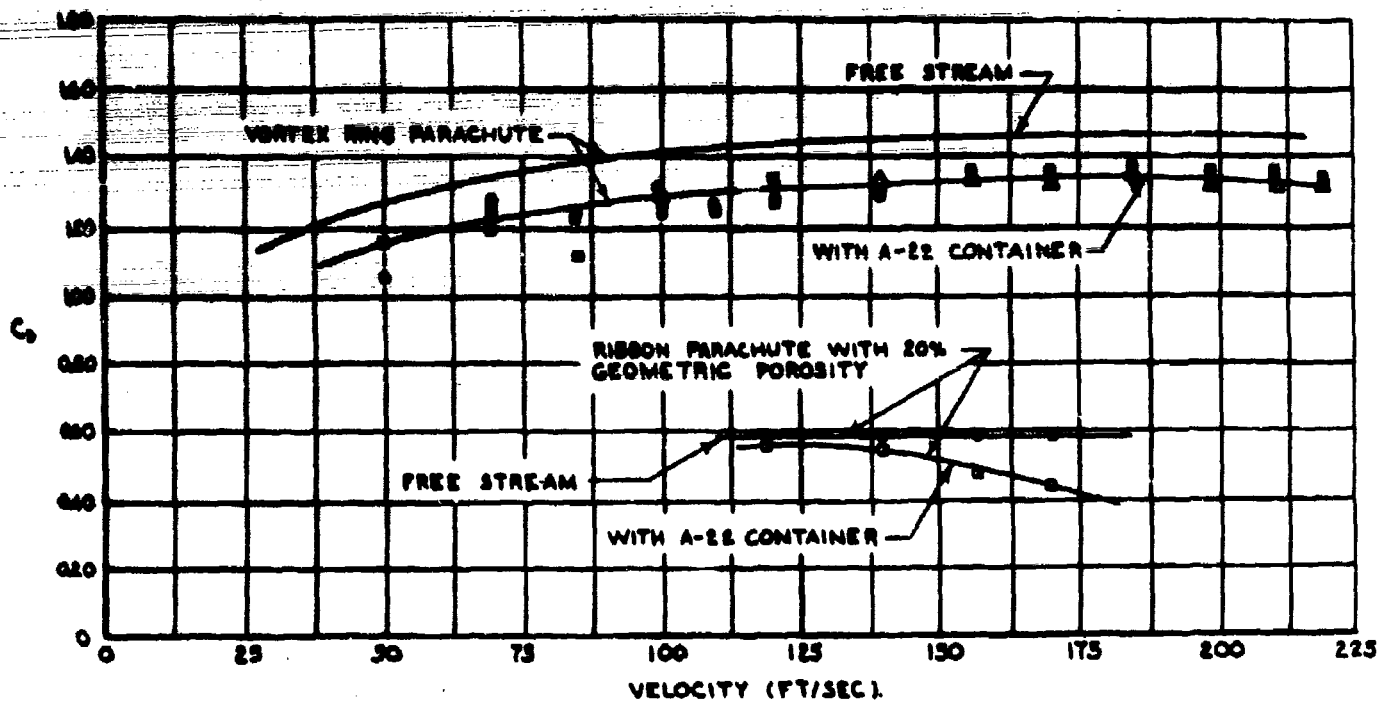


FIG 10-2. DRAG COEFFICIENT VERSUS VELOCITY FOR VORTEX RING PARACHUTE ALONE AND WITH A-22 CONTAINER ON 10 FOOT RISER

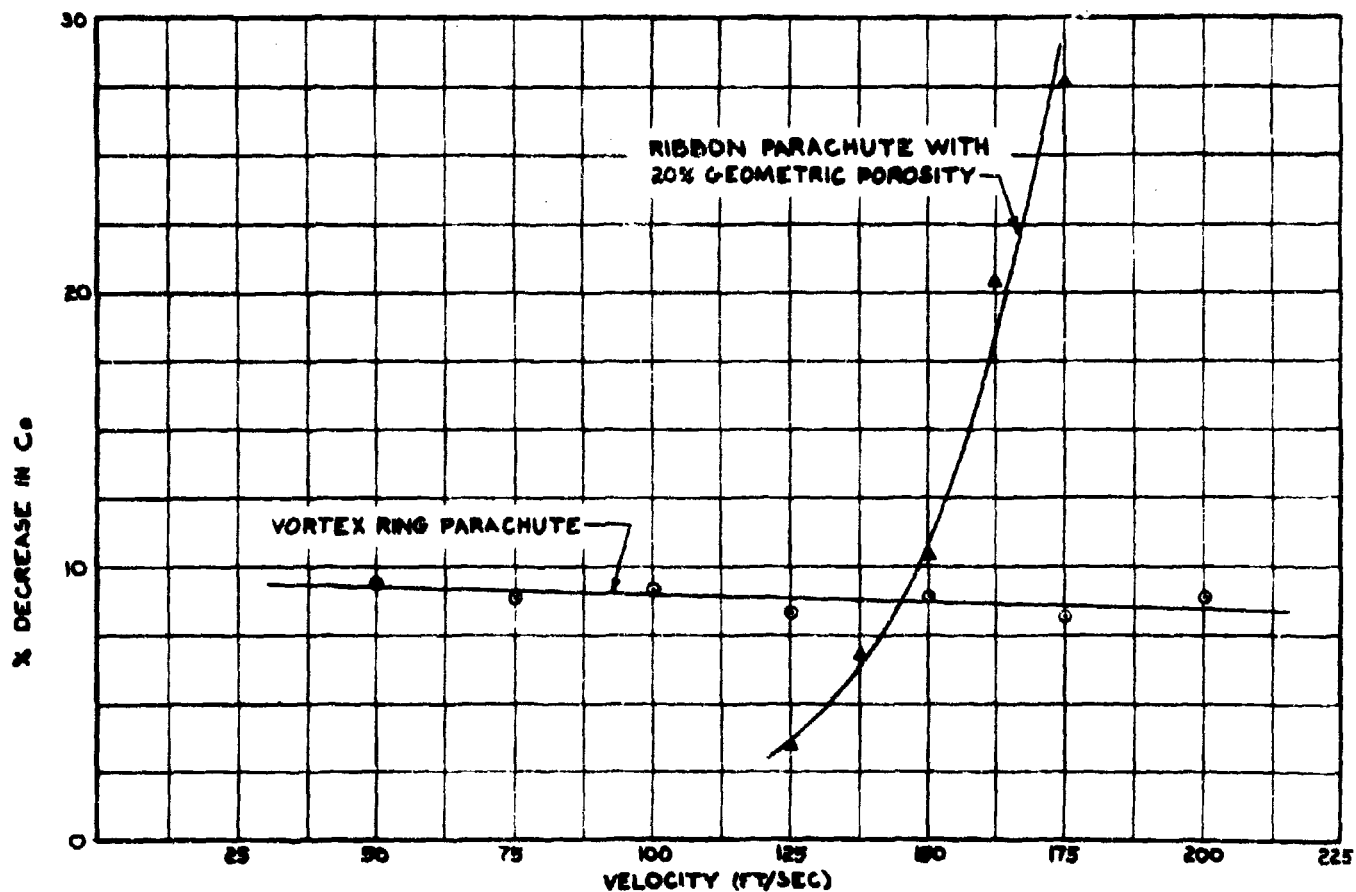


FIG 10-3. PERCENT DECREASE IN DRAG COEFFICIENT DUE TO A-22 CONTAINER FOR VORTEX RING AND RIBBON PARACHUTES

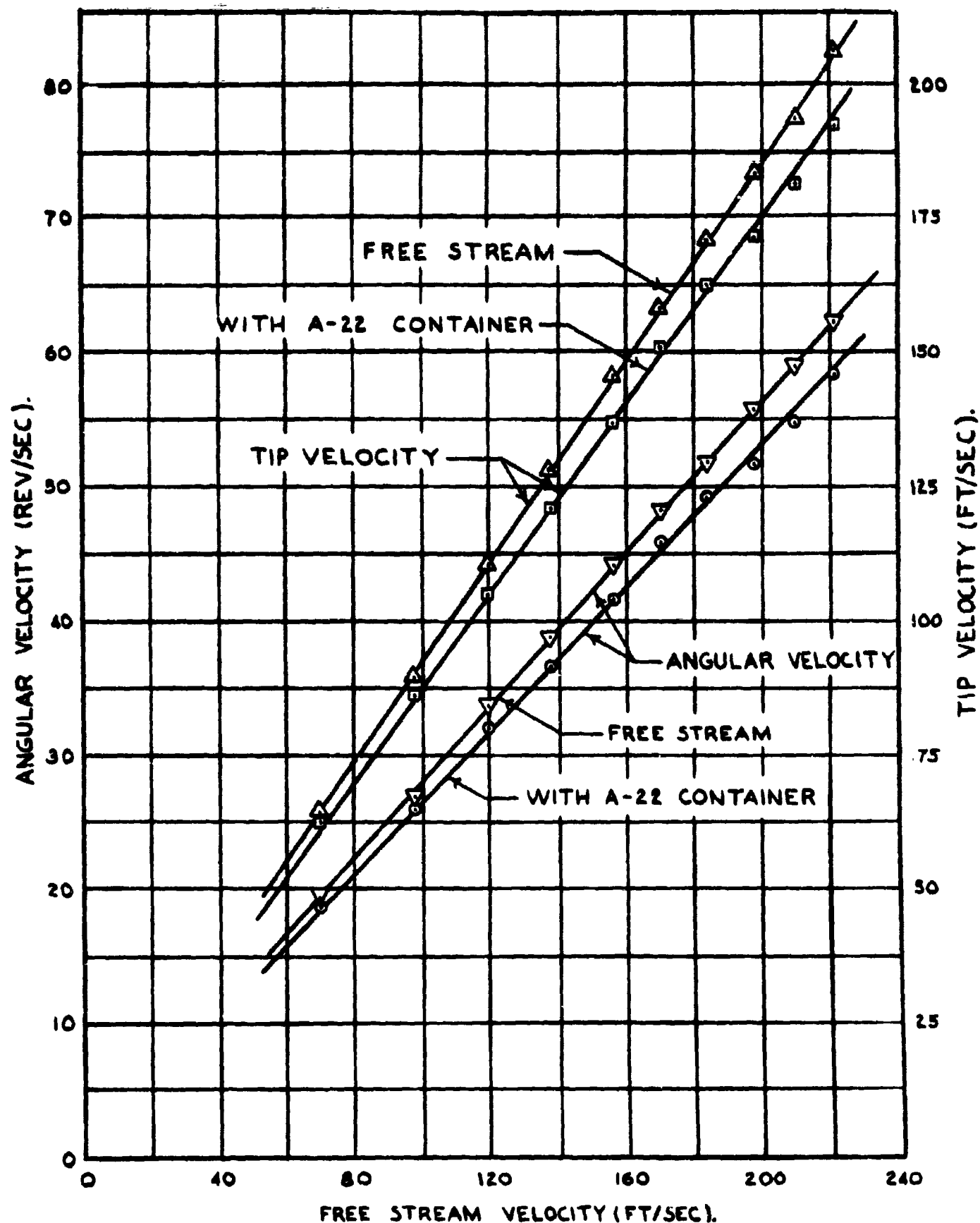


FIG 10-4. ANGULAR VELOCITY AND TIP VELOCITY VS. FREE STREAM VELOCITY FOR THE VORTEX RING PARACHUTE MODEL ALONE AND WITH A-22 CARGO CONTAINER ON A 10 FT RISER

## APPENDIX

The authors of this report who are listed on the front page wish to acknowledge the assistance of the following personnel:

### Clerical Staff:

E. Zembergs, Sr. Engineering Assistant  
Beverly M. Froers, Secretary

### Graduate Students:

I. C. Bhateley, Research Assistant  
E. M. Linhart, Research Assistant  
D. J. Monson, Research Assistant  
I. W. Russell, Research Assistant  
R. E. Schaller, Research Assistant

### Undergraduate Students:

R. E. Albrecht, Engineering Assistant  
J. S. Iratly, Engineering Assistant  
L. L. Cluever, Engineering Assistant  
C. V. Eckstrom, Engineering Assistant  
D. J. Eckstrom, Engineering Assistant  
D. D. Evenson, Engineering Assistant  
R. W. Friestad, Engineering Assistant  
S. R. Hess, Engineering Assistant  
L. R. Jamison, Engineering Assistant  
D. A. MacLean, Engineering Assistant  
D. E. McGee, Engineering Assistant  
W. R. Mueller, Engineering Assistant  
D. L. Pekarek, Engineering Assistant  
M. Putnins, Engineering Assistant  
A. Perlbachs, Engineering Assistant  
R. O. Strom, Engineering Assistant

### Machine Shop Personnel:

J. Taube, Laboratory Machinist  
P. A. Huehnert, Wind Tunnel Mechanic.